UNIVERSITY OF OKLAHOMA

GRADUATE COLLEGE

SEISMIC STRATIGRAPHY OF A PROBLEMATIC CIRCULAR CONCAVE-DOWNWARD STRUCTURE, CHUKCHI SEA

A THESIS

SUBMITTED TO THE GRADUATE FACULTY

in partial fulfillment of the requirements for the

Degree of

MASTER OF SCIENCE

By

ANDRES HERNAN RUIZ LOZANO
Norman, Oklahoma
2017

SEISMIC STRATIGRAPHY OF A PROBLEMATIC CIRCULAR CONCAVE-DOWNWARD STRUCTURE, CHUKCHI SEA

A THESIS APPROVED FOR THE
CONOCOPHILLIPS SCHOOL OF GEOLOGY AND GEOPHYSICS

BY

Dr. John Pigott, Chair

Dr. Kurt Marfurt

Dr. Shankar Mitra

This thesis is dedicated to my Mother, my Father, my Sister, and my Brother, without them this could not have been possible.

Acknowledgements

I would like to thank my advisor Dr. John D. Pigott for his guidance and advice that made possible this thesis, to Louis Niglio from the Bureau of Ocean Energy Management for providing the data and his help on this project. To the members of my committee Dr. Kurt J. Marfurt and Dr. Shankar Mitra for their reviews and help with this work. To Javier Tellez, Emilio Torres, Antonio Cervantes, Rafael Pires, and other graduate students for their help and advice. In addition, special thanks to Schlumberger for providing the Petrel license.

I would also like to thank my Mother for always believing in me and for being always there, my father for his support and advice, my sister for always encouraging me to follow my goals, and my brother for his support.

Table of Contents

List of Tables

List of Figures

Abstract

A circular concave-downward structure (CCDS) and its structural features and seismic facies can be observed in several 2D seismic lines imaging the Chukchi Sea planning area. The area in question is largely underexplored and the data coverage is limited. Nonetheless, it is possible to make a proper assessment of this geological problem, or at least an educated guess through the application of seismic interpretation techniques that combine both geophysical and geological principles such as seismic stratigraphy and fault mechanical stratigraphy to propose a solution to the geological process responsible.

Derived from the principles of Steno's law of superposition and cross cutting relations, and the deterministic and empirical description of rock strength dependence with depth and age, fault mechanical stratigraphy is useful to analyze faulting chronographically. When combined with seismic stratigraphy, an approximate geological age can be given to the faults. In the study of this structure, the analysis of the ages of the faults associated with the structure is crucial.

From the observations derived from the seismic stratigraphic method of interpretation and the fault mechanical stratigraphy analysis, three geological hypotheses were proposed to explain this structure: reactive diapirism, wrench fault-associated gas chimney, and a complex meteorite impact crater.

The fault mechanical stratigraphy of the faults related to the structure constrains the timing of the faults related to the structure and of the structure itself to a very limited time range in the middle Eocene. Together with a concentric-ring geometry of the faults,

a central uplift feature at the base of the structure, and chaotic reflectors above and around this central uplift strongly suggests it is a complex meteorite impact structure.

Complex meteorite impact crater morphology can be resolved within seismic resolution; their diameter is larger than 4 km. Three main distinctive features of these relatively large structures can be interpreted in seismic data: collapse faults rimming the crater produced by gravitational failure towards the center of the crater, a central uplift at the center of the crater generated by the rebound of the energy of the impact, and impact breccia infill.

1. Introduction

1.1. Problem definition

The Chukchi Sea Planning area (Figure 1.1.2) is located offshore of the National Petroleum Reserve in Alaska (NPRA). A series of 2D seismic surveys were acquired in the area and processed during the late 80s early 90s for future leasing. In these 2D seismic lines, structures such as shale and evaporite diapirs (Thurston and Theiss, 1987; Thurston and Lothamer, 1991), folding (Thurston and Theiss, 1987), and wrench faulting (Thurston and Theiss, 1987) have been interpreted and described. Nonetheless these structural styles cannot consistently explain the structural features of a problematic circular-concave downward structure observed in an area of the Central Chukchi Basin (Figures 1.1.3, 1.1.4 and 1.1.5). This structure is characterized by a marked contrast between parallel seismic facies and chaotic facies from the structure; the structural style of the structure also differ from the more regional style.

Therefore, the purpose of this work is to propose a geological scenario that is consistent with the structural styles and reflector facies of the CCDS.

The approach to investigate the problem will be to utilize the seismic stratigraphic approach developed by Vail et al. (1977) and expanded upon by Pigott and Radivojevic (2010), as well as the fault mechanical stratigraphic method described by Pigott and Abouelresh (2016).

Figure 1.1.1 Location of the Chukchi Sea Planning area outlined in red; source: Data SIO, NOAA, U.S. Navy, NGA, GEBCO, Image Landsat/Copernicus, US Dept of State Geographer, 12/13/2015, © 2017 Google.

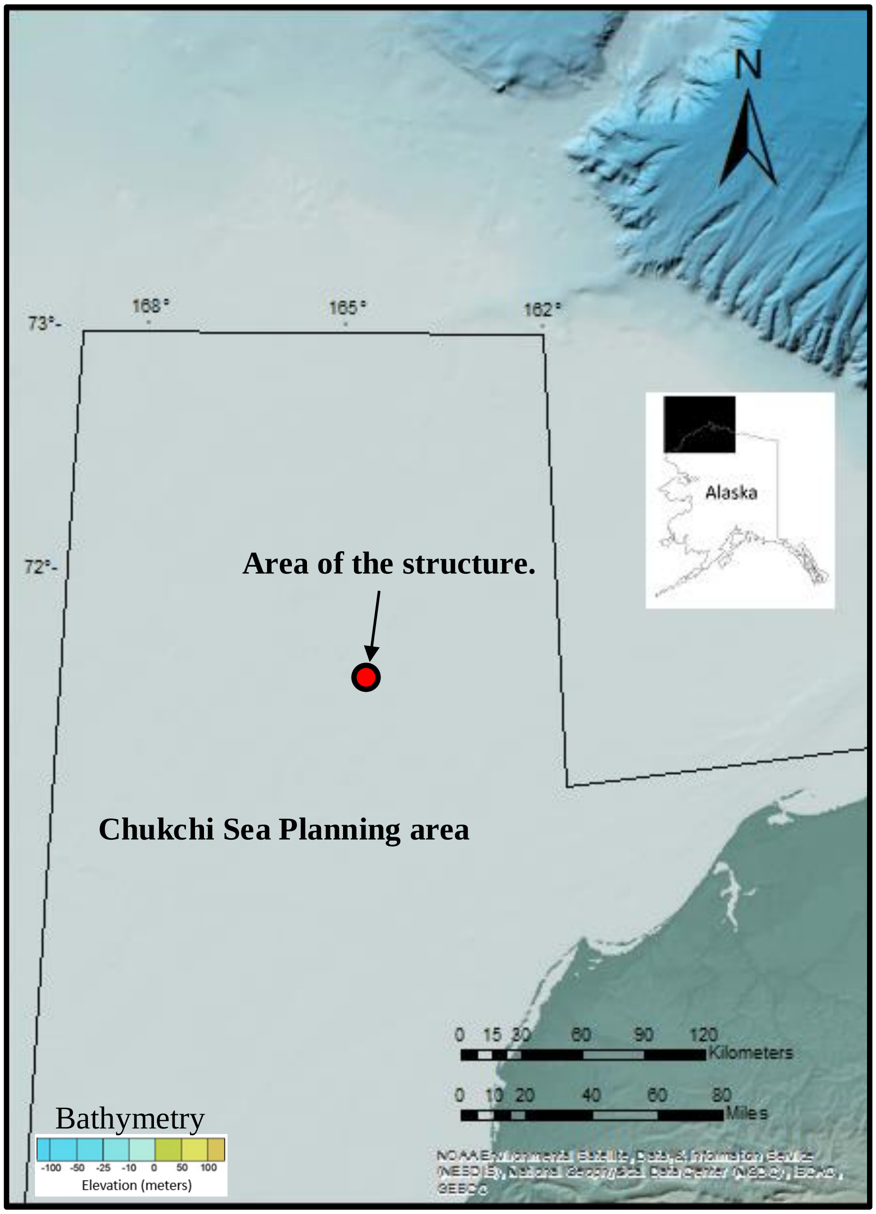

Figure 1.1.2 Chukchi Sea Planning Area, after Thurston and Theiss (1987). Topographic and bathymetric basemap from Jakobsson et al. (2012), area of the structure indicated by the red circle.

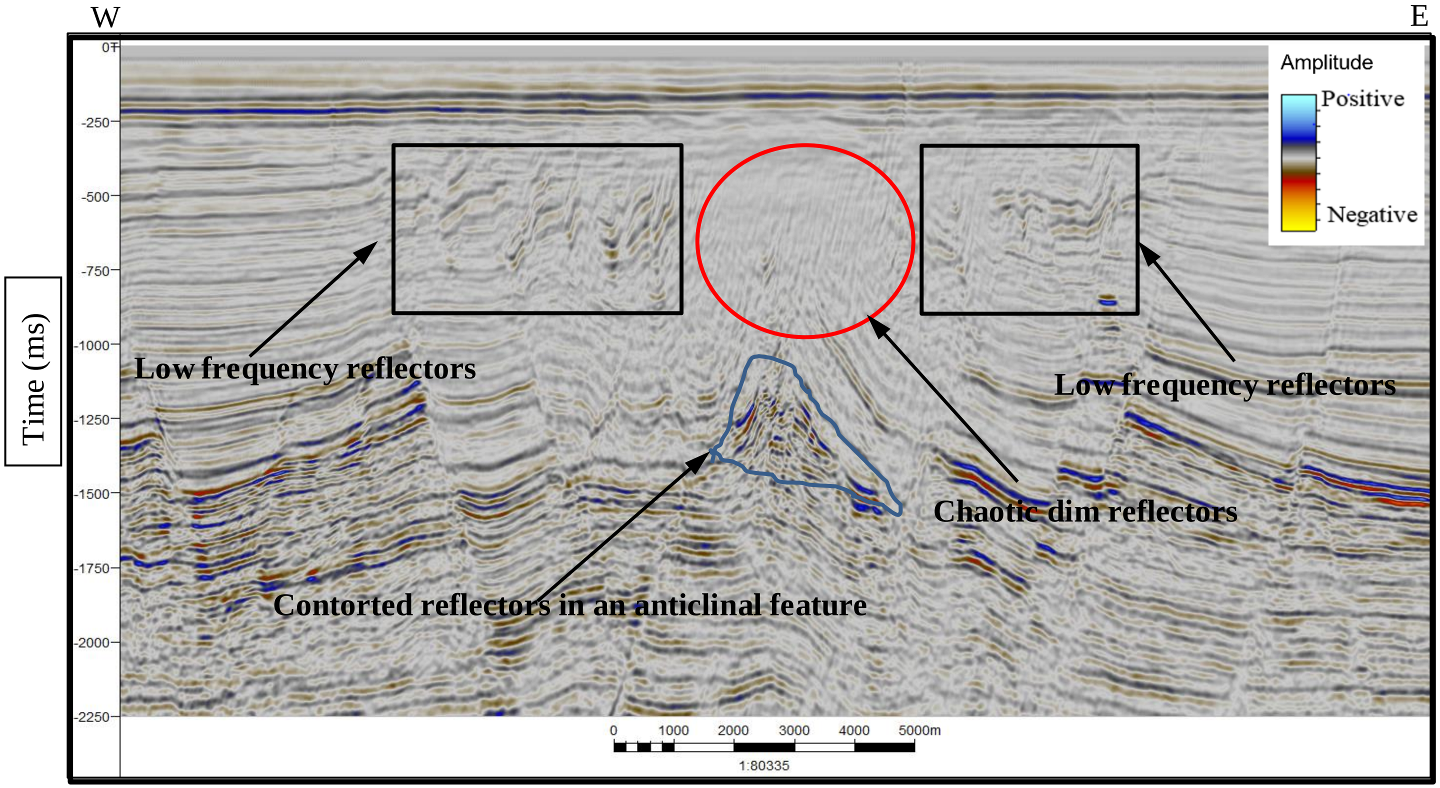

Figure 1.1.3 Characteristic elements of the CCDS on line wcs-6059. Location shown in Figure 1.1.6.

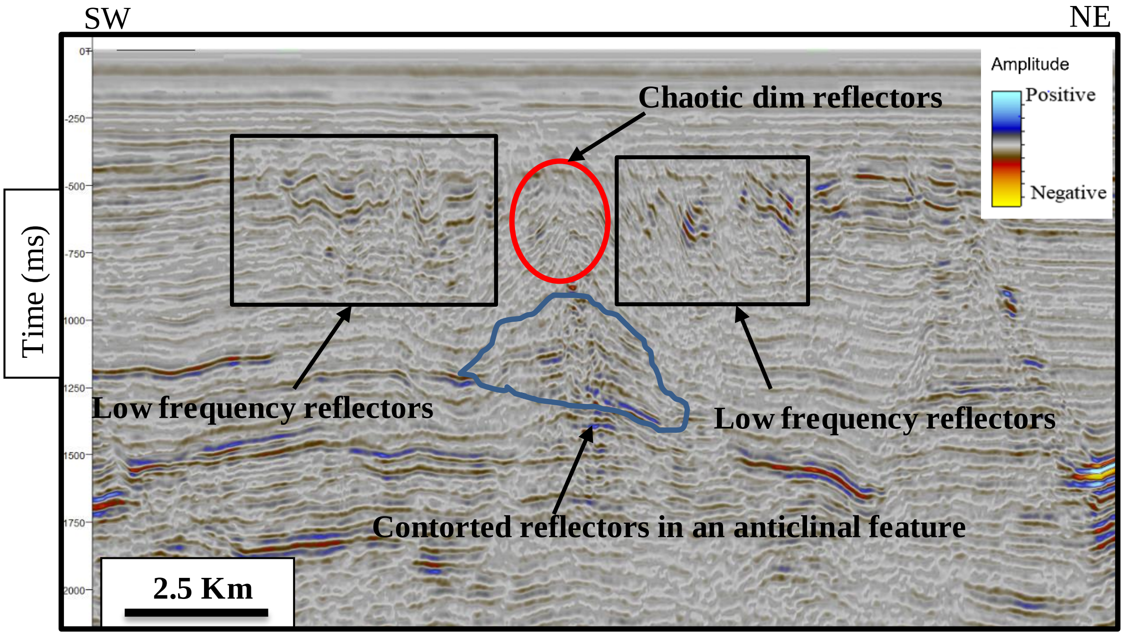

Figure 1.1.4 Characteristic elements of the CCDS on line ch83-104a. Location shown in Figure 1.1.6.

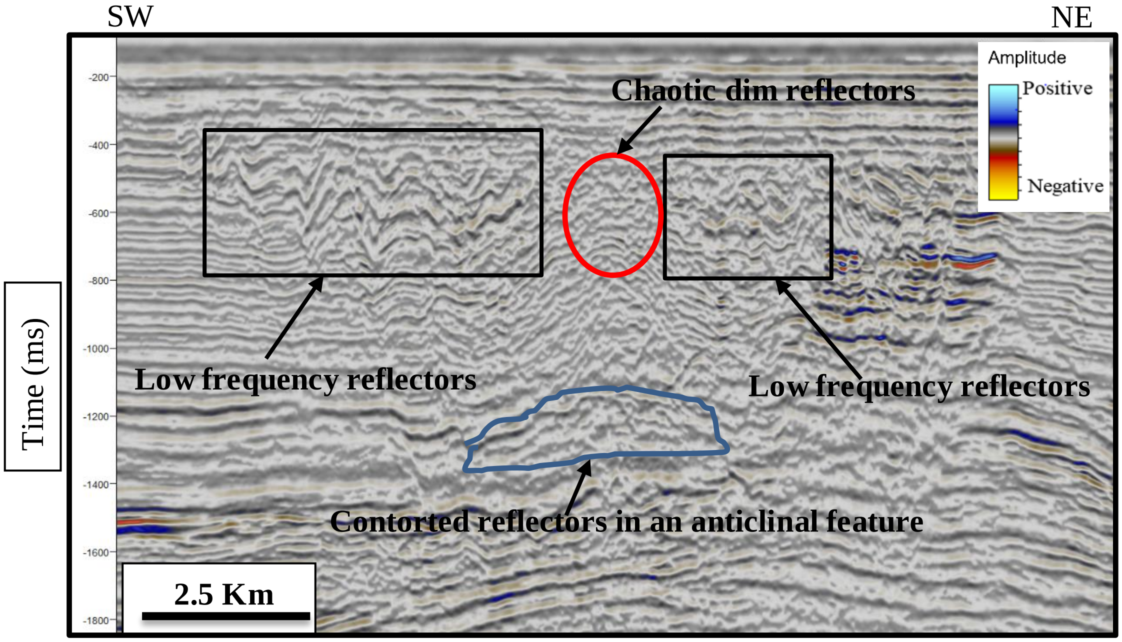

Figure 1.1.5 Characteristic elements of the CCDS on line sc86_8459. Location shown in Figure 1.1.6.

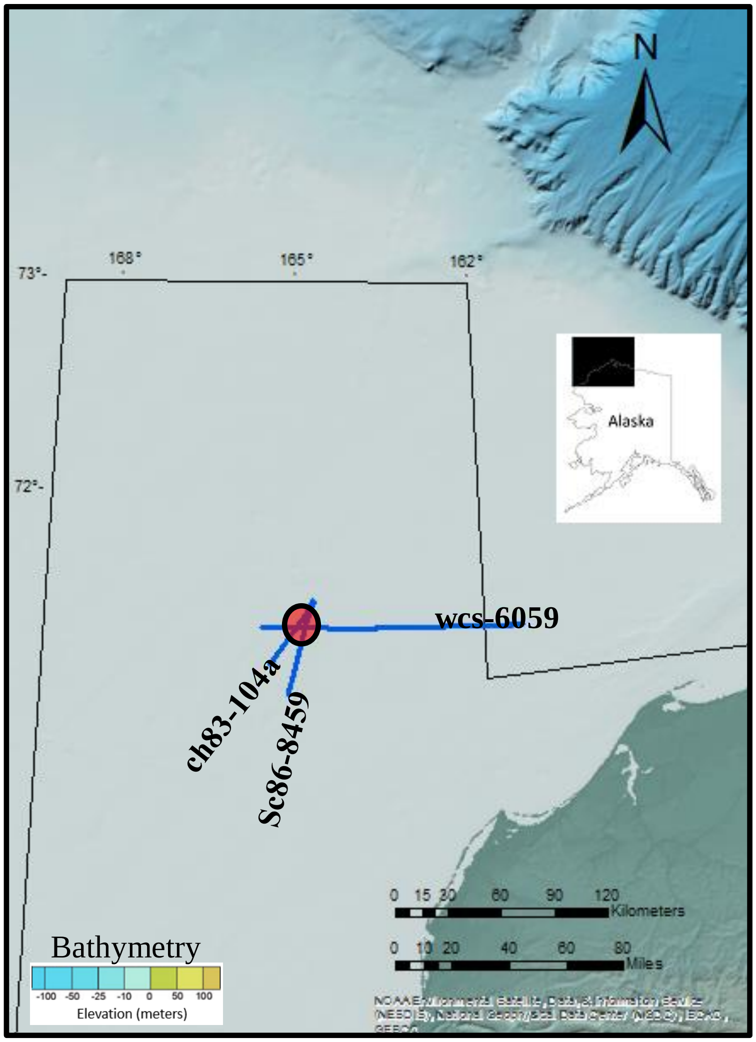

Figure 1.1.6 Position of the lines where the CCDS is identified. The area of the structure is indicated by the red circle. Topographic and bathymetric basemap from Jakobsson et al, 2012

1.2.Data availability

The following data were interpreted in this study.

1. 110 DMO/post-stack migrated 2D seismic lines, with a total length of ~11707 km (~7274 miles) (Figure1.3).

2. Well tops, total gamma ray log, and checkshots from the Crackerjack #1 OCS-Y-1320 well.

The lines interpreted in this study were acquired and processed in several surveys by different companies, resulting in variable data quality. The acquisition and processing parameters are unknown nonetheless the overall quality of the seismic data in the zone of interest is good. Line wcs-6057 illustrates an example of good quality in the data (Figure 1.5), and line gp85-229-2 provides an example of data contaminated by out of the plane noise which is probably a product of migration artifacts.

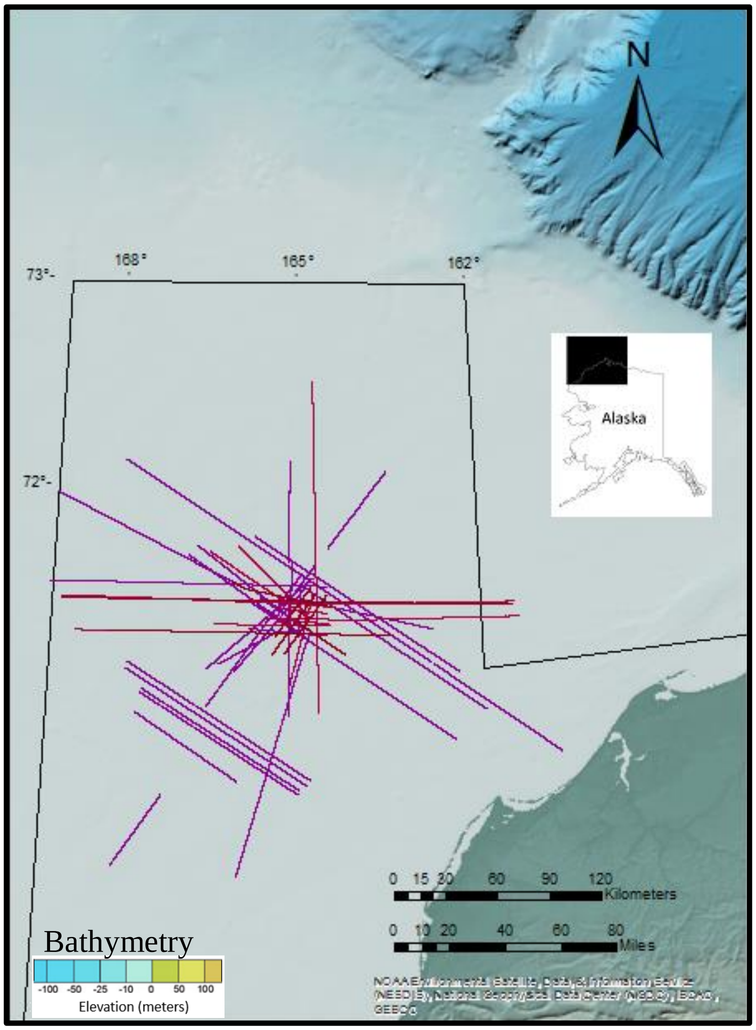

Figure 1.2.1 Position of the 110 seismic lines used in this study, Topographic and bathymetric basemap from Jakobsson et al. (2012).

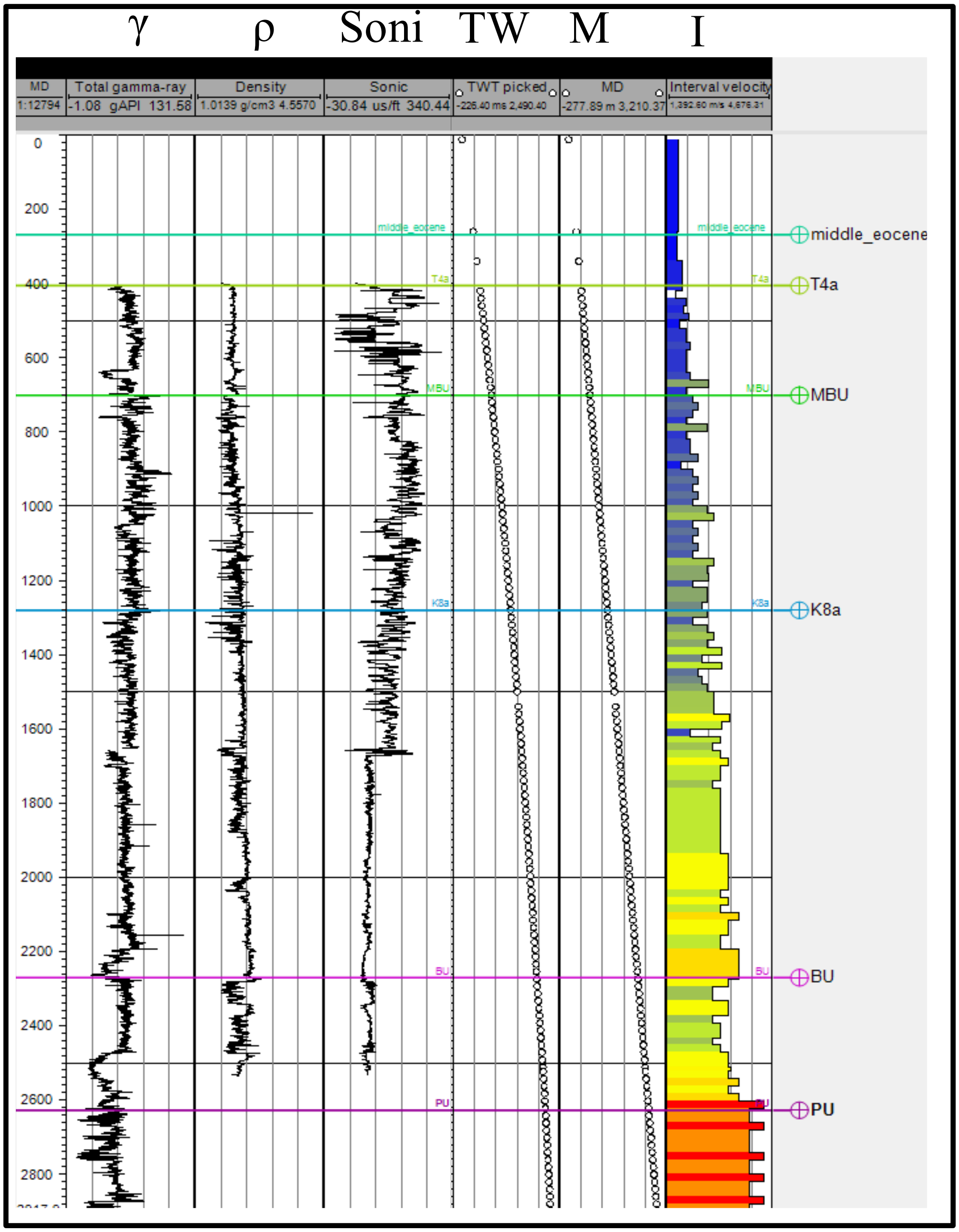

Figure 1.2.2 Crackerjack #1 OCS-Y-1320 well logs and well tops, from left to right: total gamma ray, density, sonic, two way traveltime, measured depth, interval velocity, and well tops. Location shown in Figure 3.3.1

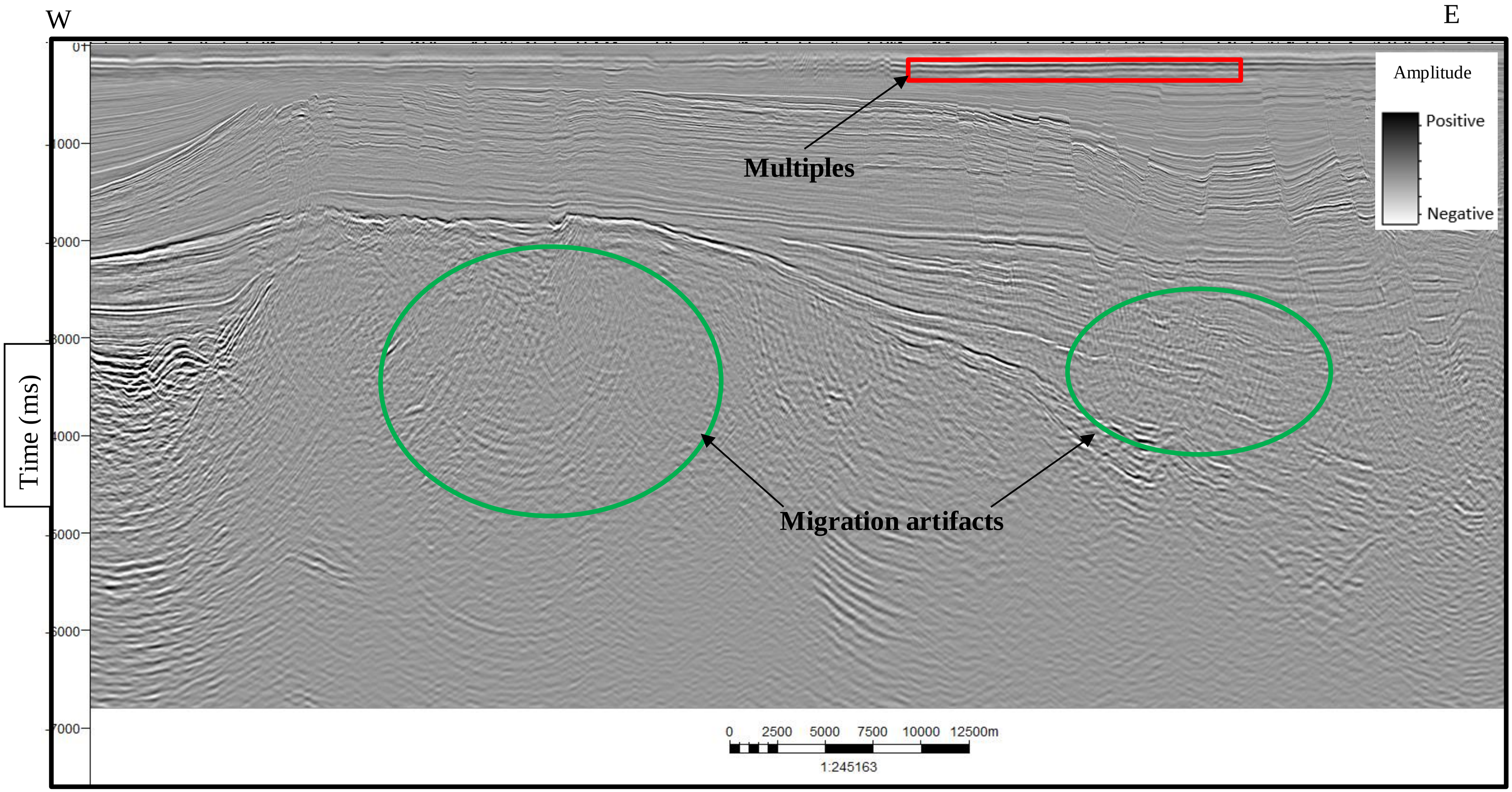

Figure 1.2.3 Line wcs-6057 in grey scale, examples of noise are outlined: migration artifacts (green), and multiples (red). Location shown in Figure 1.2.5.

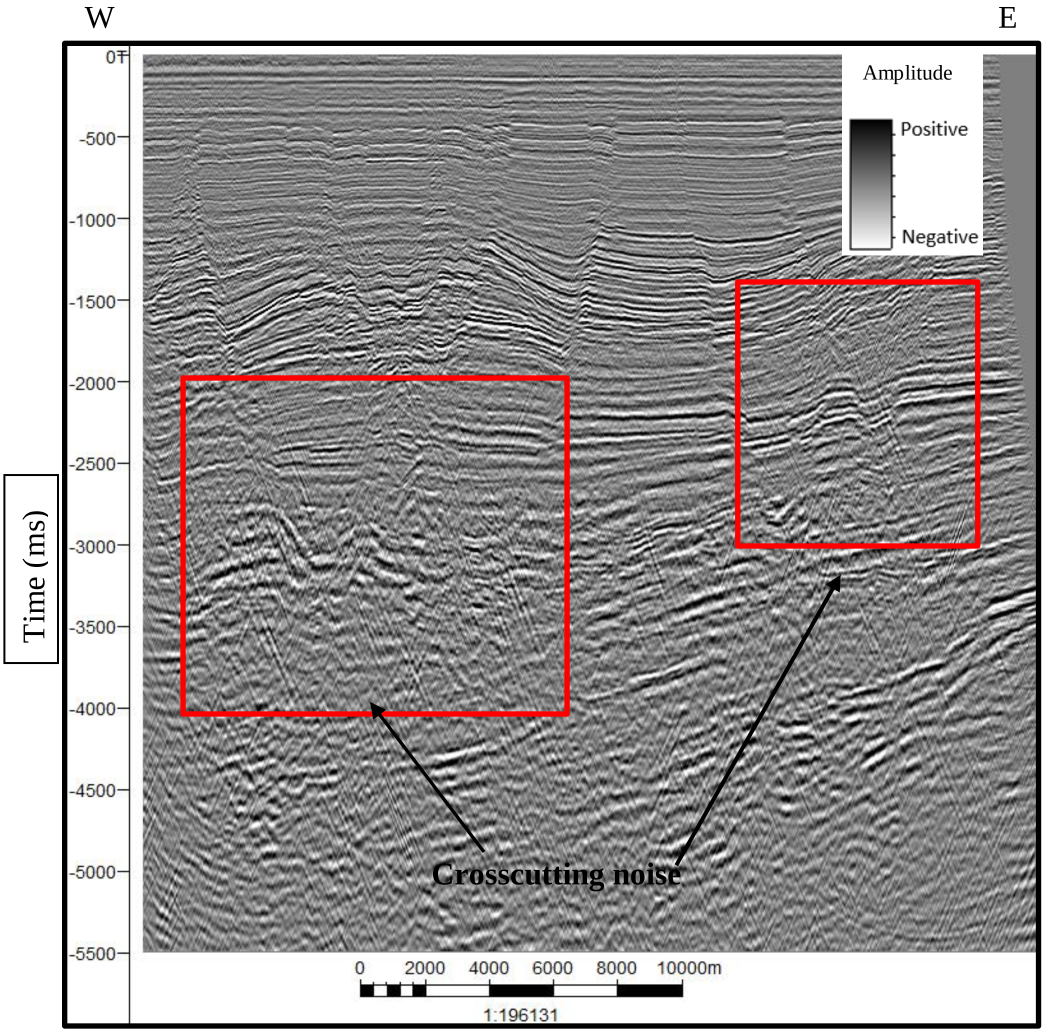

Figure 1.2.4 Line gp85_229_2 is clearly more contaminated by out of the plane noise than line wcs-6057. Location shown in Figure 1.2.5.

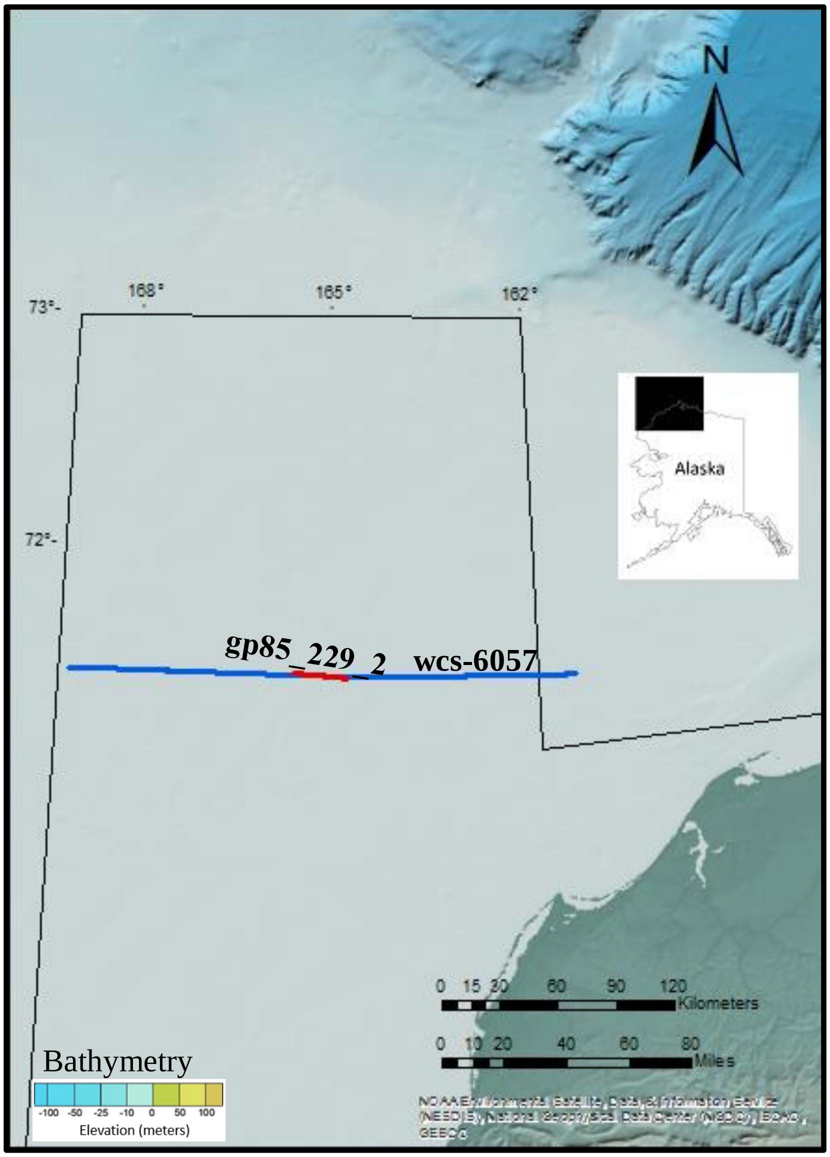

Figure 1.2.5 Position of lines wcs-6057 (blue) and gp85_229_2 (red). Topographic and bathymetric basemap from Jakobsson et. al, 2012.

1.3.Methods

1.3.1. Seismic stratigraphy

The interpretation approach in this work follows the methods developed by Vail et al. (1977) and summarized by Pigott and Radivojevic (2010), in which only seismic horizons that indicate discordances in the geological record, termed operational sequence boundaries are picked. The procedure of this investigation follows seven of the ten steps:

1. Selection of a representative seismic line of the area, which has a regional expression of the Geology, has geological well control, and has a known seismic wavelet interpretive phase and polarity.
2. Fault Interpretation: The importance of a proper fault interpretation lies on the facts that the faults are the "Tectonic Skeleton of the Basin" (Pigott, unpublished class notes, 2017), they provide the structural framework for the Petroleum System and with a proper interpretation of the faults correlation mistakes are minimized. The common criteria used in fault interpretation are :
    - Reflector offset
    - Reflector dip change
    - Amplitude Change
    - Fault plane reflections
3. Reflector terminations interpretation: Reflector terminations allow the determination of the limits of operational seismic sequences, and the relationship between adjacent seismic sequences.
4. Sequence boundaries interpretation: The boundaries of operational seismic sequences illustrate the type of unconformity between sequences. These unconformities are: toplap, erosional truncation, downlap and onlap (Mitchum, Vail, and Thompson, 1977).
5. Seismic facies analysis: After the different seismic sequences in the data have been separated by the interpretation of their boundaries, it is possible to observe seismic "packages" inside the sequences, if these packages, the amplitude, phase,

frequency, velocity and continuity are different from adjacent groups, these units are termed seismic facies. The depositional environment, energy of the deposition, and the potential lithologic content are parameters that can be interpreted from the seismic facies. (Mitchum et al.,1977).

6. Lithostratigraphy integration from the well control: The lithostratigraphic units observed in the well control are correlated to time significant reflectors in the data.
7. Integration and reiteration of the information into a geohistory analysis.

1.3.2. Fault mechanical stratigraphy

Once the faults have been interpreted, relative ages are assigned following Steno's law of superposition and cross cutting relations. The geomechanical principle that states that older rocks tend to be stronger and less prone to brittle deformation (Pigott and Abouelresh, 2016). The youngest strata affected by deep-seated faults represent the age of the fault. Since pressure P is equivalent to normal stress (Pigott and Abouelresh, 2016) and since:

$$K = \frac{\sigma}{\delta V / V}$$

then

$$K = \frac{-P}{\partial V / V} = \frac{-P}{Ev}$$

Where σ is normal stress, K is the bulk modulus, V is volume, P is the pressure, and Ev is the volumetric strain; this equation describes the increase of the bulk modulus with the increase of pressure (i.e. confining depth and geological age).

Young's modulus (E) and the Poisson's ratio (ν) in a homogenous isotropic solid are related by:

$$K(z) = \frac{E(z)}{3(1-2\nu(z))}$$

where in this case ν is a fixed parameter for the rock and E increases with increasing burial depth (age). As E increases so does K.

2. Geological Background

The Chukchi Sea Planning Area has an extension of approximately 49, 000 square miles in the continental shelf of northwestern Alaska (Thurston and Theiss, 1987) (Figure 2.1.1). Thurston and Theiss (1987) recognized six tectonic provinces and four major sedimentary basins in the area.

2.1.Structural Provinces of the Chukchi Sea

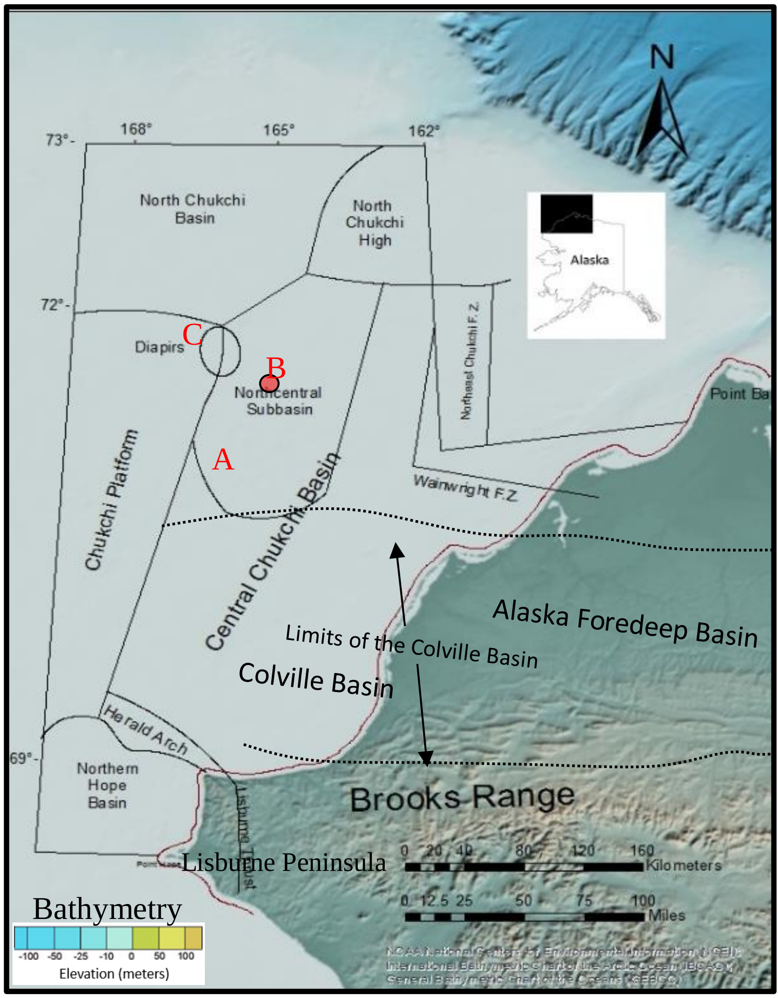

Figure 2.1.1 Structural provinces in the Chukchi Sea planning area. Topographic and bathymetric basemap from Jakobsson et al., 2012.

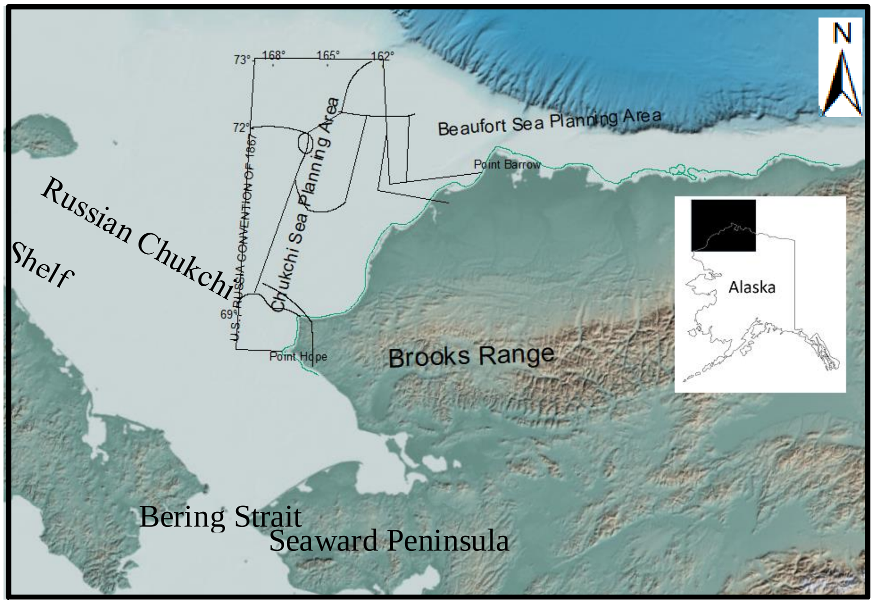

Figure 2.1.2 General view of the major structural limits of the Chukchi Sea planning area structural provinces.

2.1.1. Hope Basin

Hope Basin is located in the southeastern portion of the Chukchi Sea (Figure 2.1.1), with an E-W strike. The northwest coast of Alaska, and the Herald arch bound it on the north; northeastern Siberia rims it on the west; and Seaward Peninsula and the Bering Strait to the south (Figure 2.1.2) (Tolson, 1987).

The evolution of this basin consisted of three stages: isolated half grabens during the early Paleogene in response to transtensional movement of southeast-northwest-trending faults, thermal subsidence during the early Miocene and reactivation of the Eocene normal faults and generation of new faults during middle to late Miocene. (Tolson, 1987).

Deformed Brookian age rocks possibly compose the Acoustic Basement of the Hope Basin. A sedimentary prism of tertiary age, with a S-N provenance, fills the Hope Basin. (Grantz et al., 1975).

2.1.2. Herald Arch

The positive structural relief termed Herald arch is located in the southeast portion of the Chukchi Sea (Figure 2.1.1). It is bounded on the south by the Hope Basin, to the east by the Lisburne Peninsula, to the north by the Central Chukchi Basin (“Hanna Trough” in Serwood et al., 2002, and in Grantz et al., 1975), and to the west by the Chukchi Platform. (Thurston and Theiss, 1987; Grantz et al., 1975).

Herald arch is the result of reverse S-N thrusting along the Herald fault zone during the late Cretaceous until the Paleogene. Subsidence of the Hope basin in the middle Paleogene is another factor that contributed to the generation of this structural high, which attained its present form by the Neogene time. (Grantz et al., 1975).

From geological iferences and dredging studies by the University of Washington, the composition of the arch is suggested to be Franklinian (pre-Mississippian) argillite and greywacke, and Mississippian to Triassic clastics. The sedimentary cover of the arch is carbonate and chert of the Ellesmerian sequence in the southwest half of the arch, and Lower Cretaceous sandstone and shale is the lithology in the northwest half of the arch. (Grantz et al., 1975).

2.1.3. Chukchi Platform

On the western margin of the Chukchi Sea planning area there is a structural plateau termed the Chukchi platform (Figure 2.1.1), it is rimmed to the east by the Central Chukchi Basin and the Herald arch, to the north by the North Chukchi Basin, to the south by the Hope Basin, and it extends west into the Russian Chukchi Shelf. (Thurston and Theiss, 1987).

Rifting in the Central Chukchi Basin (“Hanna trough” in Grantz and Eittreim, 1979, and Sherwood et al, 2002), is responsible for the high structural relief, on the western margin of the Chukchi sea planning area, known as the Central Chukchi Platform, which forms the western flank of the rift. (Sherwood et al., 2002).

The Central Chukchi Platform is characterized by a shallowing of the Franklinian acoustic basement (1 to 1.25 km), and high angle normal faulting typical of a rift structure (Figure 2.1.1) (Grantz et al., 1984a). Ellesmerian sequences onlap on this structural feature, and subsequent Brookian sequences cover it.

2.1.4. Central Chukchi Basin (Hanna trough)

The Central Chukchi Basin is a structural trough, with a strike predominantly N-S (Figure 2.1.1). It is bounded on the south by the Herald Thrust, on the east by the Northeast Chukchi and Wainwright fault zones, on the west by the Chukchi Platform, and to the north by the North Chukchi basin and the North Chukchi High (Thurston and Theiss, 1987).

The Central Chuckchi basin formed because of a complex N-S rifting event during the Devonian until the Permian, with a subsequent regional sagging from Permian to Late Jurassic. Ellesmerian and Brookian sequences compose the sedimentary prism that filled this basin (Sherwood et al., 2002).

2.1.5. Colville Basin

The Colville Basin is located in the southern parts of the Central Chukchi Basin Figure (2.1.1) (below ~70° N). It is bounded to the south by the Herald Arch, to the north by the Central Chukchi Basin, to the east by the Chukchi Platform (Thurston and Theiss, 1987).

The sediments of this basin are of Brookian age and were deposited in the Colville Geosyncline. These sediments display compressional folding and faulting, product of the Brookian orogeny. (Thurston and Theiss, 1987).

2.1.6. Northcentral Subbasin

On the northern portion of the Central Chukchi Basin, there is a subbasin of Late Cretaceous-Tertiary age (Figure 2.1.1). This basin trends roughly N-S and it merges with the Central Chukchi Basin to the north. (Thurston and Theiss, 1987).

Transtentional stresses in the Hanna wrench fault zone are a possible explanation for the origin of this subbasin. Brookian sediments fill this basin. (Thurston and Theiss, 1987).

2.1.7. North Chukchi Basin

This basin is located in the northwestern portion of the Chukchi Sea planning area (Figure 2.1.1), and is bounded to the south by the Chukchi Platform and the Central Chukchi Basin, and to the West by the North Chukchi High. (Thurston and Theiss, 1987).

An extension of the rifting from the Beaufort continental margin to the North Chukchi Shelf, during Early to Late Cretaceous, and Late Cretaceous to Quaternary thermal sagging created the North Chukchi Basin (Sherwood et al. 2002). Brookian and Ellesmerian strata compose the filling of this basin. (Thurston and Theiss, 1987).

2.1.8. North Chukchi High

The North Chukchi High is located on the northcentral part of the Chukchi Sea planning area (Figure 2.1.1). The Central Chukchi Basin bounds it on the south, and the North Chukchi Basin to the west and northwest. The North Chukchi high is a structural uplift, remnant of the Early to Late Cretaceous rifting event, the lower Brookian units, which cover this structural uplift, display compressional structural styles such as concentric folds (Sherwood et al., 1992) (Johnson, 1992).

2.1.9. Wainwright Fault Zone

This is a west-northwest-trending fault zone, located east of the Central Chukchi basin extending onshore into the NPRA (Figure 2.1.1). It is truncated or joined to the northeast by the Northeast Chukchi fault zone. (Thurston and Theiss, 1987). These are normal faults pre-Permian in age, with a down to the south displacement. (Thurston and Theiss, 1987).

2.1.10. Northeast Chukchi Fault Zone

The Northeast Chukchi Fault zone is located in the northeast portion of the Chukchi Sea planning area (Figure 2.1.1), extending beyond this area to the northeast. It limits to the south with the Wainwright fault zone and to the east with the Hanna wrench fault zone and the North Chukchi High.

The faults in this province juxtapose Late Devonian or older strata against Mississippian to Permian units, with a down-to-the-west relative displacement. (Thurston and Theiss, 1987).

2.1.11. Hanna Wrench Fault Zone

In the central Chukchi basin, the North Chukchi high, the Northcentral subbasin, and the Chukchi platform, wrench-faulting structures are interpreted (Figure 5.2.1). There are four main styles of deformation in this zone: depressions or structural sags in the Northcentral subbasin, structural uplift in the North Chukchi high, local structural doming, and positive and negative flower structures throughout the area. (Thurston and Theiss, 1987).

2.2.Stratigraphy

The rocks underlying the Chukchi shelf consist of four major stratigraphic units: Franklinian, Ellesmerian, Rift and Brookian (Figure 2.2.2). The age range in these units is from the Late Devonian and older (Franklinian), up to the Quaternary (late Brookian). (MMS, 2006). Sedimentary rocks constitute the lithology in these units, both carbonates and siliciclastic rocks are present. (MMS, 2006).

2.2.1. Franklinian Sequence

Thurston and Theiss (1987) interpreted the Franklinian sequence as the acoustic basement in the Chukchi Sea planning area (Figure 2.2.2). Highly deformed flysch and metamorphosed rocks are the inferred lithology. (MMS, 2006).

2.2.2. Ellesmerian Sequence

This sequence overlays unconformably the Franklinian sequence in the central Chukchi basin (Hanna trough); onlaps are observed (Thurston and Theiss, 1987) (Figure 2.2.2). Carbonates and shales are observed in the Lower Ellesmerian sequence; shale, sandstone, siltstone and conglomerates are present in the upper ellesmerian sequence. (MMS, 2006).

2.2.3. Rift Sequence

In the middle-Jurassic a second rifting episode along the Beaufort continental margin generated grabens and flexural downwraps, these structural lows were filled by a thick clastic sequence (Figure 2.2.2), probably of local provenance and recycled from the Ellesmerian sequence. Siltstone, sand conglomerates, and shale compose the lithology.

2.2.4. Brookian Sequence

An E-W trending orogeny, termed the Brookian orogeny, with a S-N general direction of thrust, shifted the sedimentation patterns in the Chukchi shelf; the provenance of the sediments became predominantly southward (Figure 2.2.2). These sediments were derived from the structural uplifts created in the orogeny. Shales, siltstones, sandstones, and conglomerates are present in the lithology.

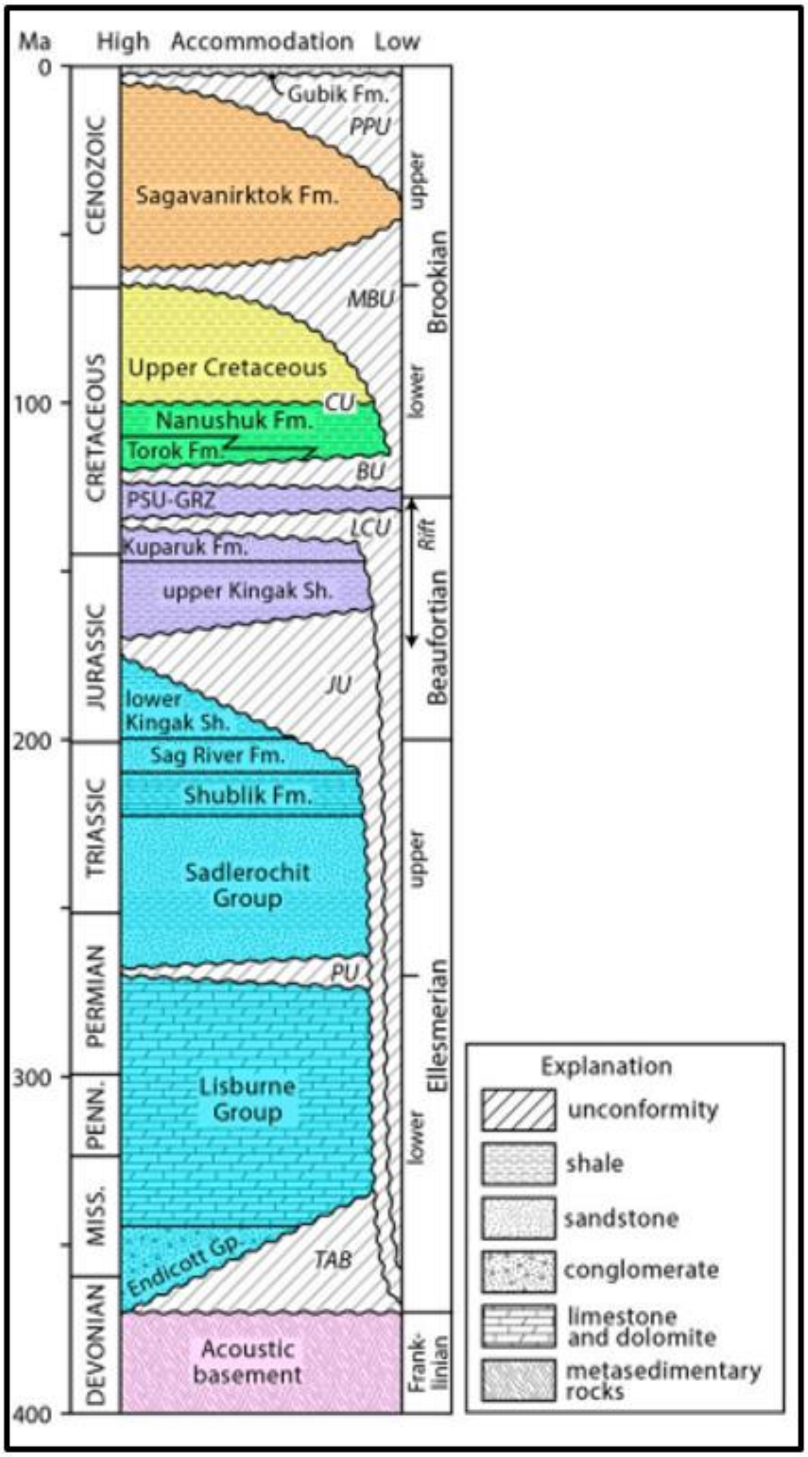

Figure 2.2.1 Regional stratigraphy of the Chukchi Sea planning area, from Craddock and Houseknecht, 2016.

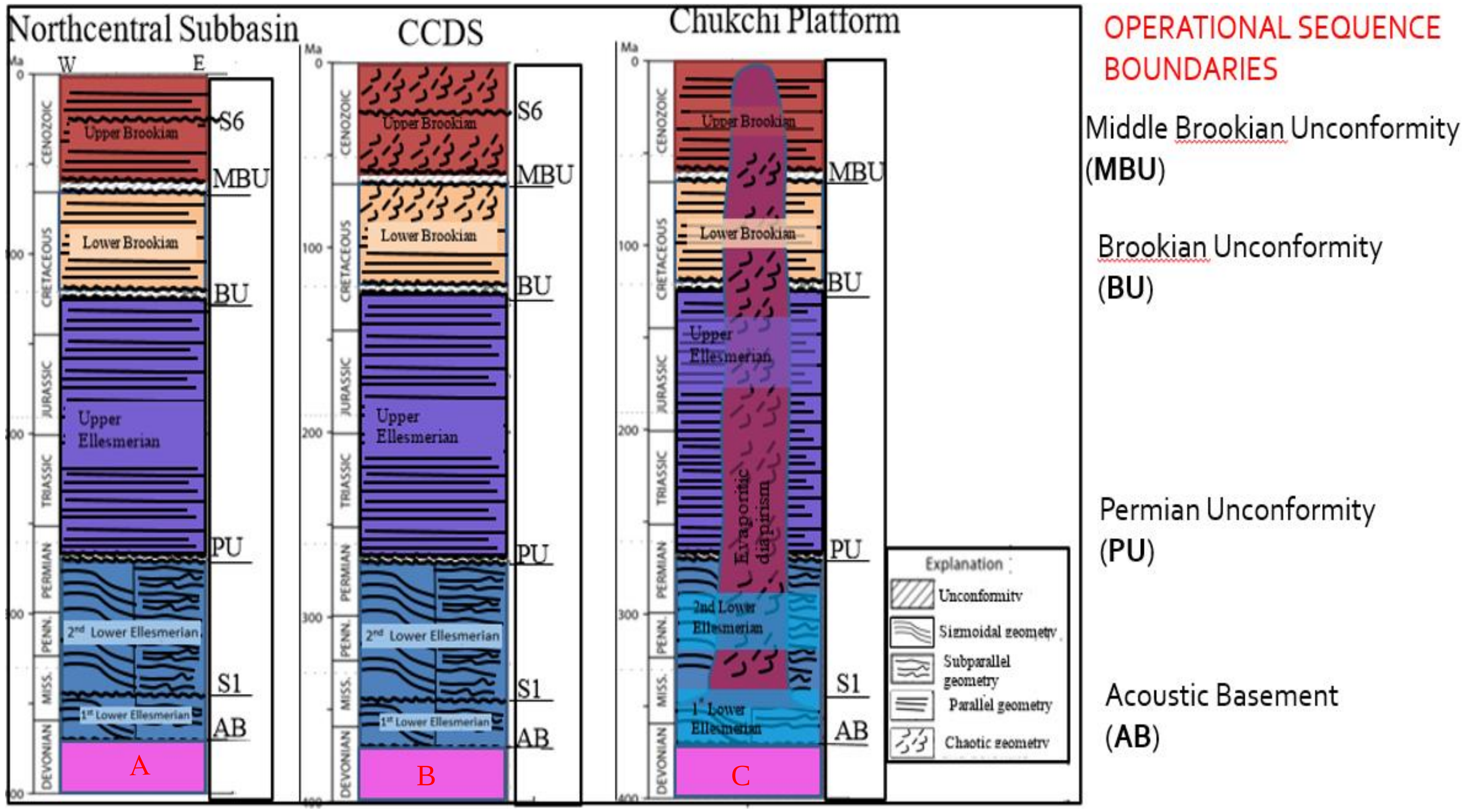

Figure 2.2.2 Schematic seismic interpreted stratigraphic columns of the Northcentral Subbasin, CCDS area, and the Chukchi platform. Modified after Craddok and Houseknecht, 2016. Location shown in Figure 2.1.1.

3. Observations

The seismic stratigraphic method and fault mechanical stratigraphy analysis, attribute assisted and corroborated with well data were used to determine the possible geological relation or discrepancy of the CCDS with its surroundings.

Fault mechanical stratigraphy and fault interpretation are related concepts but differ: fault interpretation is necessary to obtain a proper interpretation of the operational sequence boundaries, and it is a fundamental step in the seismic stratigraphic method; as for fault mechanical stratigraphy, the analysis is performed after the operational sequence boundaries and their ages are described. The purpose of fault mechanical stratigraphy analysis in this work was to obtain an approximate of the geological ages of the faults, not just the relative ages of the faults. Thus, the description of the operational sequence boundaries and its correlation with well data precedes fault mechanical stratigraphy.

The seismic attributes used in this work, their parameters, and the observations derived from them are described and summarized in this chapter. Amplitudes are displayed using “North Sea polarity,” (Bacon et al., 2003) i.e. negative reflector coefficients are bright (red and yellow).

3.1.Fault interpretation procedure.

Fault interpretation was performed by applying the concepts described in the introduction of this work and with the assistance of seismic attributes: variance, and cosine of phase (Pigott et al., 2013).

Fault planes were interpreted by systematically picking faults on regional lines such as wcs-6057 (Figure 3.1.1) and wcs-6063 (Figure 3.1.2), where the whole extent of the Central Chukchi Basin and adjacent major structural features can be observed (e.g.

Chukchi Platform). After faults are picked on these regional lines, faults are interpreted in adjacent parallel lines, i.e. examining the possible continuity of the faults from line to line by the examination of the geometry, relative age, throw, and associated structures (horsts, grabens, wrench faults, etc.). By following this procedure, it was possible to obtain the pseudo 3D geometry of the faults (Figure 3.1.6), the pseudo 3-D geometry of the faults associated with the CCDS (Figure 3.1.7) is important to assess possible geological models that could fit the observations.

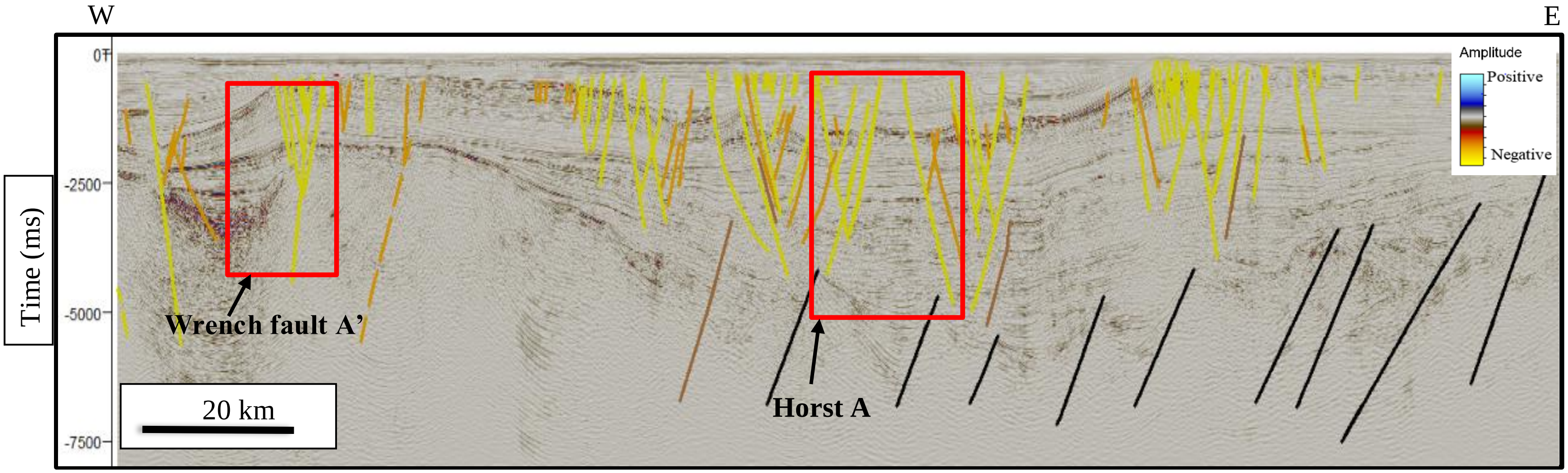

Figure 3.1.1 Fault interpretation on line wcs-6057, color of the fault are representative of the geological age of the fault. Location shown in Figure 3.1.4.

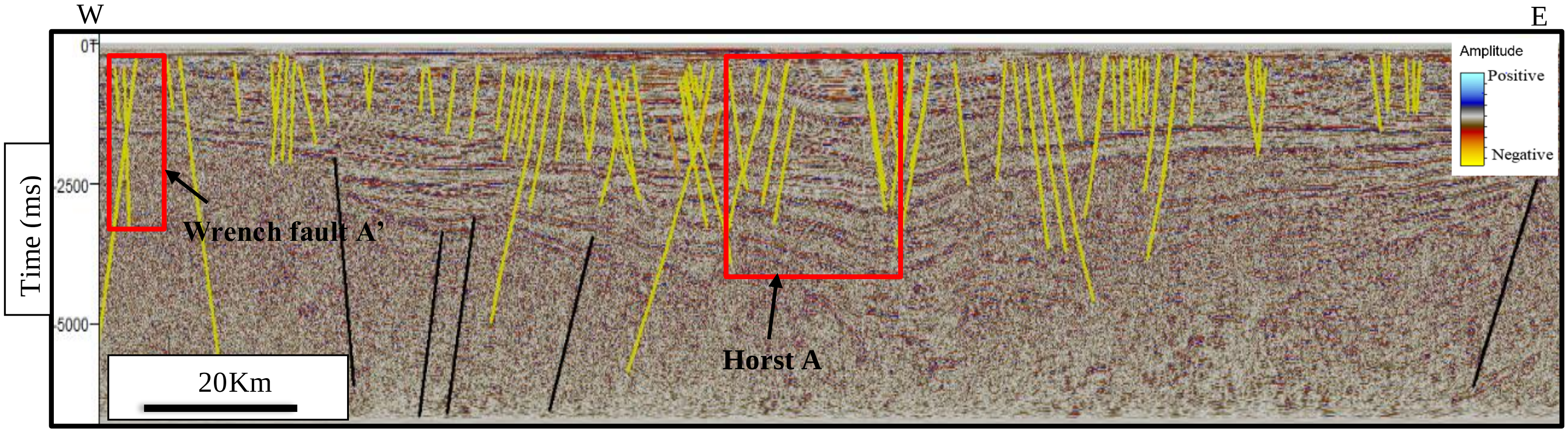

Figure 3.1.2 Fault interpretation on line wcs-6063, color of the fault are representative of the geological age of the fault. Location shown in Figure 3.1.4

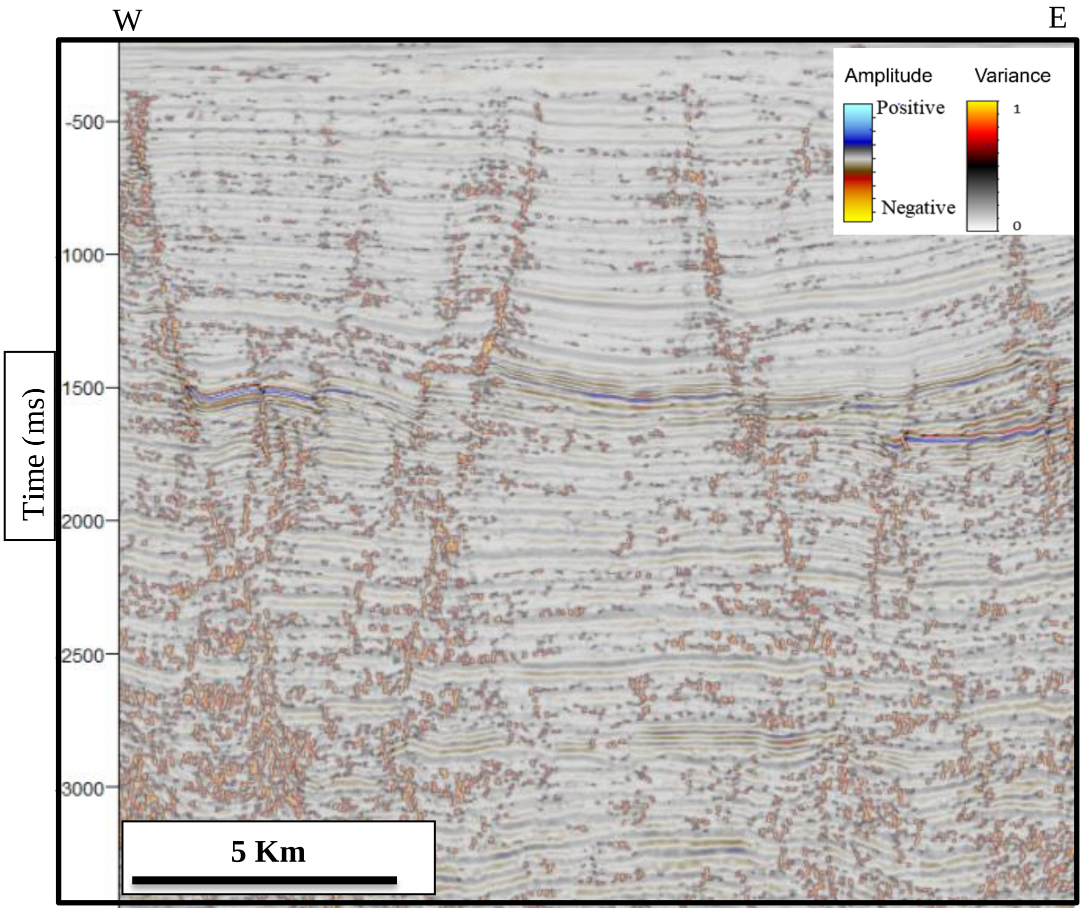

Figure 3.1.3 Close up on structure "Horst A" on line wcs-6057(Seismic amplitude co-rendered with variance at 70% transparency). Location shown in Figure 3.1.4

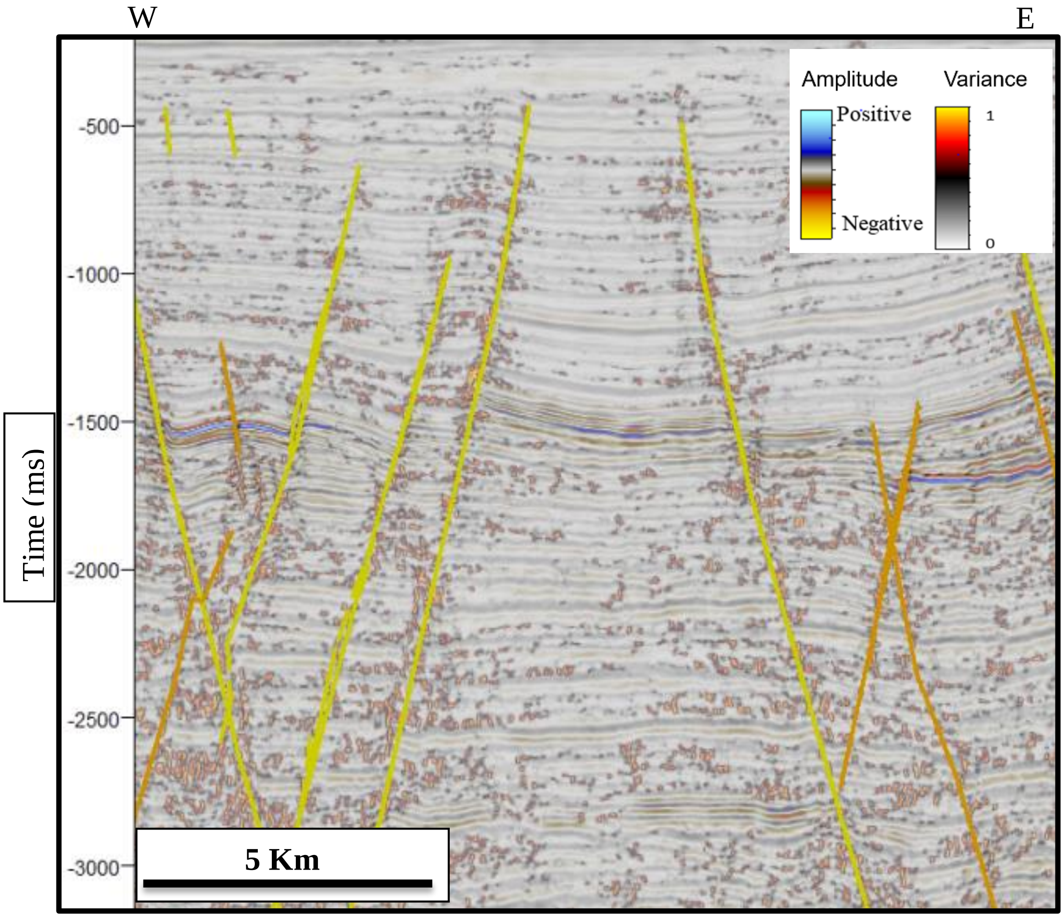

Figure 3.1.4 Fault interpretation of structure "Horst A" and adjacent faults on a portion of line wcs-6057 (seismic amplitude co-rendered with variance at 70% transparency) color of the fault is representative of the geological age of the fault. Location shown in Figure 3.1.5.

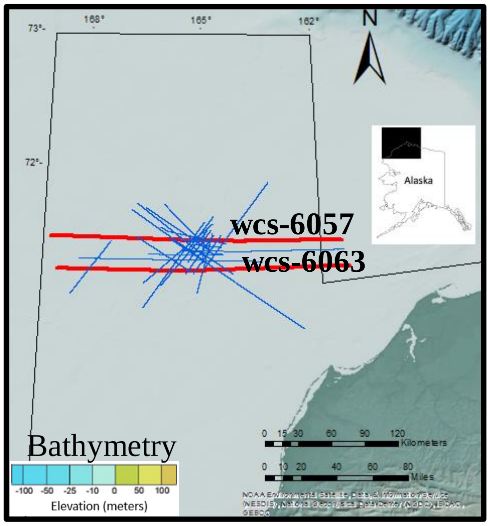

Figure 3.1.5 Locations of lines wcs_6057 and wcs_6063 (red).

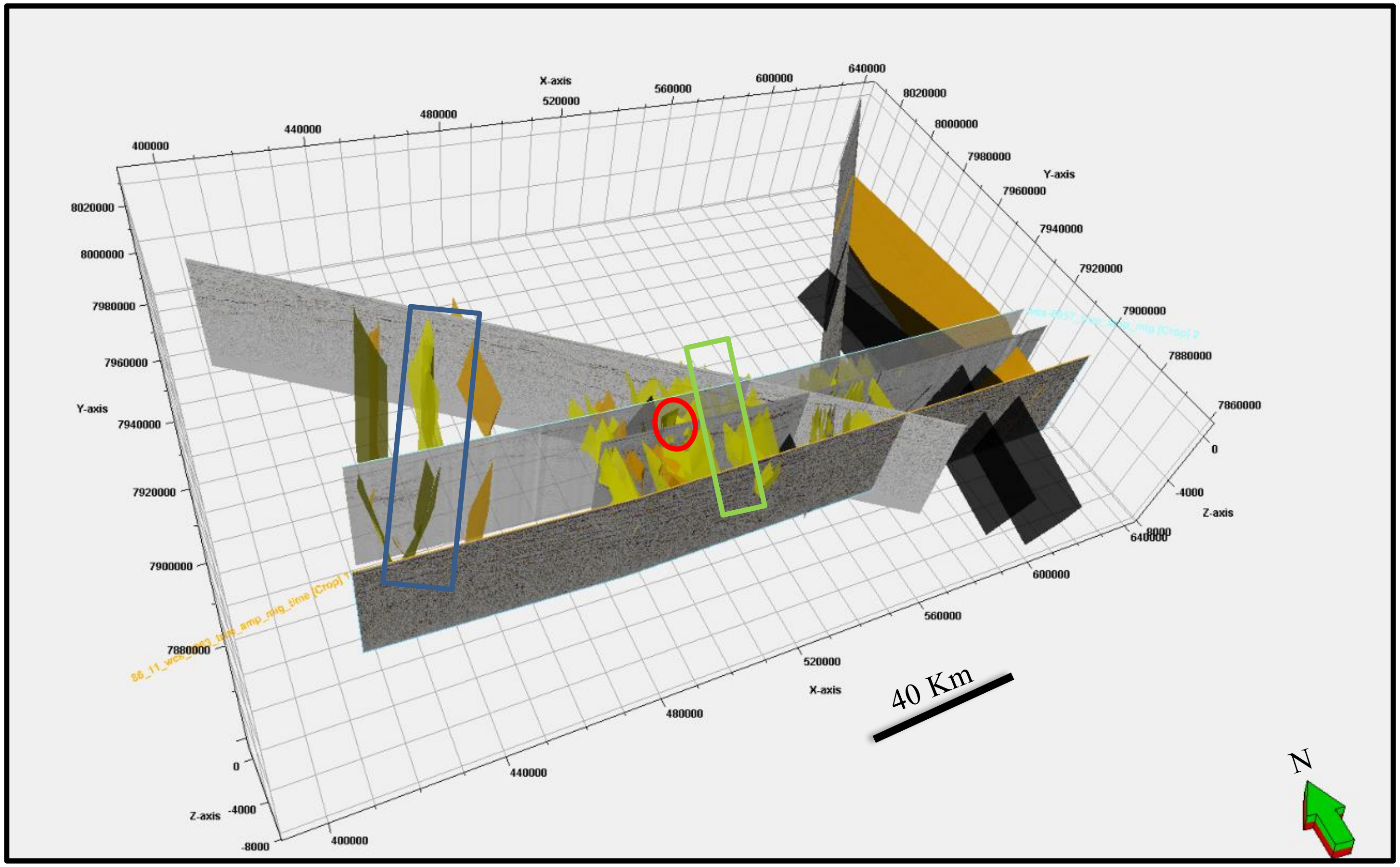

Figure 3.1.6 Pseudo 3-D geometry showing seven seismic lines and major faults in the area; area of the structure outlined by red ellipse, Wrench fault A' outlined by the blue rectangle (west), and Horst A outlined by green rectangle (east). Regionally sigma 3 stresses are dominantly E-W trending (color of the fault is representative of the geological age of the fault.

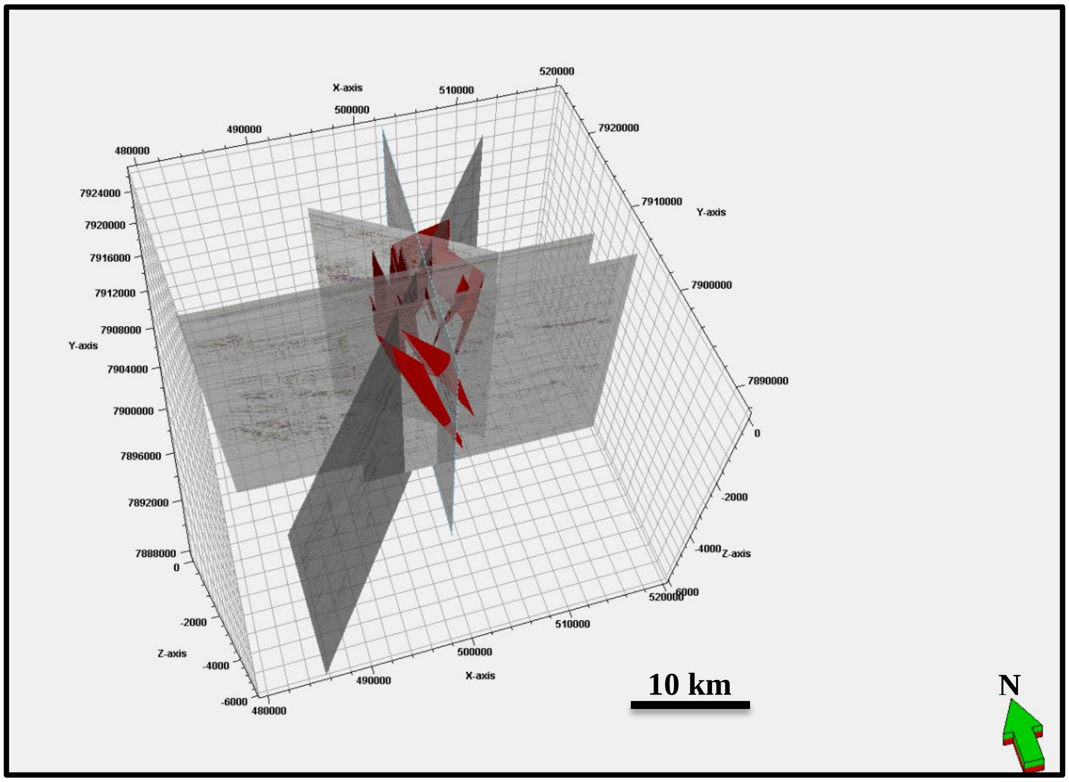

Figure 3.1.7 Pseudo 3D geometry of the faults related to the structure along with seismic: line wcs-6059 W-E, line sc86-8459 N-S, line ch83-104a NE-SW, line d85-o-m2, line ch83-104a (SE-NW), and line d84-29b (NW-SE) sigma 3 stresses are horizontal and radial (color of the fault is representative of the geological age of the fault).

3.2. Operational sequence boundaries interpretation.

After the faults were interpreted, operational sequence boundary interpretation followed. The procedure to interpret the operational seismic sequences was to mark terminations in regional seismic sections with an apparent dip view (W-E, NW-SE), trace the reflectors defined by the terminations through the section, and interpret the operational sequence boundaries in perpendicular strike-view lines crossed by dip lines at several points. This procedure was useful in tracing operational sequence boundaries on relatively short dip lines where no terminations were visible.

The seismic stratigraphic analysis was performed on 26 of the 111 2D seismic lines (Figure 3.2.1); six operational seismic sequences were recognized in this analysis.

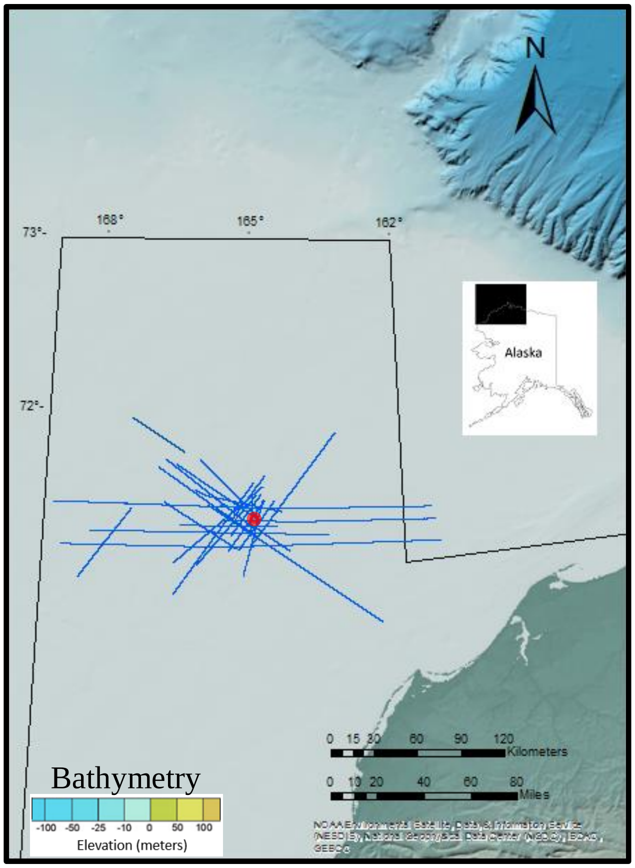

Figure 3.2.1 Position of the 26 lines utilized for seismic stratigraphic and fault mechanical stratigraphy analysis, area of the CCDS red circle.

3.2.1. Acoustic Basement

Commonly the acoustic basement exhibits high amplitude and is the lowermost continuous reflector. Downlapping and onlapping characterize the upper boundary, and migration artifacts are present below this reflector (Pigott unpublished class notes, 2017).

In the data examined in this work, the seismic horizon defining the acoustic basement was recognized by a high amplitude continuous-reflector where the structural elevation was relatively high (Chukchi Platform). In the basin, the acoustic basement is deeper and the reflections dimmer, possibly due to obscuring by the basin infill. In this case the acoustic basement was picked as the lowermost continuous reflector with onlapping and downlapping on top (Figures 3.2.2 and 3.2.3).

The seismic facies below the acoustic basement vary, in most of the cases they were characterized by chaotic reflectors, with relatively high amplitude, low frequency isolated reflectors, apparent migration artifacts ("smiles"), and sideswipe (Figure 3.2.2).

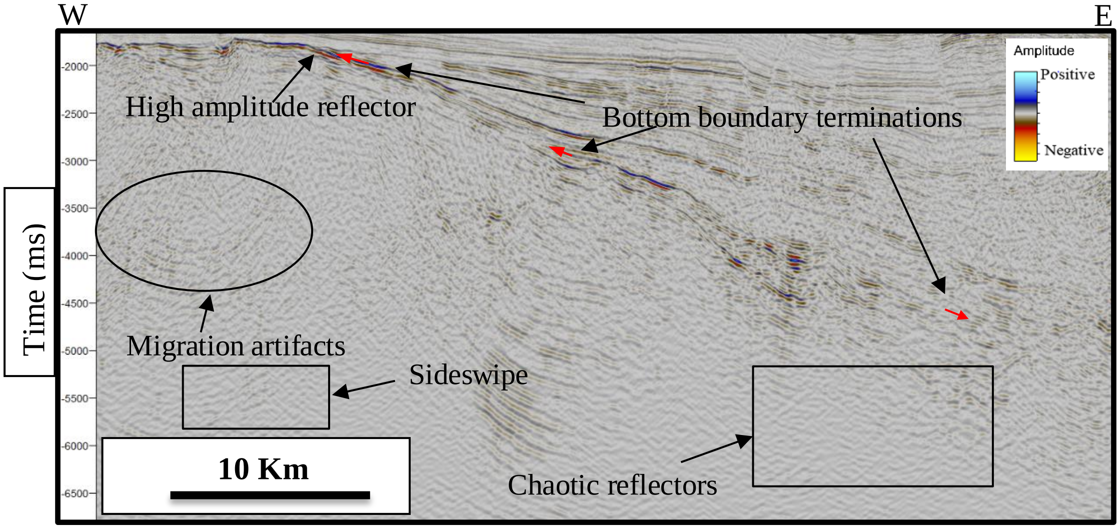

Figure 3.2.2 Characteristic elements of the Acoustic Basement on line wcs-6057. Location shown in Figure 3.2.28.

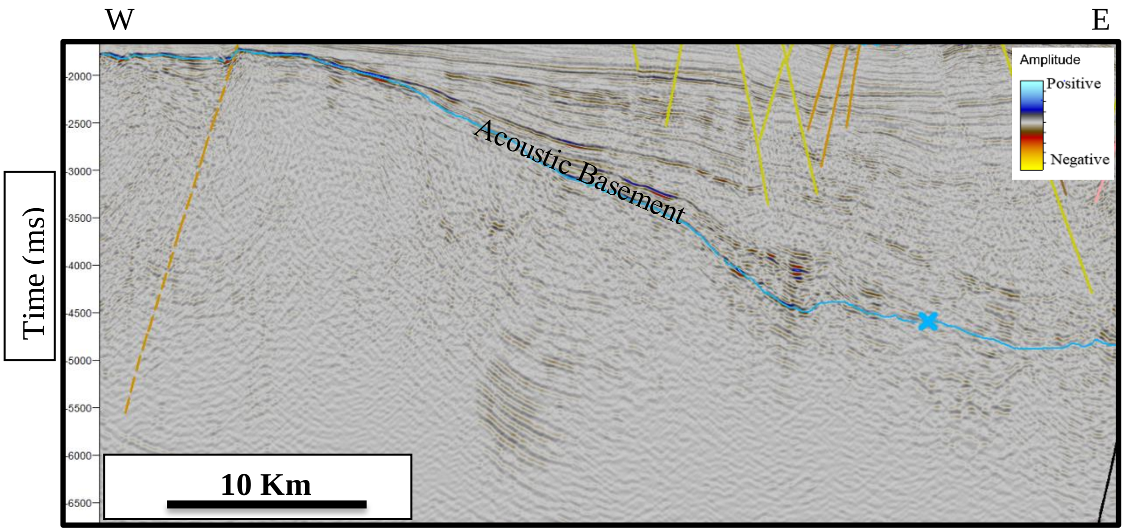

Figure 3.2.3 Interpretation of the Acoustic Basement on line wcs-6057. Location shown in Figure 3.2.28, (color of the fault is representative of the geological age of the fault).

3.2.2. S1

Toplap and downlapping in W-E, and NW-SE seismic lines define this operational sequence boundary, such as on seismic lines wcs-6057 and wcs-6063, where the whole extent of this operational sequence boundary can be observed. S1 onlaps the acoustic basement at the Chuckchi platform on the west.

The seismic facies of the 1st Lower Ellesmerian exhibit a sigmoidal geometry with variable amplitude and constant frequency at the onlap on the Chukchi Platform (Figures 3.2.4 and 3.2.5); the facies gradually change basinward, expressing a subparallel/mounded morphology (Figures 3.2.6 and 3.2.7).

The geometry of the facies are concordant with the apparent structural regime. Sigmoidal facies in the western end of the 1st Lower Ellesmerian indicate a low energy environment with relatively rapid basin subsidence (Mitchum et al., 1977). The basinward subparallel reflection patterns indicate constant deposition rates in a uniformally subsiding environment. The parallel geometries in the eastern end of the operational sequence could reflect a stable basin plain depositional environment (Mitchum et al., 1977).

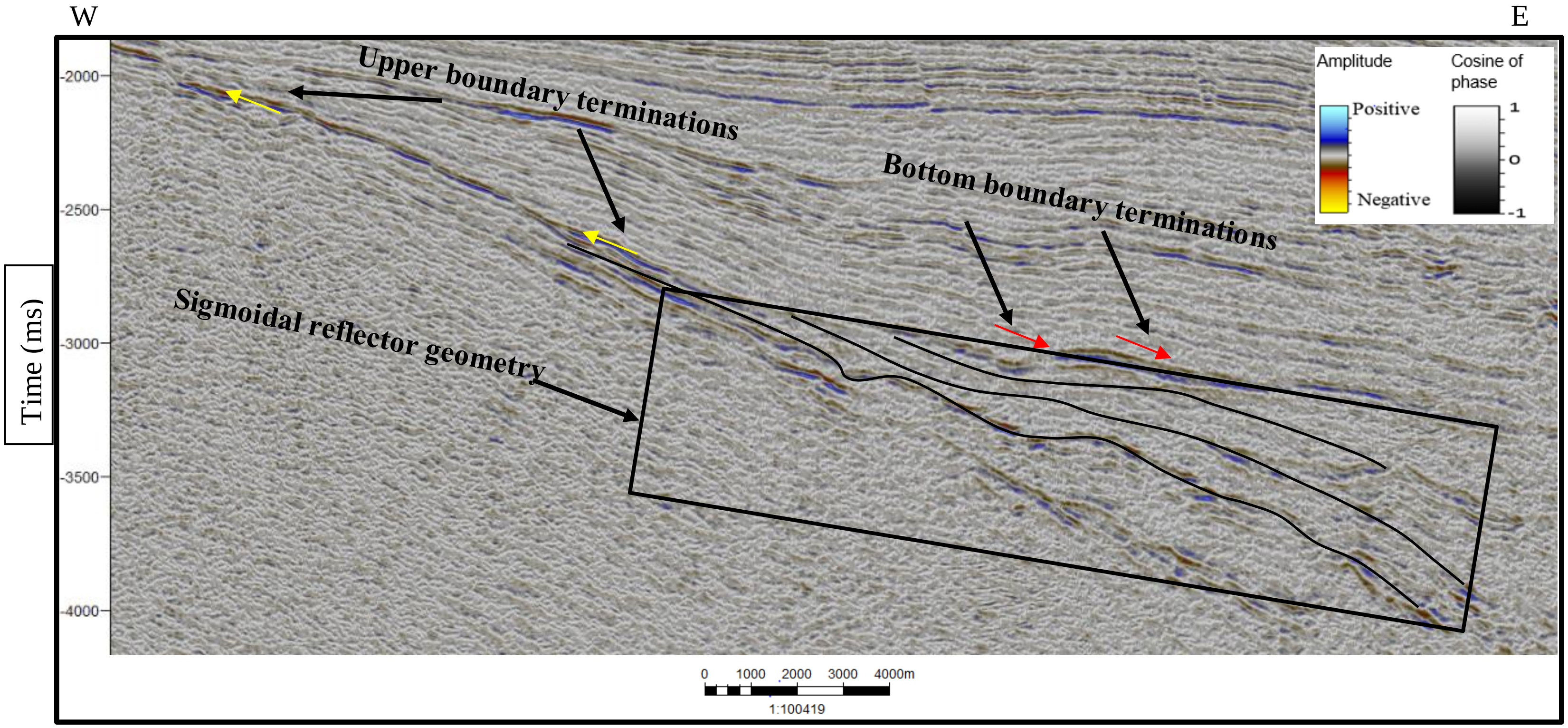

Figure 3.2.4 S1 Operational Sequence Boundary elements, and 1st Lower Ellesmerian reflectors' geometry (Seismic amplitude co-rendered with cosine of phase at 80% transparency). Location shown in Figure 3.2.28.

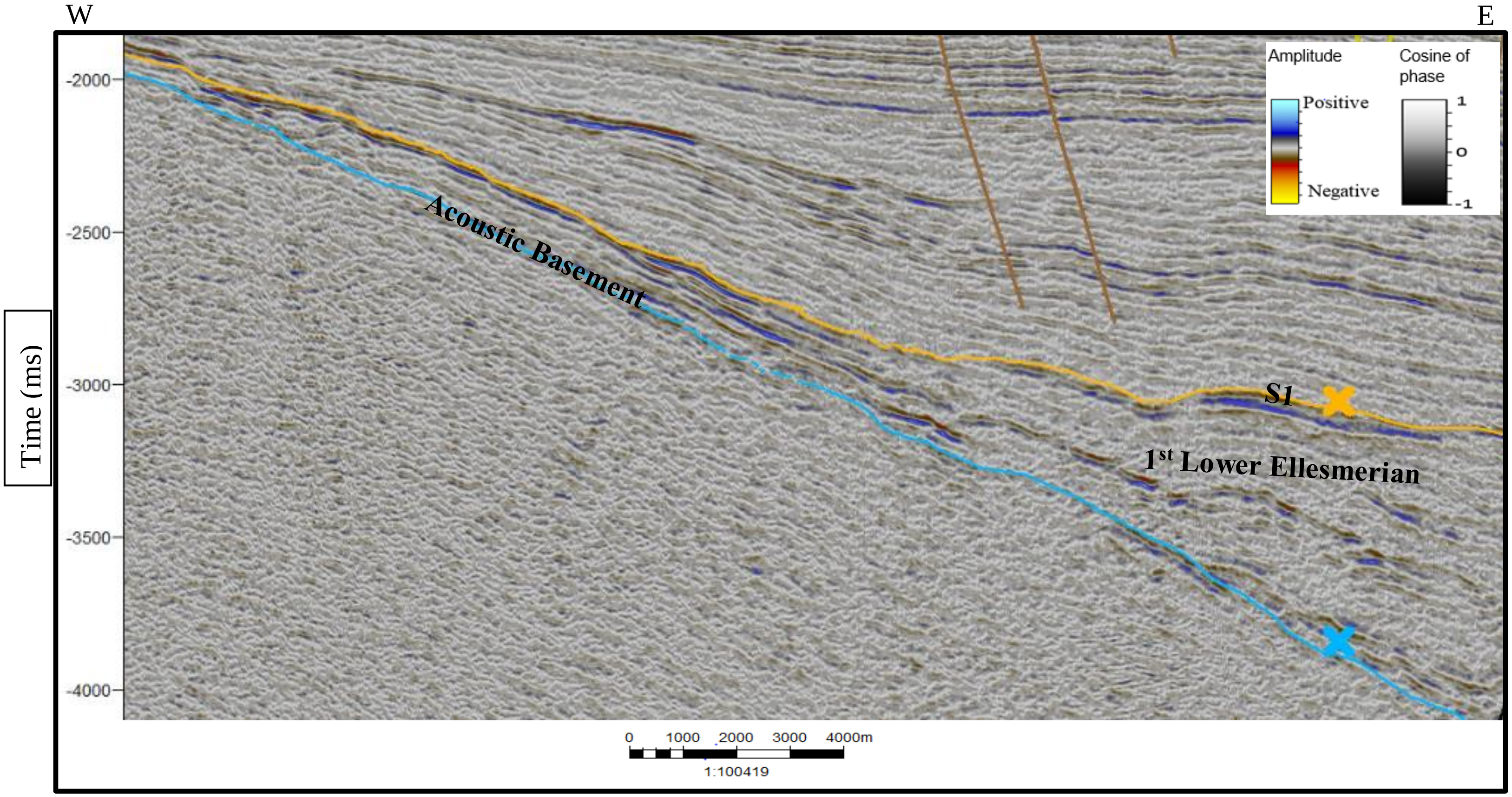

Figure 3.2.5 Interpretation of the S1 operational sequence boundary (Seismic amplitude co-rendered with cosine of phase at ~80% transparency). Location shown in Figure 3.2.28, (color of the fault is representative of the geological age of the fault).

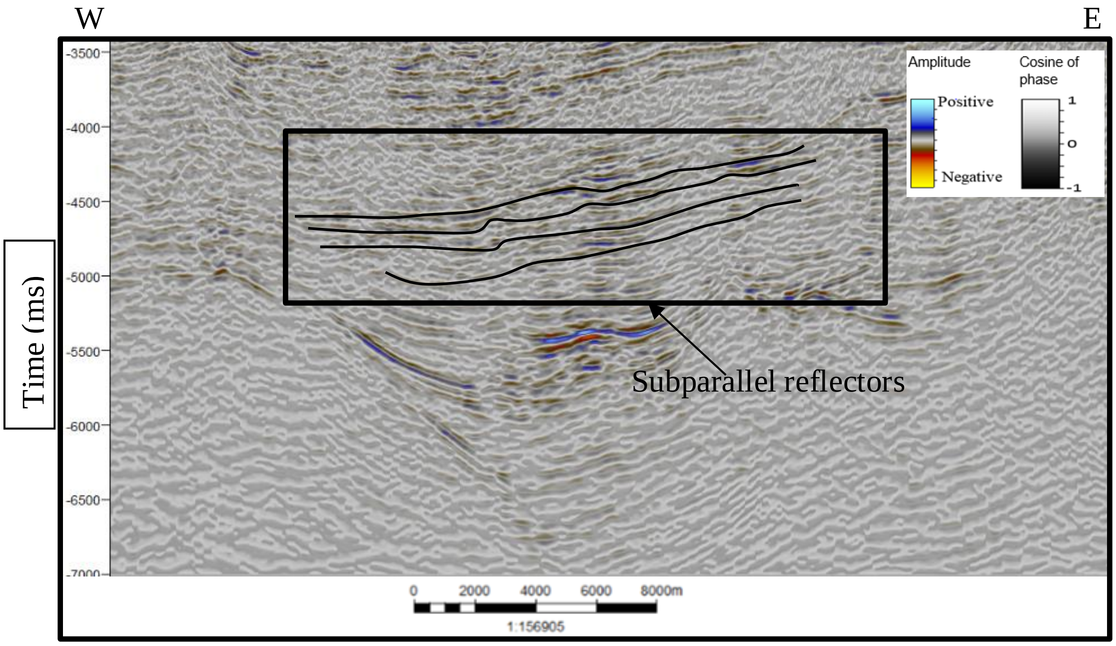

Figure 3.2.7 Subparallel reflector geometry of the 1st Lower Ellesmerian, line wcs 6059 (Seismic amplitude co-rendered with cosine of phase at 80% transparency). Location shown in Figure 3.2.28.

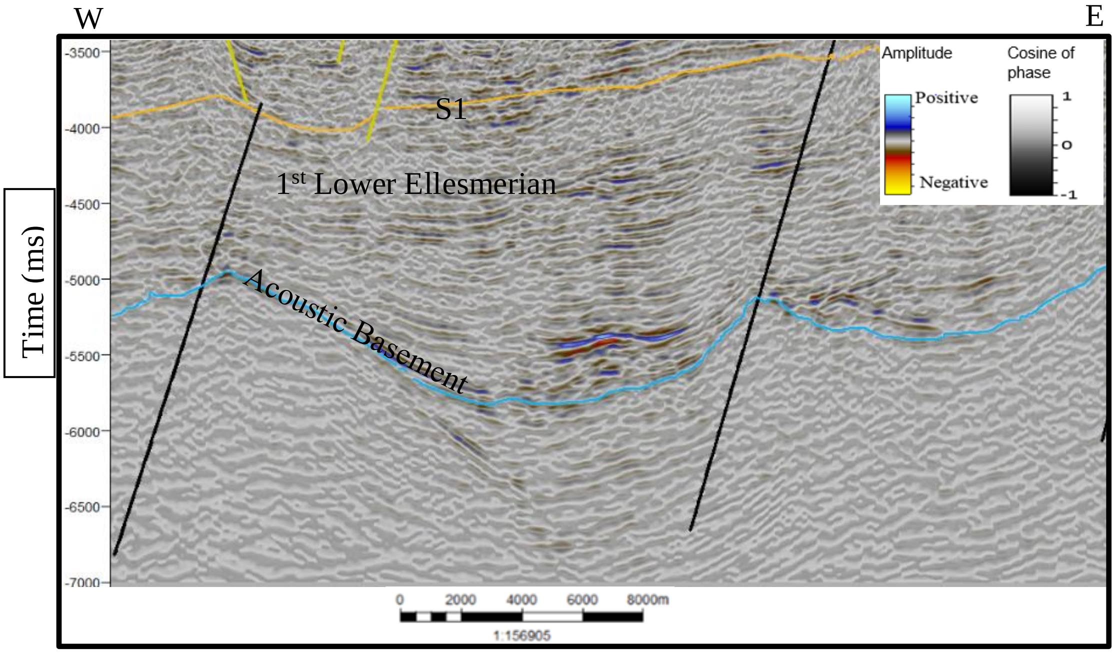

Figure 3.2.6 Interpreteation of the 1st Lower Ellesmerian, line wcs 6059 (Seismic amplitude co-rendered with cosine of phase at 80% transparency). Location shown in Figure 3.2.28 (color of the fault is representative of the geological age of the fault).

3.2.3. Permian Unconformity

Toplap defines the Permian Unconformity in the W-E and NW-SE seismic sections; and similar to *S1*, the whole extent of this operational sequence boundary can be observed on regional dip lines.

Seismic facies of the 2nd Lower Ellesmerian are sigmoidal of variable amplitude and constant frequency close to the onlap with the Central Chukchi platform (Figures 3.2.8 and 3.2.9), basinward the facies are subparallel (Figures 3.2.10 and 3.2.11). On the eastern end at the Arctic platform, the facies are predominantly subparallel of variable amplitude with constant frequencies .

Sigmoidal facies of the 2nd Lower Ellesmerian at the Chukchi platform indicate that at the time this operational sequence was being deposited, relatively rapid subsidence was still affecting the Central Chukchi basin. Subparallel geometries at the basin indicate a stable subsidence, and the parallel geometries in the eastern end of this operational sequence indicate deposition on a stable shelf (Mitchum et al., 1977).

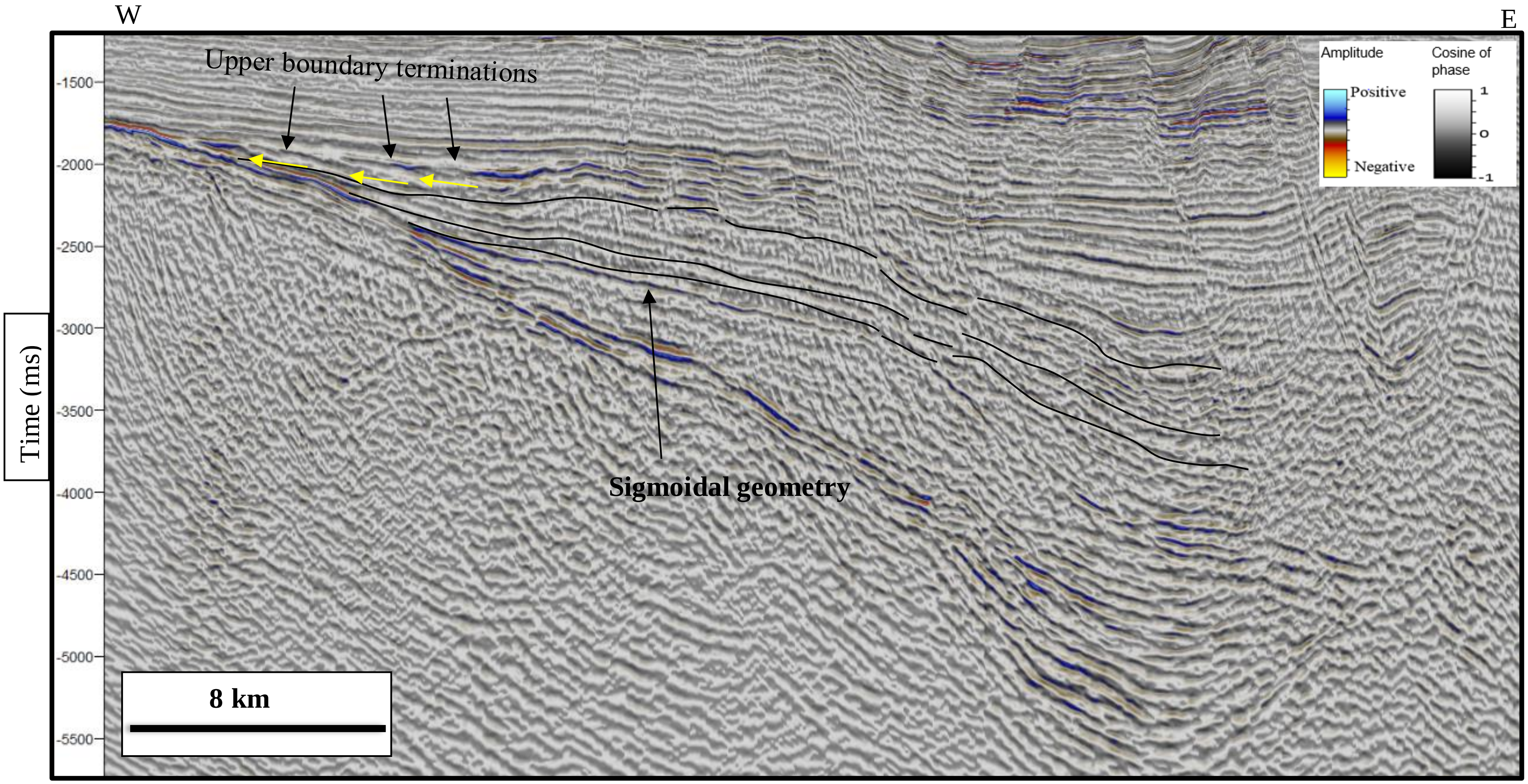

Figure 3.2.8 Upper boundary terminations defining the Permian Unconformity, and Sigmoidal reflector geometry of the 2nd Lower Ellesmerian on line ch90-001b (seismic amplitude co-rendered with cosine of phase at 80% transparency). Location shown in Figure 3.2.28.

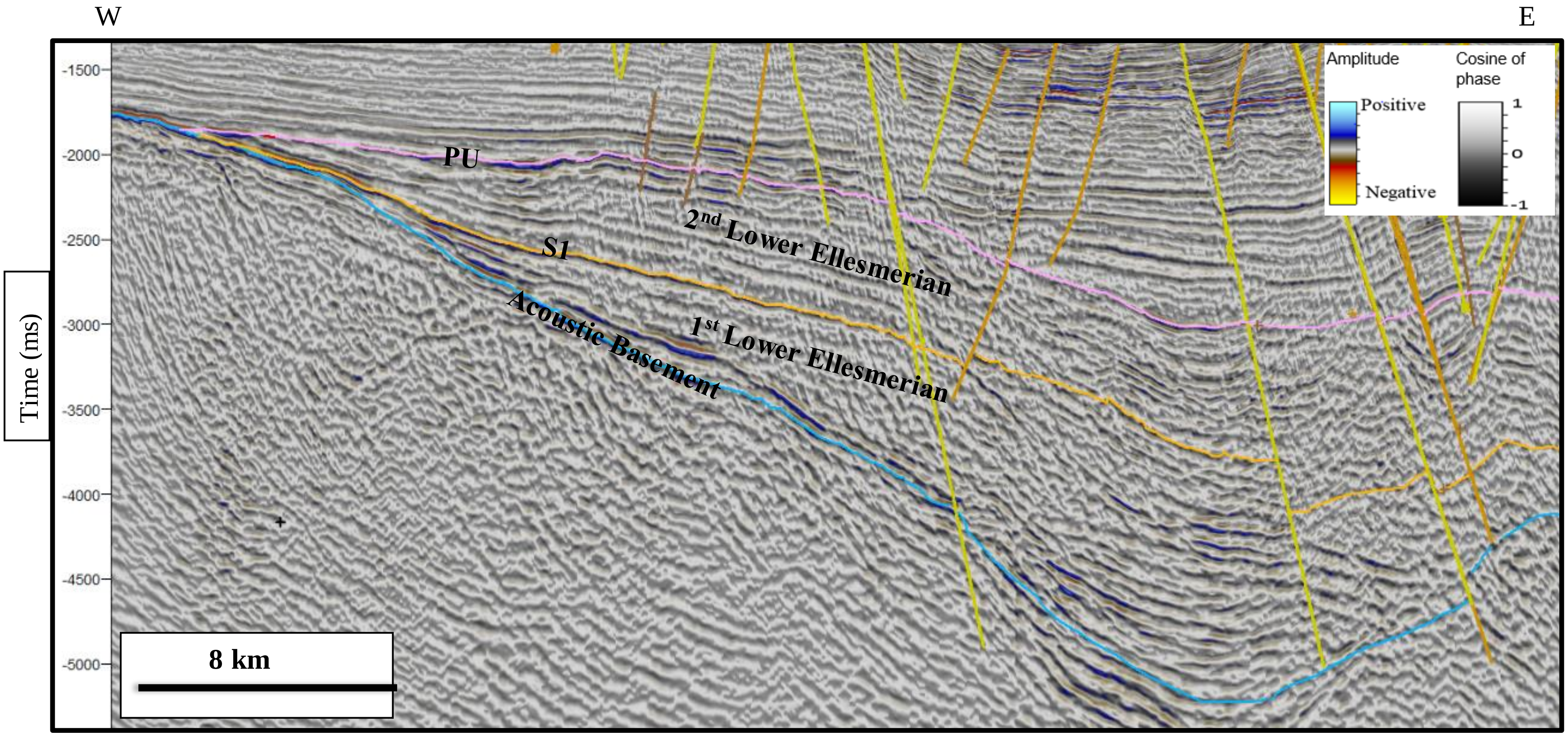

Figure 3.2.9 Interpretation of the Permian Unconformity operational sequence boundary on line ch90-001b (Seismic amplitude co-rendered with cosine of phase at 80% transparency). Location shown in Figure 3.2.28 (color of the fault is representative of the geological age of the fault).

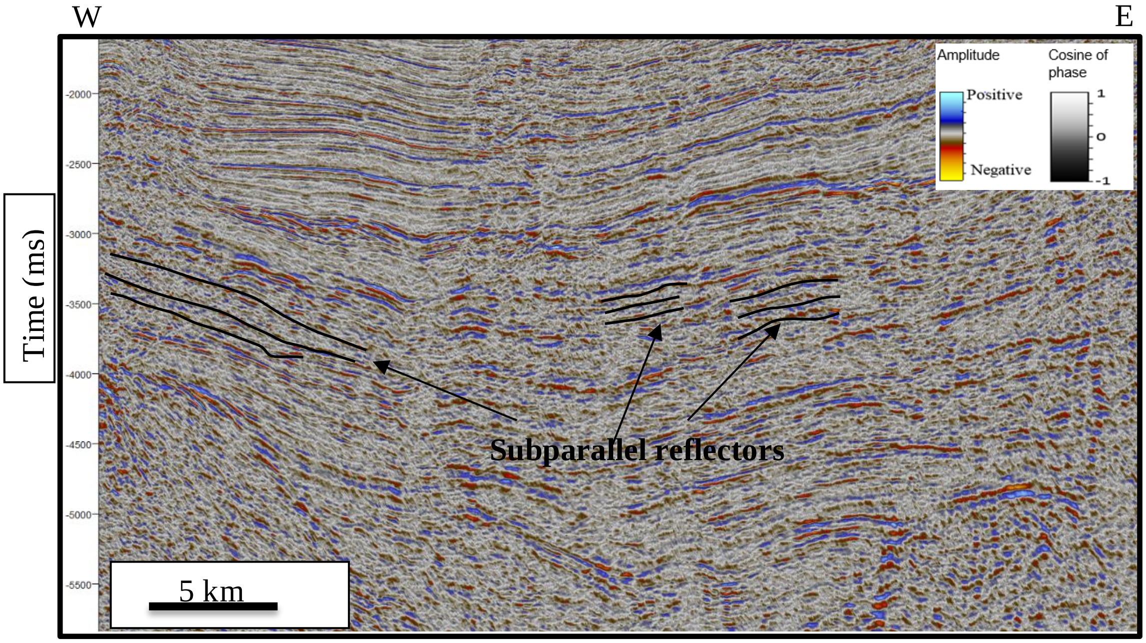

Figure 3.2.10 Subparallel reflectors of the 2nd Lower Ellesmerian on seismic line wcs 6061 (seismic amplitude co-rendered with cosine of phase at 80% transparency). Location shown in Figure 3.2.28.

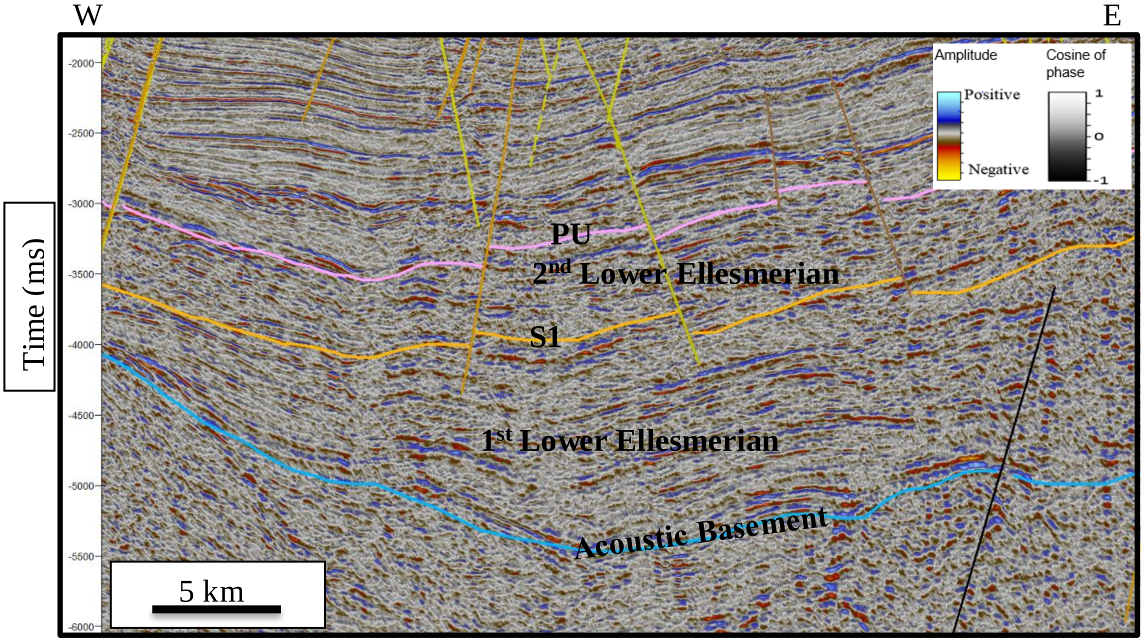

Figure 3.2.11 Interpreted Permian unconformity on line wcs-6061 (seismic amplitude co-rendered with cosine of phase at 80% transparency). Location shown in Figure 3.2.28 (color of the fault is representative of the geological age of the fault).

3.2.4. Brookian Unconformity

This operational sequence boundary is defined by downlapping; it corresponds with the Brookian Unconformity (Thurston, and Theiss 1987).

The seismic facies of the Upper Ellesmerian are subparallel, with reflectors of relatively high amplitude and medium frequency, embedded within reflector packages of low amplitude, reflection free, or chaotic (Figures 3.2.12 and 3.2.13).

Parallel reflections of the Upper Ellesmerian indicate a stable shelf environment for this operational sequence. As for the high amplitude packages embedded within subparallel chaotic dim reflectors, the positive reflection at the interface of the high amplitude package could indicate a shale/sand interface, and a relatively uniform sand package below a shale one (Mitchum et al., 1977).

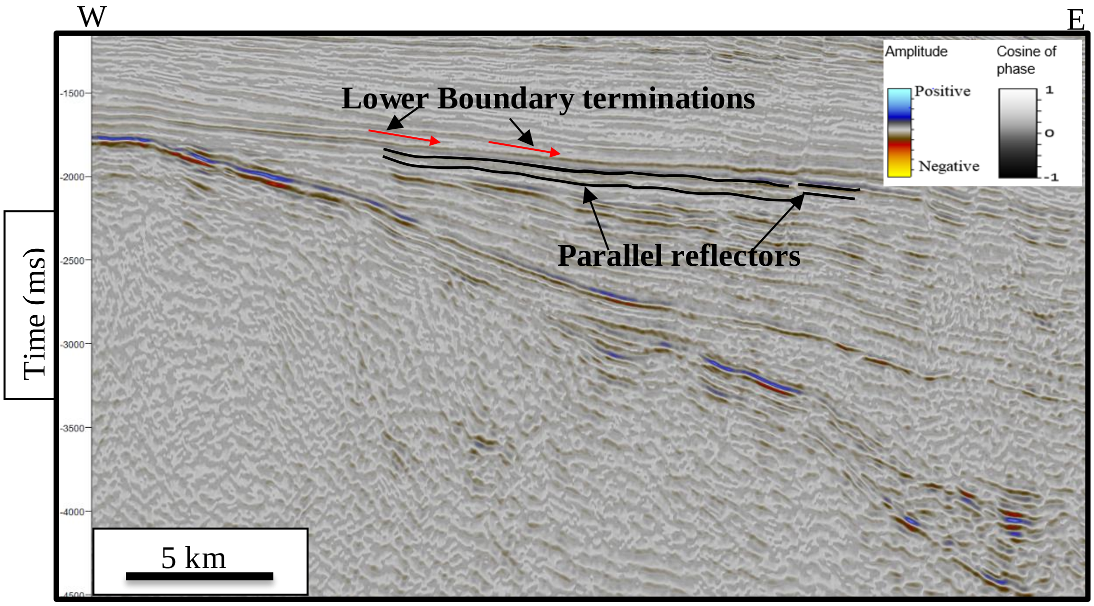

Figure 3.2.12 Lower boundary terminations defining the Brookian Unconformity and parallel reflector geometry of the Upper Ellesmerian on line wcs-6057 (seismic amplitude co-rendered with cosine of phase at 80% transparency). Location shown in Figure 3.2.28.

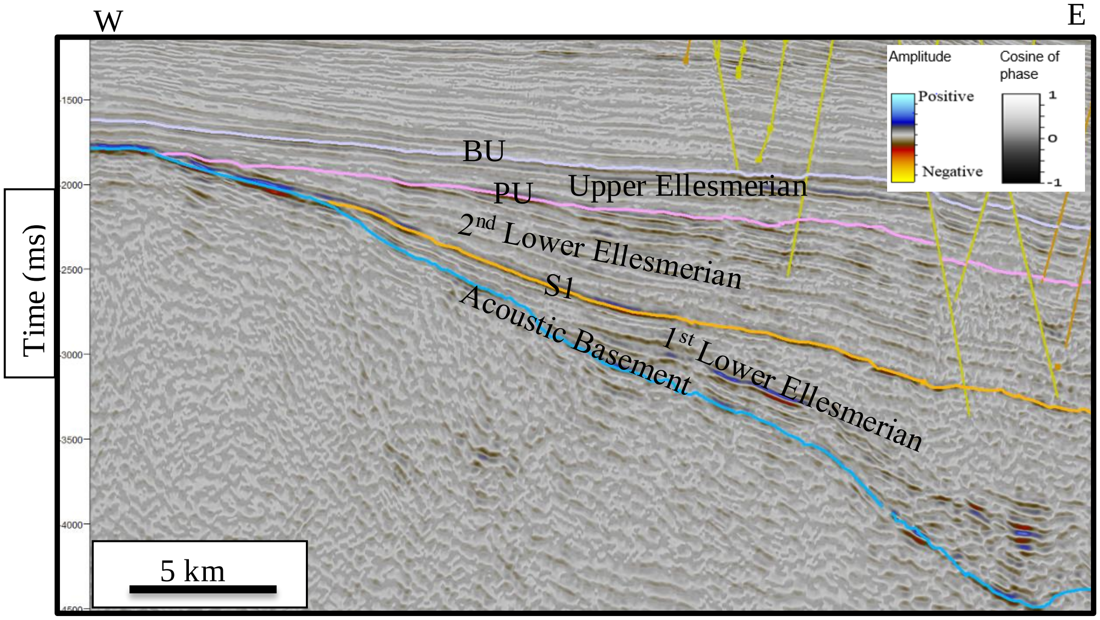

Figure 3.2.13 Interpretation of the Brookian Unconformity on line wcs-6057 (seismic amplitude co-rendered with cosine of phase at 80% transparency). Location shown in Figure 3.2.28 (color of the fault is representative of the geological age of the fault).

3.2.5. MBU

The Middle Brookian Unconformity operational sequence boundary is defined by toplap, particularly in the western part of the basin, above the Chukchi Platform.

Facies of the Lower Brookian are of parallel geometries with a vertical variation of amplitude ranging from medium amplitude to high amplitude, frequencies remain constant reflecting a stable environment of deposition. In the area of the structure, the reflectors of the upper portion of the Lower Brookian are contorted (Figures 3.2.14 and 3.2.15).

Parallel reflectors of the Lower Brookian indicate a relatively low energy environment in a stable shelf, except for the area of the structure where the contorted geometries indicate a possible structural deformation event (Figures 3.2.16 and 3.2.17).

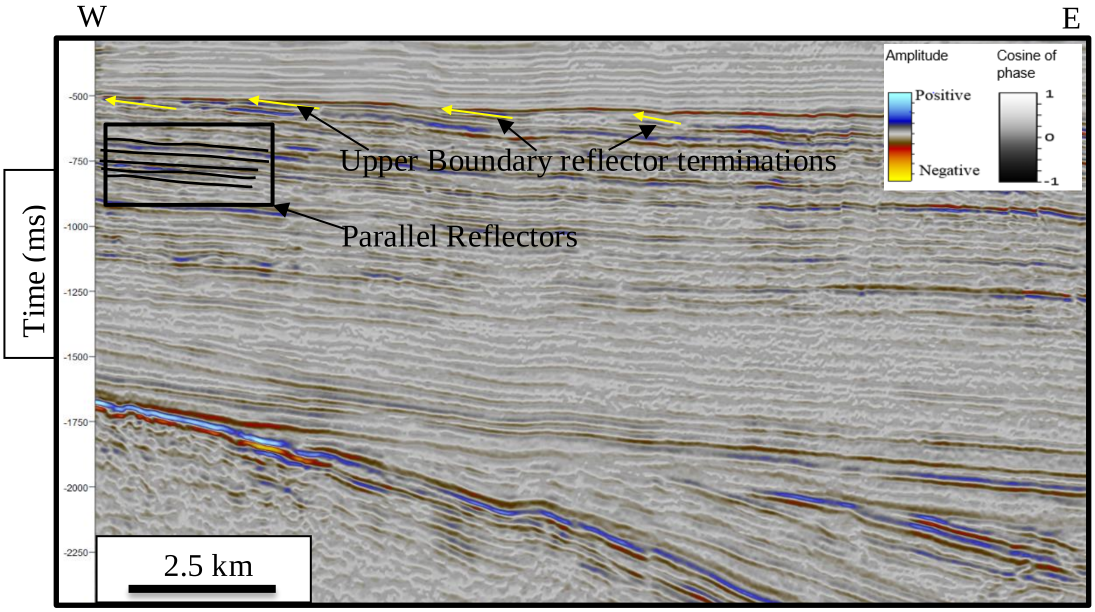

Figure 3.2.14 Upper boundary reflector terminations defining the Middle Brookian Unconformity and parallel reflector geometry of the lower Brookian as observed on line sc86-8406 (seismic amplitude co-rendered with cosine of phase at 80% transparency). Location shown in Figure 3.2.28.

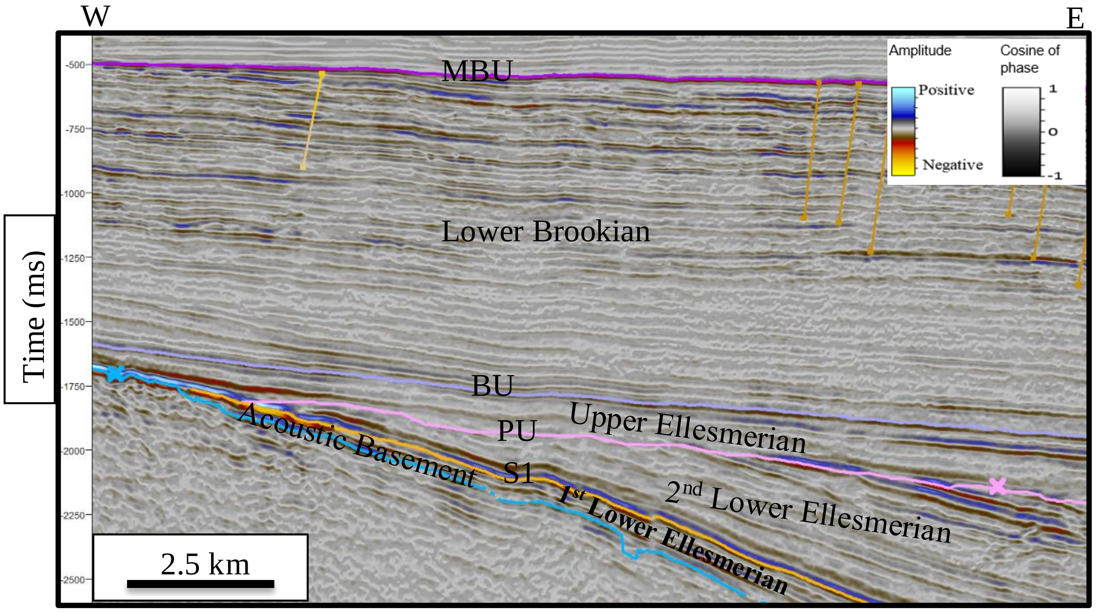

Figure 3.2.15 Interpreted Middle Brookian Unconformity on line sc86-8406 (seismic amplitude co-rendered with cosine of phase at 80% transparency). Location shown in Figure 3.2.28 (color of the fault is representative of the geological age of the fault).

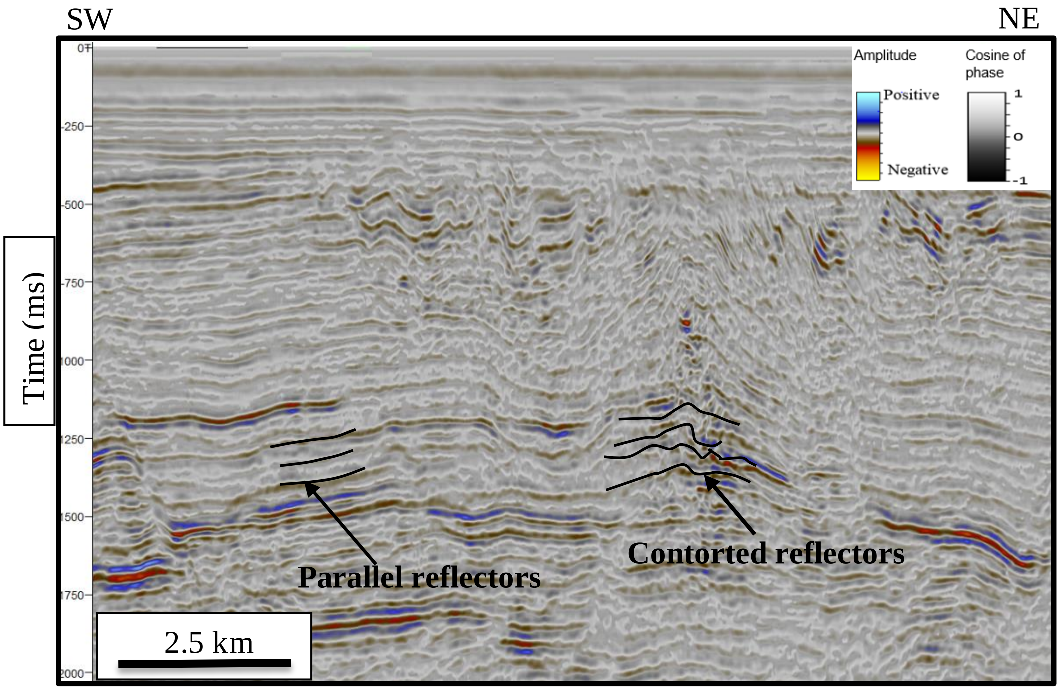

Figure 3.2.17 Lower Brookian reflector geometries: parallel reflectors at the area of the structure, and contorted reflectors in the area of the structure, line ch83-104a (seismic amplitude co-rendered with cosine of phase at 80% transparency). Location shown in Figure 3.2.28.

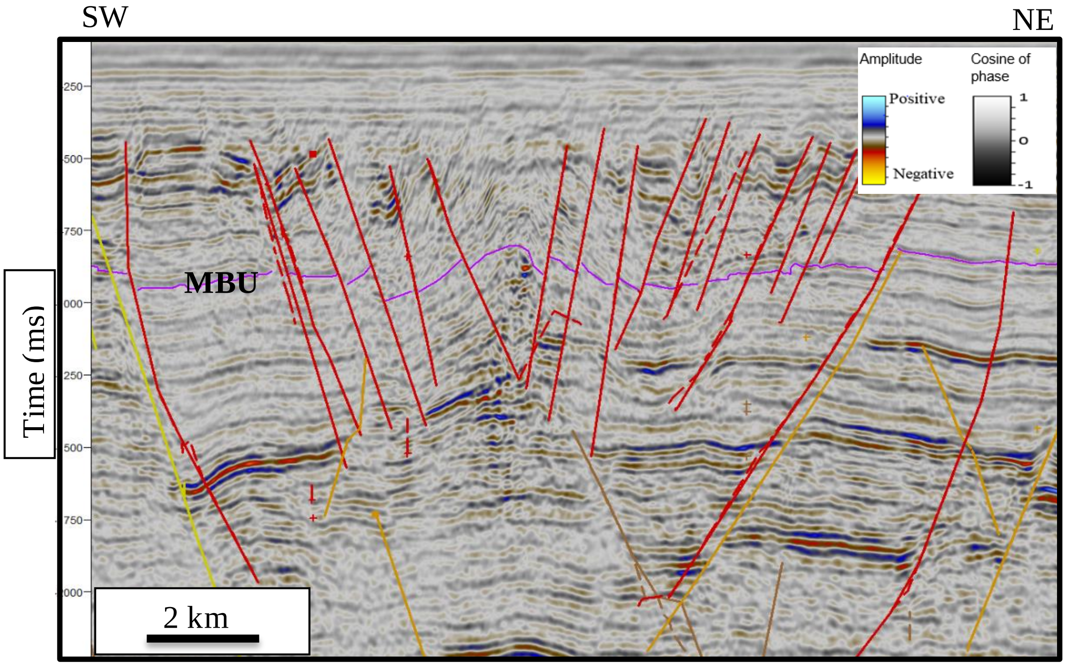

Figure 3.2.16 Middle Brookian Unconformity interpretation on line ch83-104a (seismic amplitude co-rendered with cosine of phase at 80%. Location shown in Figure 3.2.28 (color of the fault is representative of the geological age of the fault).

3.2.6. S6

This operational sequence boundary is defined by truncations (Figure 3.2.18) (Figure 3.2.19) at several lines, wcs-6057 among them. A well top does not define it though. This operational sequence boundary might only represent an unconformity of local occurrence.

The geometries of the Upper Brookian are commonly parallel, with low amplitude and medium frequencies. There is an abrupt lateral change of the facies in the area of the structure: low frequency reflectors above chaotic reflector packages in the faulted blocks, and chaotic dim reflector facies in the center of the structure (Figures 3.2.20 and 3.2.21).

Parallel geometries in the area outside of the northcentral subbasin indicate a low energy, stable shelf environment. In the northcentral subbasin, geometries are also parallel.

The abrupt change of facies from medium frequency parallel reflectors to low frequency parallel fault blocks, and subsequently to chaotic dim reflectors in the center of the structure (Figures 3.2.20 and 3.2.21) indicate a variable relatively high-energy setting, or highly deformed strata (Mitchum et al.,1977).

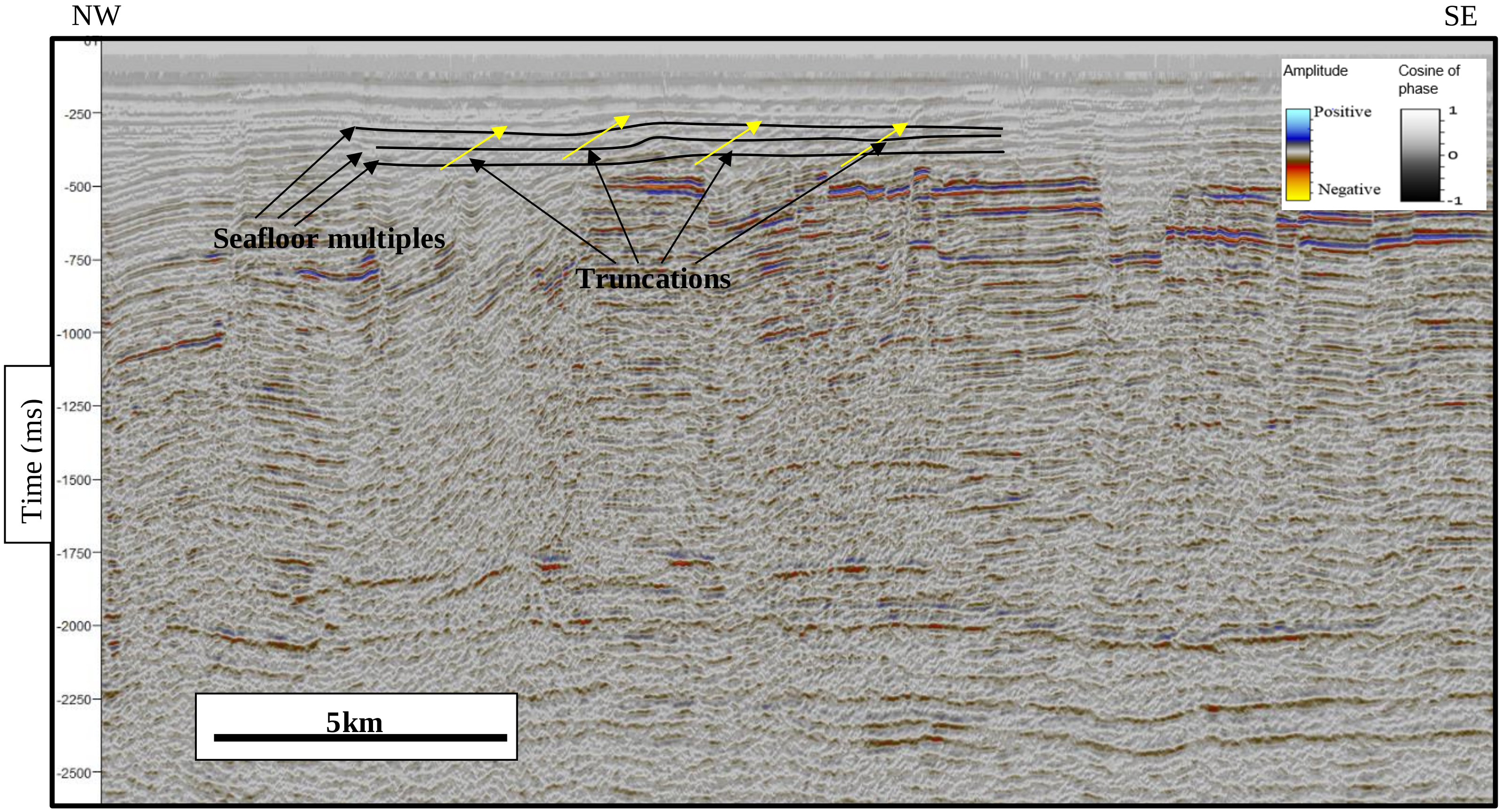

Figure 3.2.18 Truncations defining the S6 operational sequence boundary, and multiples at the area of the truncations as observed on line ch85_39a (seismic amplitude co-rendered with cosine of phase at 80% transparency). Location shown in Figure 3.2.28.

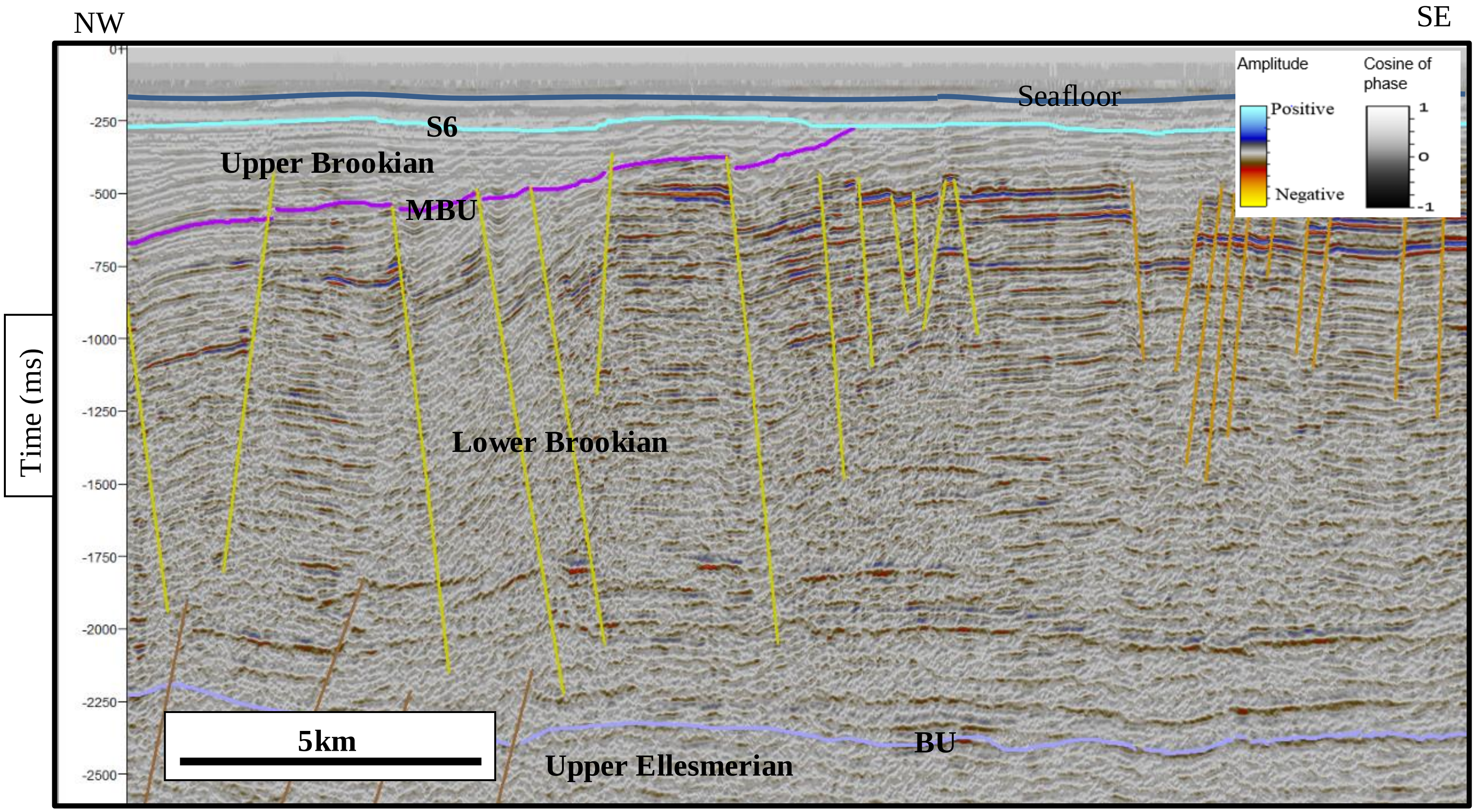

Figure 3.2.19 Interpretation of S6 on line ch85_39a (seismic amplitude co-rendered with cosine of phase at 80% transparency). Location shown in Figure 3.2.28 (color of the fault is representative of the geological age of the fault).

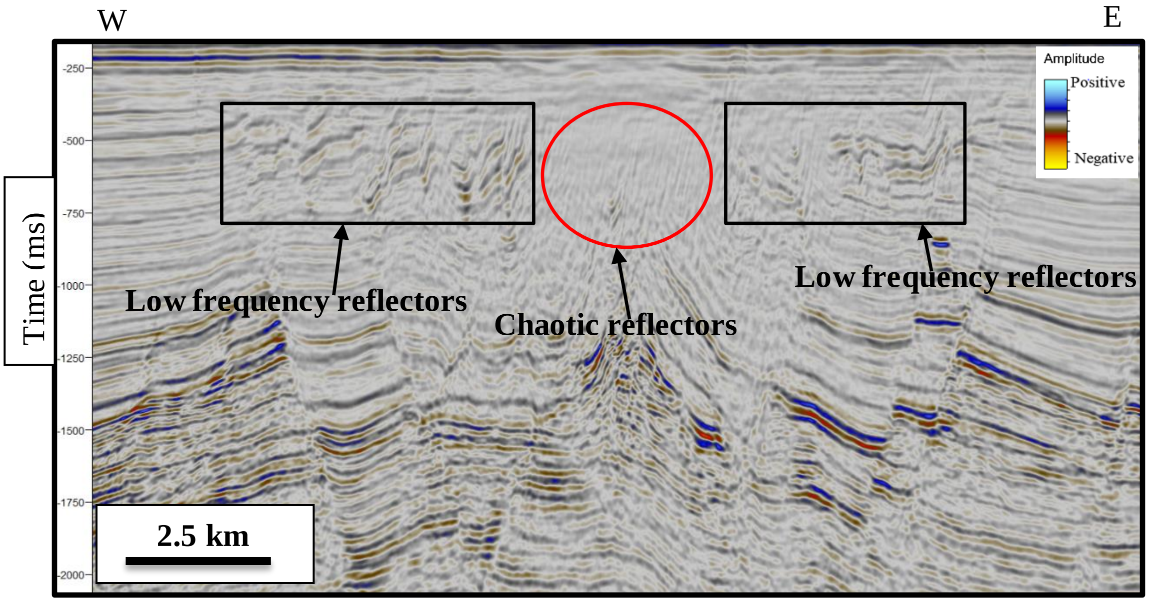

Figure 3.2.20 Chaotic and low frequency reflectors of the Upper Brookian on line wcs-6059. Location shown in Figure 3.2.28.

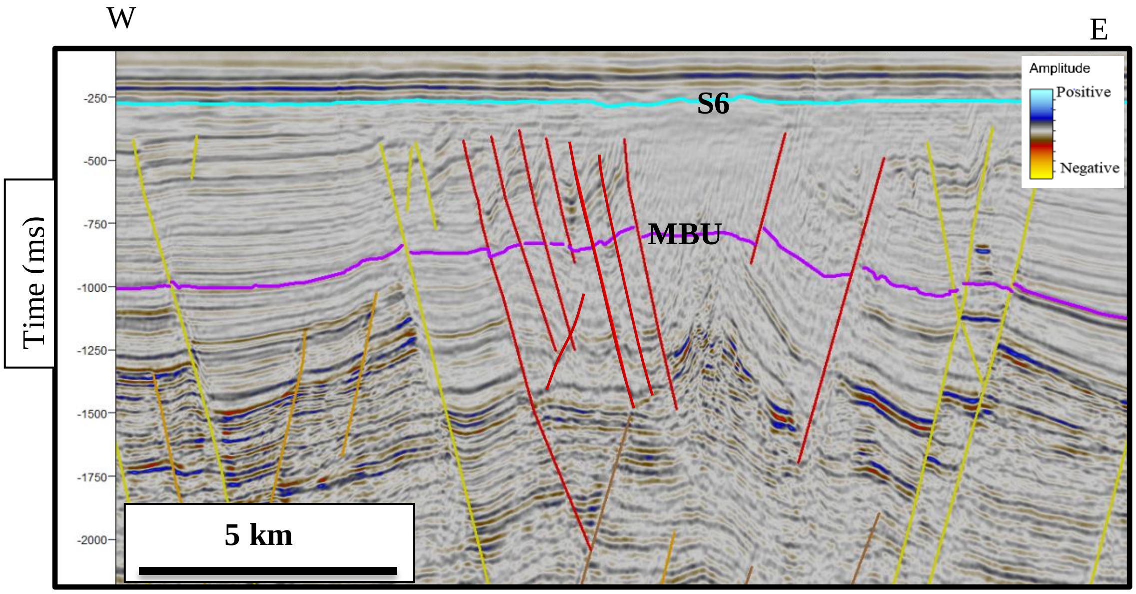

Figure 3.2.21 Interpreted seismic horizons MBU and S6 at the area of the structure on line wcs-6059. Location shown in Figure 3.2.28 (color of the fault is representative of the geological age of the fault).

3.2.7. Seismic facies distribution

Once the seismic facies were interpreted, the seismic facies were mapped by interpolation between the seismic lines. One map for each interpreted seismic operational sequence was made.

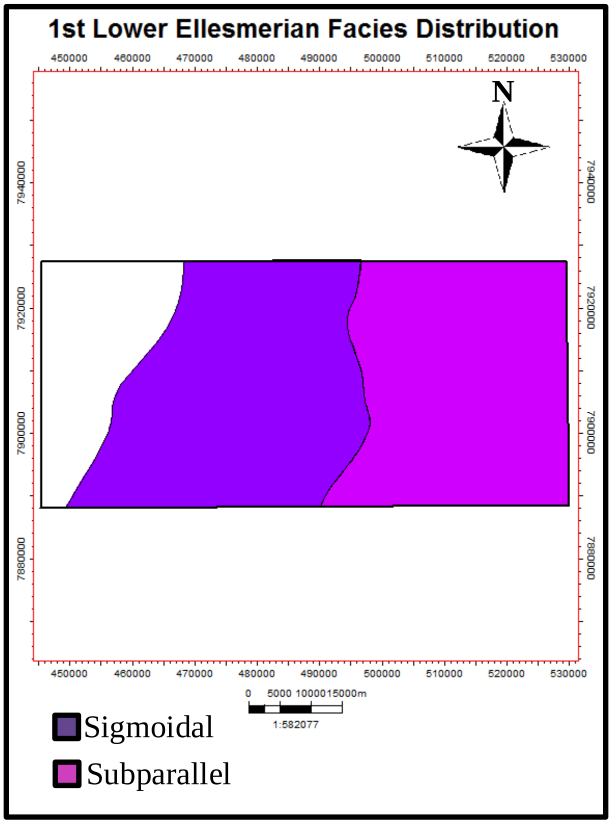

Figure 3.2.22 1st Lower Ellesmerian facies distribution. Location shown in Figure 3.2.27.

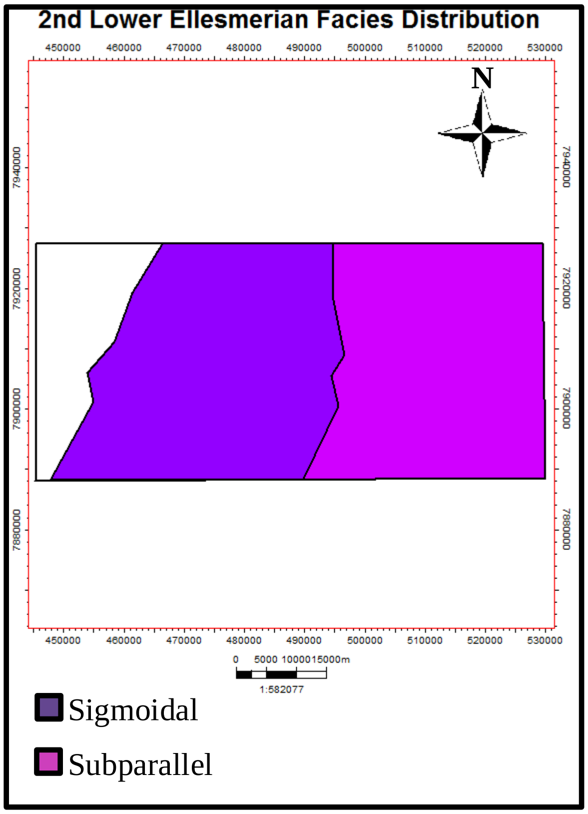

Figure 3.2.24 2nd Lower Ellesmerian facies distribution. Location shown in Figure 3.2.27.

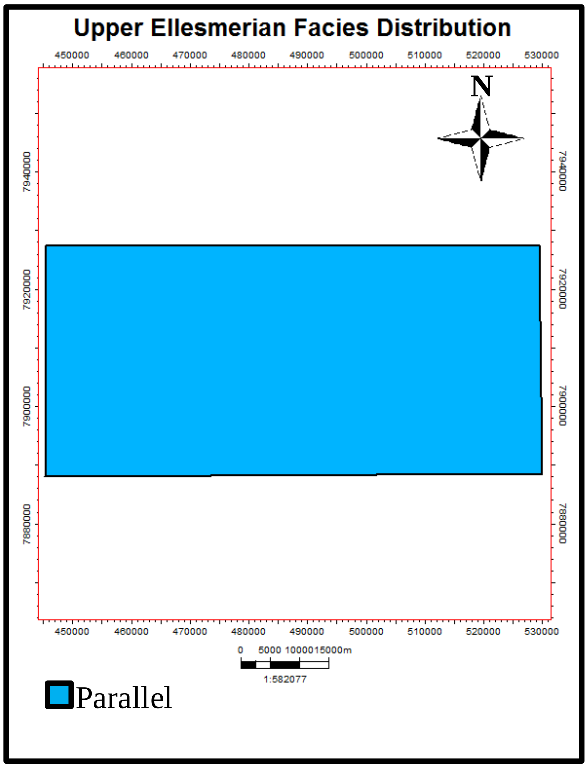

Figure 3.2.23 Upper Ellesmerian Facies Distribution. Location shown in Figure 3.2.27.

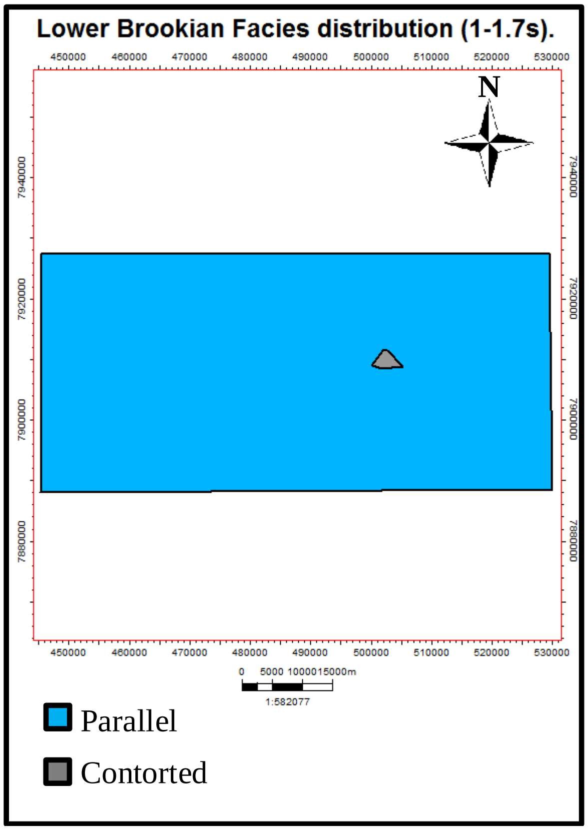

Figure 3.2.26 Lower Brookian facies distribution at a depth range between 1 and 1.7 seconds. Location shown in Figure 3.2.27

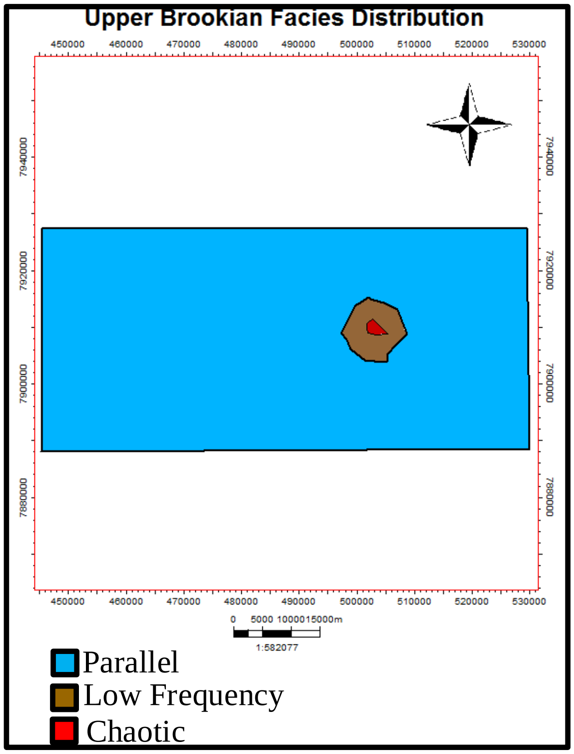

Figure 3.2.25 Upper Brookian facies distribution. Location shown in Figure 3.2.27.

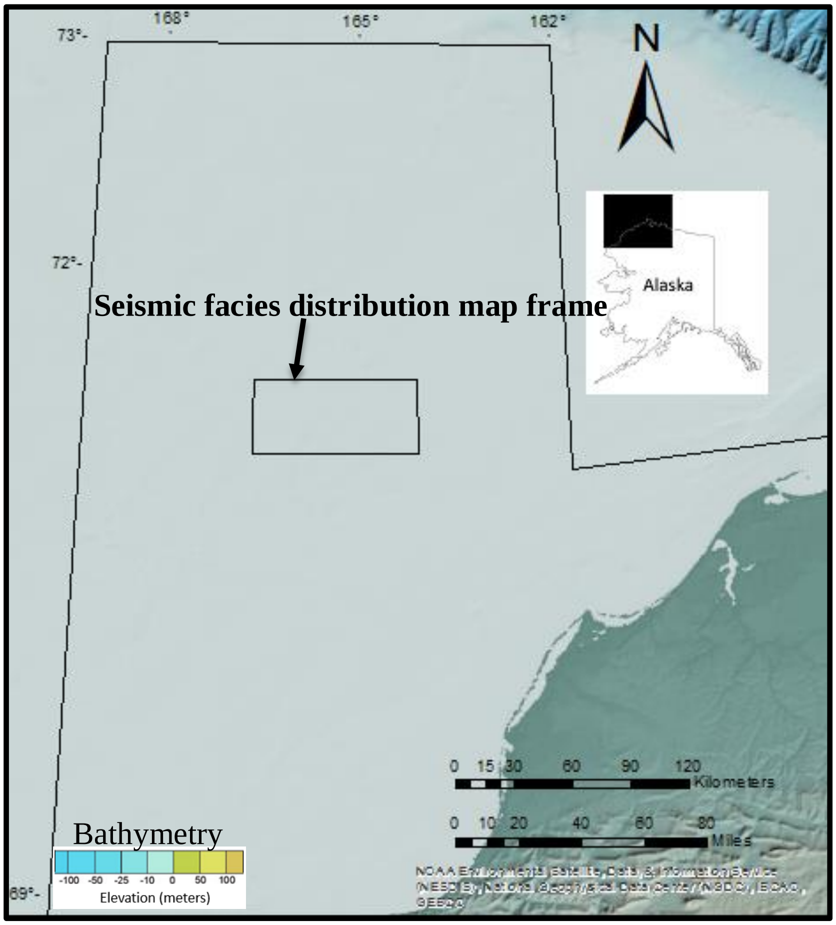

Figure 3.2.27 Ubication of the seismic facies distribution map on the Chukchi Sea. Topographic and bathymetric basemap from Jakobsson et. al, 2012.

3.2.8. Discussion

Except from the area of the structure, the depositional environment has been interpreted to be of low to medium energy, affected by several episodes of rifting and thermal subsidence. The first episode of rapid subsidence is indicated by the 1st Lower Ellesmerian and 2nd Lower Ellesmerian facies; the progradation of the sigmoidal clinoforms of these operational sequences from west to east indicate a shallow environment with depositional direction W-E. Afterwards, the parallel facies from the Upper Ellesmerian up to the Upper Brookian indicate a stable shelf environment of deposition, the Upper Ellesmerian indicates a W-E deposition direction, but the Lower and Upper Brookian display a change in deposition direction from W-E to N-S.

The abrupt change of facies in the area of the structure, and the limited distribution of the facies associated with the structure, i.e. from parallel reflector to low frequency fault blocks, chaotic, and contorted facies (Figures 3.2.20 and 3.2.21); indicate that the most possible reason for these abrupt changes in seismic facies is structural deformation in the area of the structure.

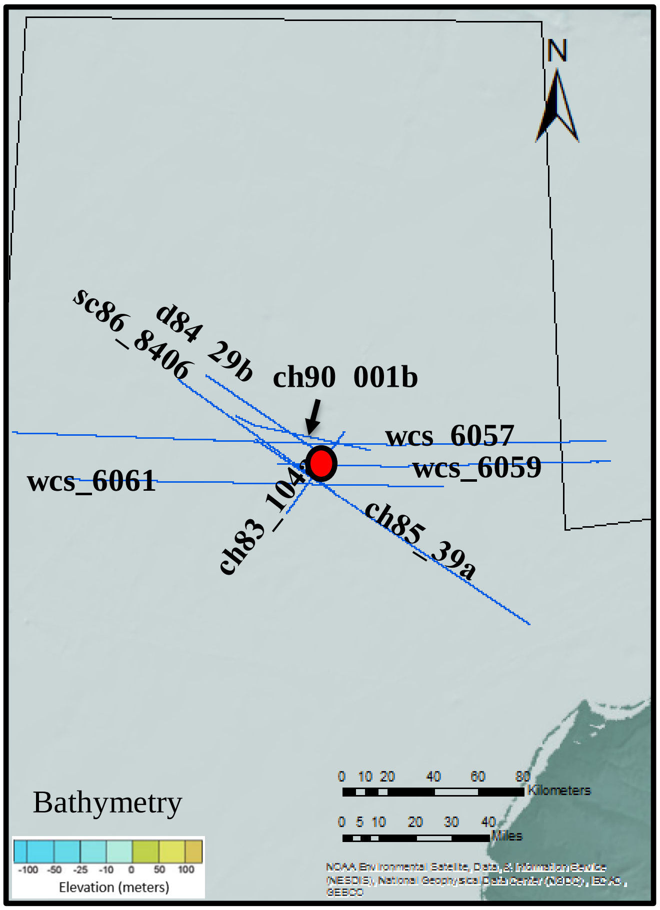

NOAA Environmental Satellite, Data, & Information Service (NESDIS), National Geophysical Data Center (NGDC), IBCAO, GEBCO

Figure 3.2.28 Location of seismic lines described in this section relative to the area of the structure (red). Topographic and bathymetric basemap from Jakobsson et. al, 2012.

3.3. Seismic stratigraphic well tie

Part of the procedure is to tie the seismic stratigraphic interpretations to the well control. Except for the Acoustic basement and S1, the rest of the interpreted operational sequence boundaries were at stratigraphic levels penetrated by the well Crackerjack #1-OCS-Y-1320.

Derived from the checkshot logs: TWT, MD, and Interval velocity, a depth to time conversion curve was calculated and the depths of the logs and of well tops were converted to two way travel time to perform the seismic stratigraphic well tie on line ch90-001b.

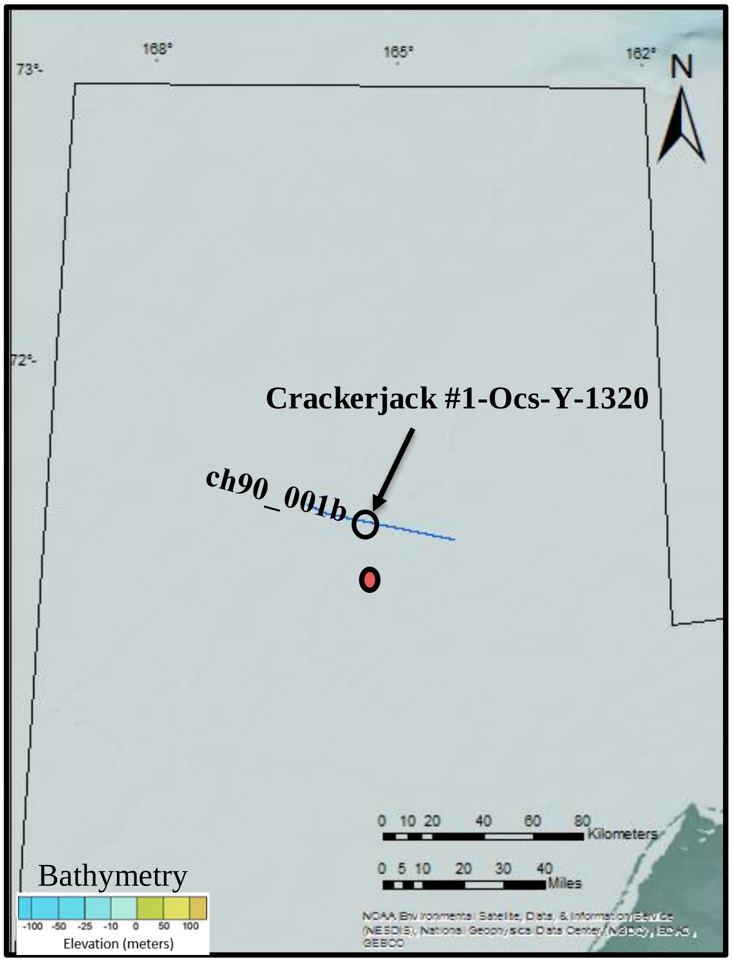

Figure 3.3.1 Location of line ch90_001b, well Crackerjack #1-OCS-Y-1320 (black circle), and area of the structure (red). Topographic and bathymetric basemap from Jakobsson et. al, 2012.

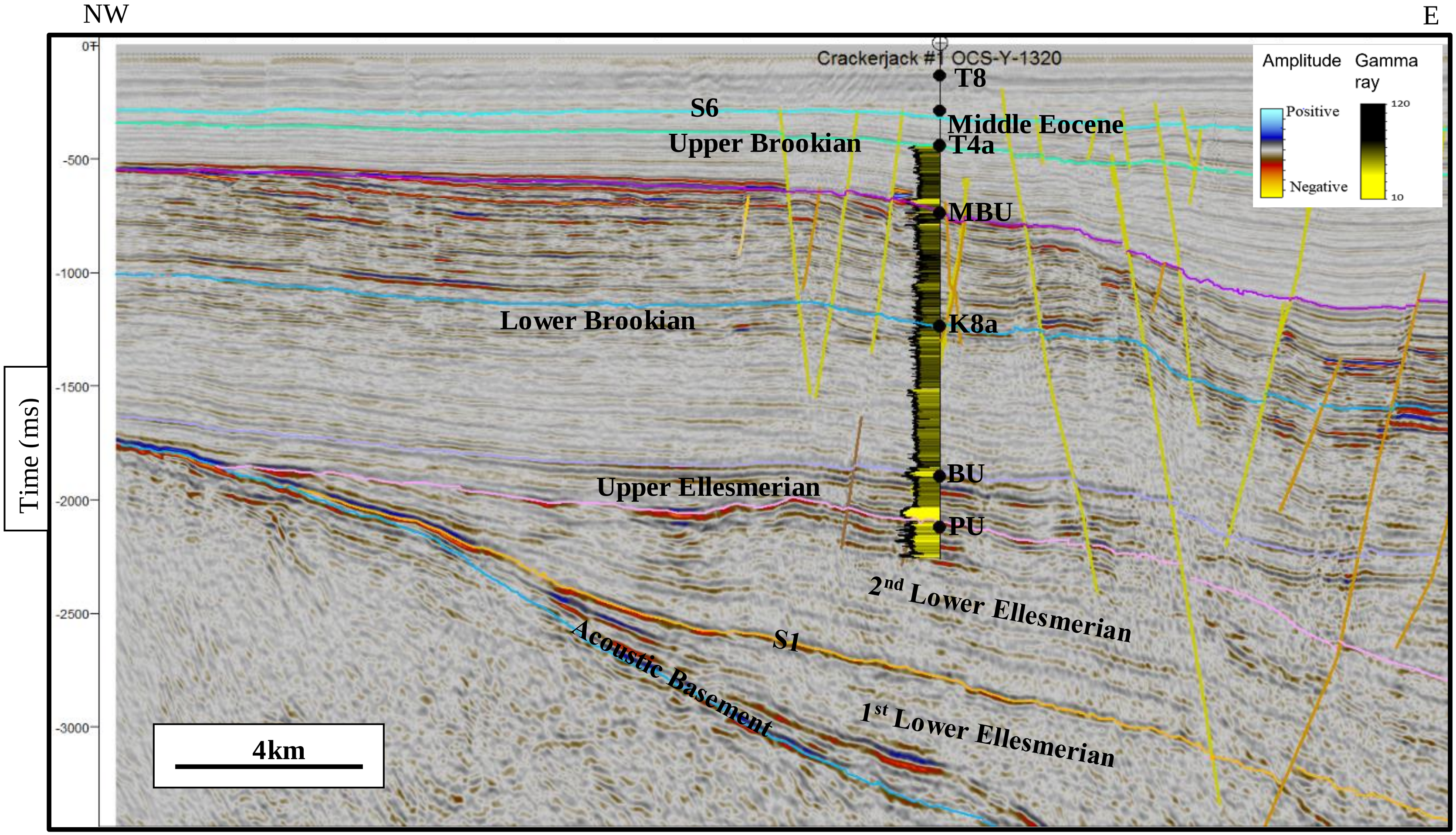

Figure 3.3.2 Well control on line ch90-001b, total gamma ray log and well tops (black circles). Location shown in Figure 3.3.1.

3.3.1. Permian Unconformity

The picked reflector does not exactly match the well top and the trough in the reflector at the well top.

3.3.2. Brookian Unconformity

Unconformity defined by downlapping (in the area of the Chukchi Platform). The picked horizon matches the reflector that consistently corresponds with both the total gamma ray log and the well top.

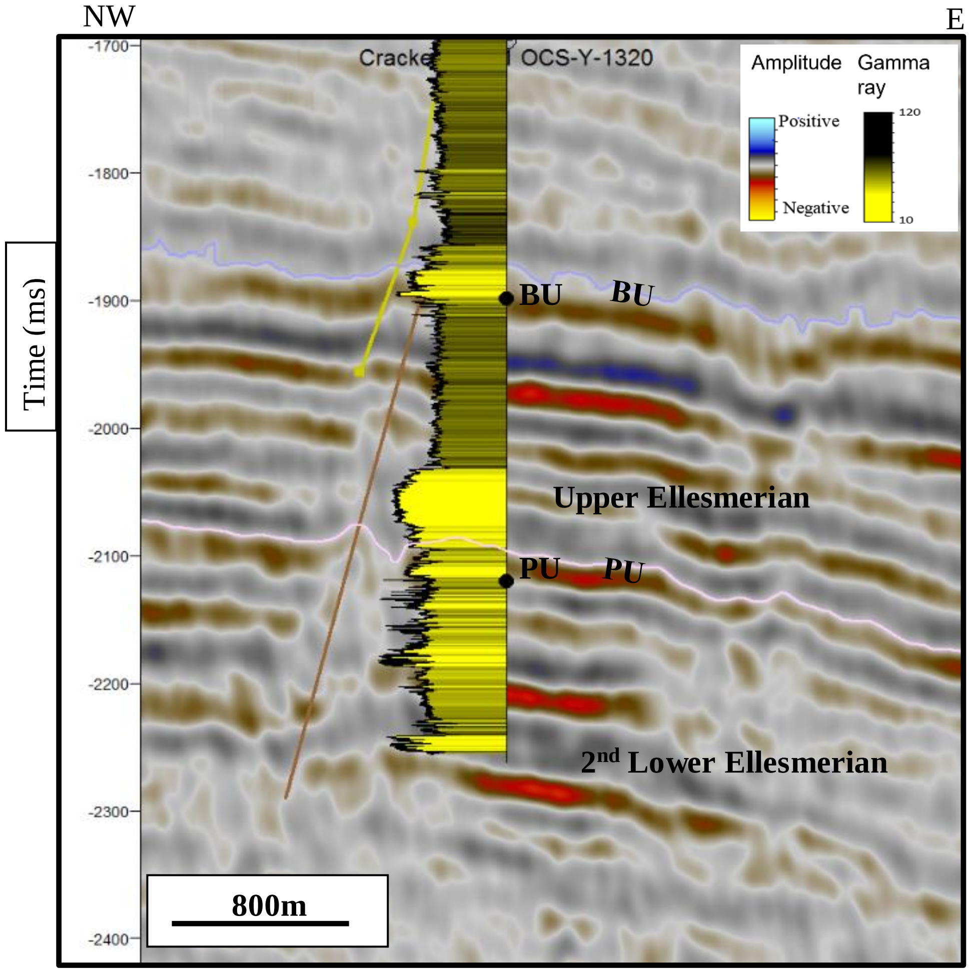

Figure 3.3.3 Close up on well tops, total gamma ray log, and picked reflectors for the Permian Unconformity and the Brookian unconformity on line ch90-001b. Location shown in Figure 3.3.1.

3.3.3. Middle Brookian Unconformity

Defined by toplap in the seismic reflections. The picked horizon ties with a reflector in the seismic that matches the well top and the total gamma ray log.

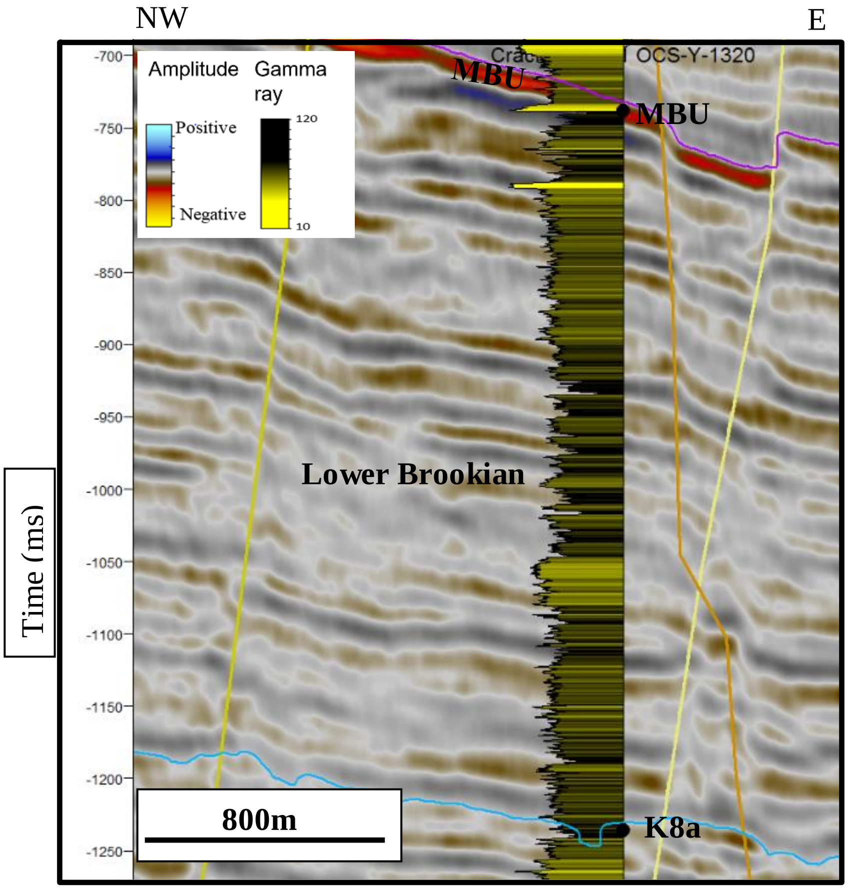

Figure 3.3.4 Middle Brookian Unconformity well top and picked horizon, and K8a well top and picked K8a seismic horizon on line ch90-001b. Location shown in Figure 3.3.1.

3.3.4. S6

Defined by truncations in the Northcentral subbasin. There are no corresponding well tops or gamma ray signature change that ties this reflector with the well, thus this is interpreted as an unconformity of local occurrence, but nonetheless it could provide a timing constrain for the structure and its associated features. The stratigraphic position of this reflector between the early and middle Eocene tops dates it as a Middle Eocene surface.

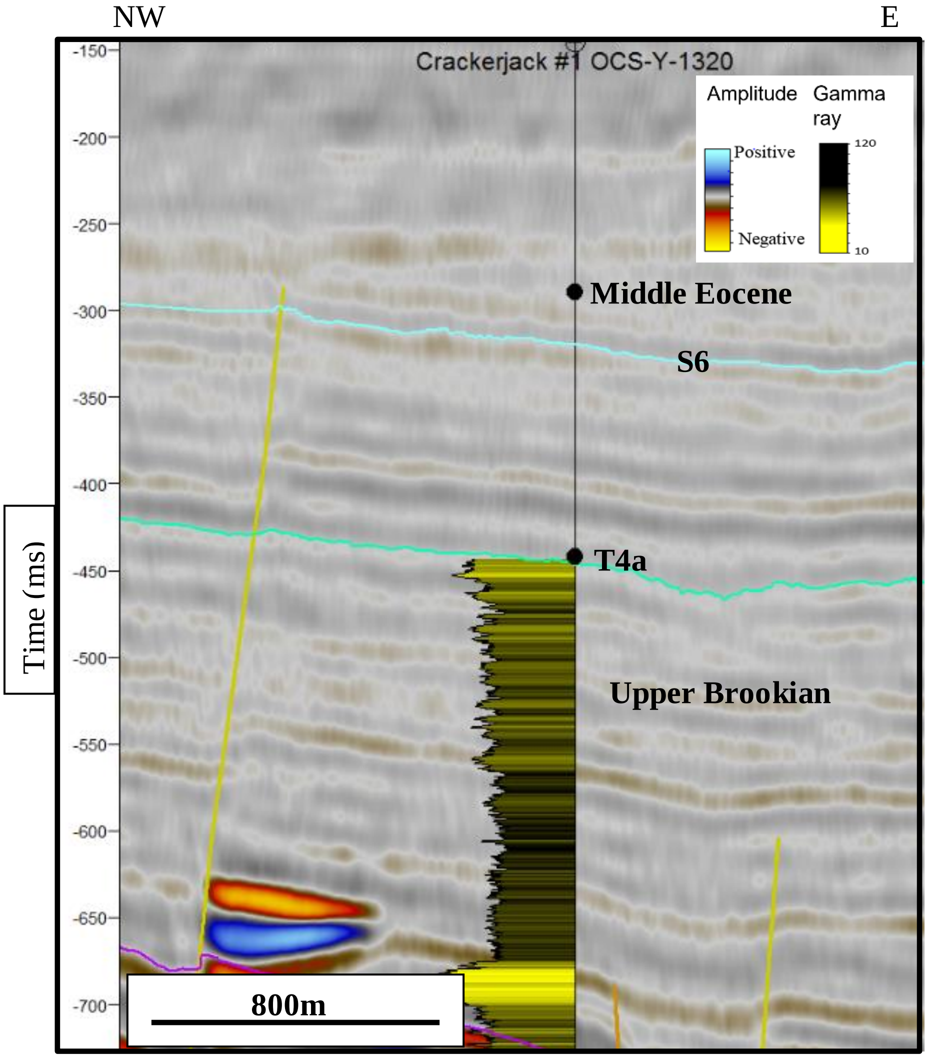

Figure 3.3.5 T4a Well top and seismic horizon, S6 operational sequence boundary, and Middle Eocene well top, line ch90-001b. Location Shown in Figure 3.3.1.

3.3.5. Discussion

The fact that well log resolution is higher than seismic resolution of ~30 cm, could explain why there are interpreted operational sequence boundaries that do not exactly match well tops; seismic resolution is between 10-30 m depending on the acquisition and processing parameters.

3.4. Well to seismic tie (synthetic seismogram)

In order to validate the horizon interpretation with the geology observed in the well, and asses the correlation of the geology in the well and the seismic, a synthetic seismogram was calculated utilizing a bulk density log and a sonic log from the well Crackerjack #1 OCS-Y-1320. The resulting synthetic acoustic impedance was convolved with a deterministic wavelet extracted from the seismic and the calculated impedance time series utilizing the method for wavelet extraction described in Walden and White (1998).

This wavelet extraction method utilizes the principles of covariance-based coherence and it takes into account the fact that there is noise present in both the well log data and in the seismic data (Walden and White, 1998).

3.4.1. Brookian Unconformity

It can be observed that the trough associated with the Brookian Unconformity matches the well top and the synthetic seismogram generated from the well.

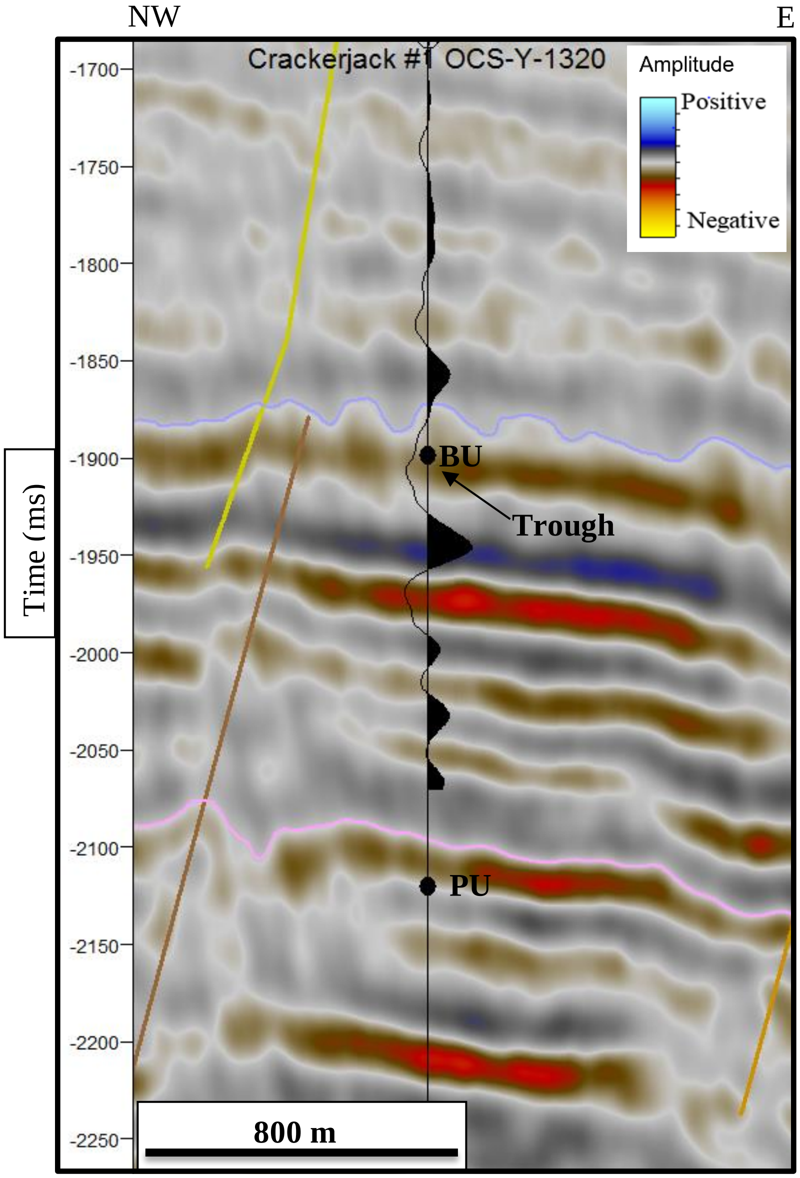

Figure 3.4.1 Seismic to well tie of the BU at the well Crackerjack #1 OCS-Y-1320. Location Shown in Figure 3.3.1.

3.4.2. Middle Brookian Unconformity

Similarly to the Brookian unconformity, a trough in the generated synthetic seismogram matches the reflector and the well top associated with the Middle Brookian Unconformity.

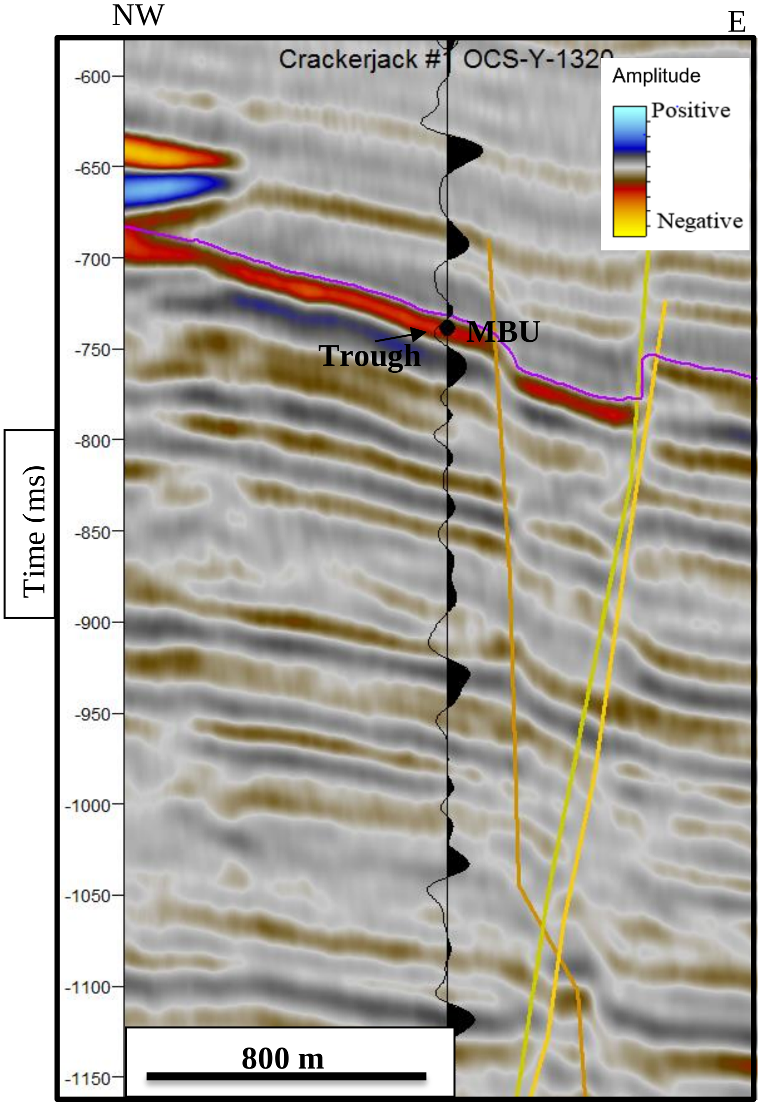

Figure 3.4.2 Well to seismic tie of the MBU at well Crackerjack #1-OCS-Y-1320. Location Shown in Figure 3.3.1.

3.4.3. Discussion

The well to seismic tie of the operational sequence boundaries in this section shows a clear correlation between the geology observed in the well and the geophysical signature of those horizons. Nonetheless, the coverage of the sonic log data and of the bulk density, data is limited throughout the well, and only the BU and the MBU horizons were correlated.

3.5.Fault Mechanical Stratigraphy

Fault mechanical stratigraphy analysis is utilized to determine the approximate geological ages of the faults. This analysis was performed in the same 26 lines that were used for seismic stratigraphic interpretation.

The procedure to assign approximate geological ages to the faults was to examine which operational sequence boundaries and seismic horizons, picked from correlating reflectors with well tops, were cut vertically by the faults. From this analysis, five families of faults were recognized; line d85-o-m2 (Figure 3.4.6) is an example where there are no faults associated to the CCDS. For line d84-29b (Figure 3.4.7) all five families of faults can be observed.

3.5.1. Early Permian

These faults are colored in black, they cut through the Franklinian basement of late Devonian age, and in some cases the lower Ellesmerian operational sequence boundary *S1*.

This tectonic event is probably related to the late Devonian-early Permian rifting, which created the Hanna Trough.

3.5.2. Lower Cretaceous

The second oldest set of faults cut through S1 (Lower Ellesmerian), PU (Permian unconformity), and K4 (Lower Cretaceous Unconformity). This family of faults are of Cretaceous age, and are colored in brown in the interpreted seismic lines.

3.5.3. Upper Cretaceous

The third set of faults stops before the Middle Brookian Unconformity, in lines wcs-6057, wcs-6059, and wcs-6063, one fault of this group appears to be a reactivated basement fault. These faults are colored in orange

3.5.4. Early to Middle Eocene.

These faults go through Tertiary seismic horizons, they are associated with extensional and transtentional structures, i.e. horsts, grabens, half grabens, and flower structures.

3.5.5. Middle Eocene (CCDS related Faults).

In the lines where the structure can be seen, these faults are restricted to a narrow range of geological time. The faults associated with the structure only cut through the middle Eocene seismic horizon T4a (extrapolated from the well).

3.5.6. Intersections of faults at time surfaces.

After all the faults families were interpreted a closer inspection upon the faults related to the structure was performed, with the purpose to delimitate the area of the structure and the vertical range of the faults i.e. time. Maps of the intersections of the fault planes with time surfaces at 1500ms (Figure 3.4.1), 1000ms (Figure 3.4.2), 500ms (Figure 3.4.3), and 250ms (Figure 3.4.4) were made. Three groups of faults were identified within that time range: Tertiary, Middle Eocene (structure), and Upper Cretaceous

3.5.7. Discussion

The criteria used to date the faults was the same for each family; the faults were grouped if the top of the faults was in certain vertical range or if the fault was crossing a determined time significant seismic horizon. The fault mechanical stratigraphy of the

CCDS is distinctive, these faults do not display a variability in time, and they are only constrained to a determined seismic horizon only (T4a). Contrasting with the other families of faults that are variable in time; typical of geological processes due to its chronological nature i.e. they require several million years to happen. Because of that and the apparent instantaneous FMS of the faults related to the structure, the CCDS faults where given its particular division, even though they are also in the Tertiary, as the rest of the faults crossing the MBU seismic horizon.

Figure 3.5.1 Upper Cretaceous, Middle Eocene (structure), and Early to Middle Eocene faults intersection at 1500ms. Location shown in Figure 3.5.5.

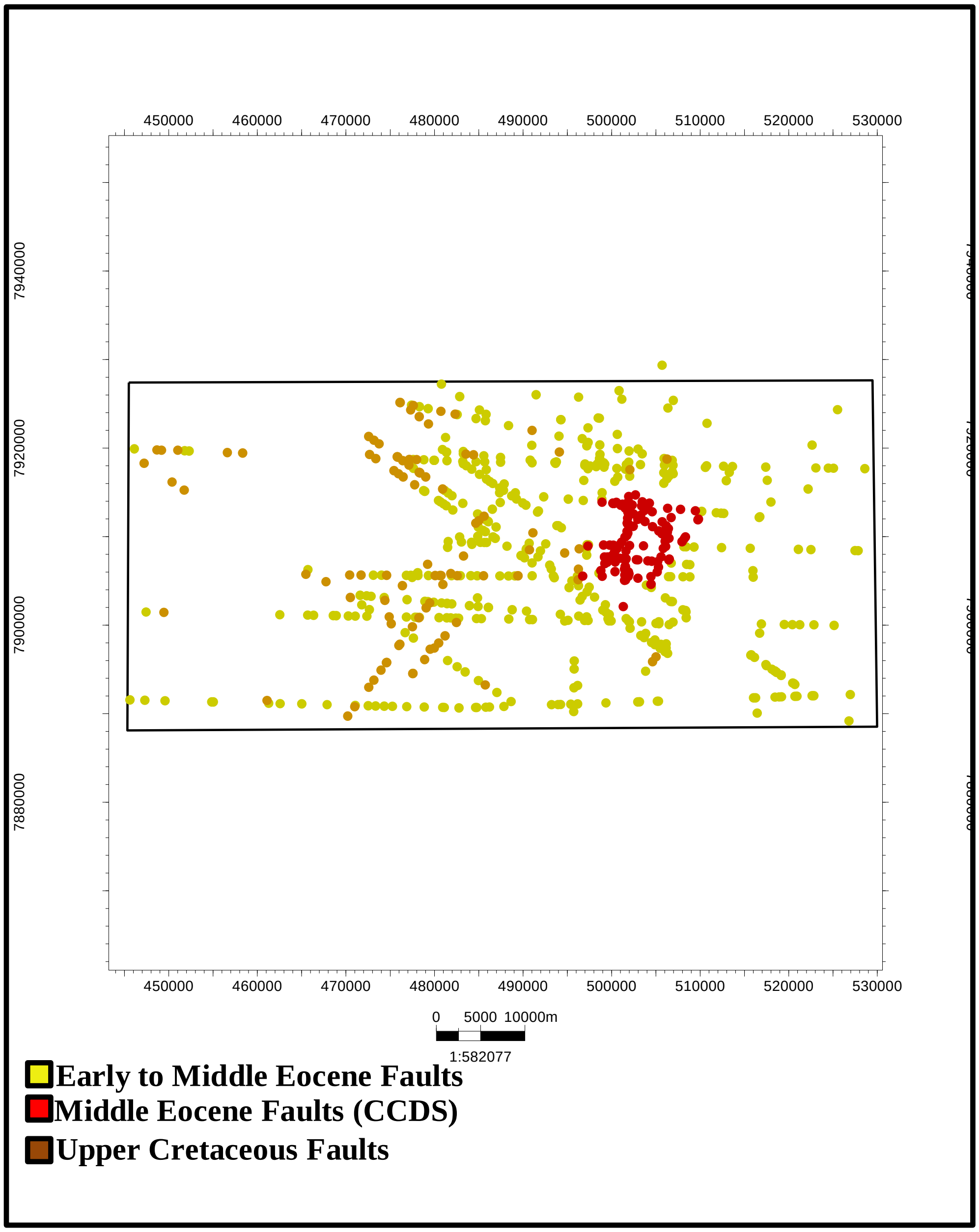

Figure 3.53.5.2 Upper Cretaceous, Middle Eocene (structure), and Early to Middle Eocene faults intersection at 1000ms. Location shown in Figure 3.5.5.

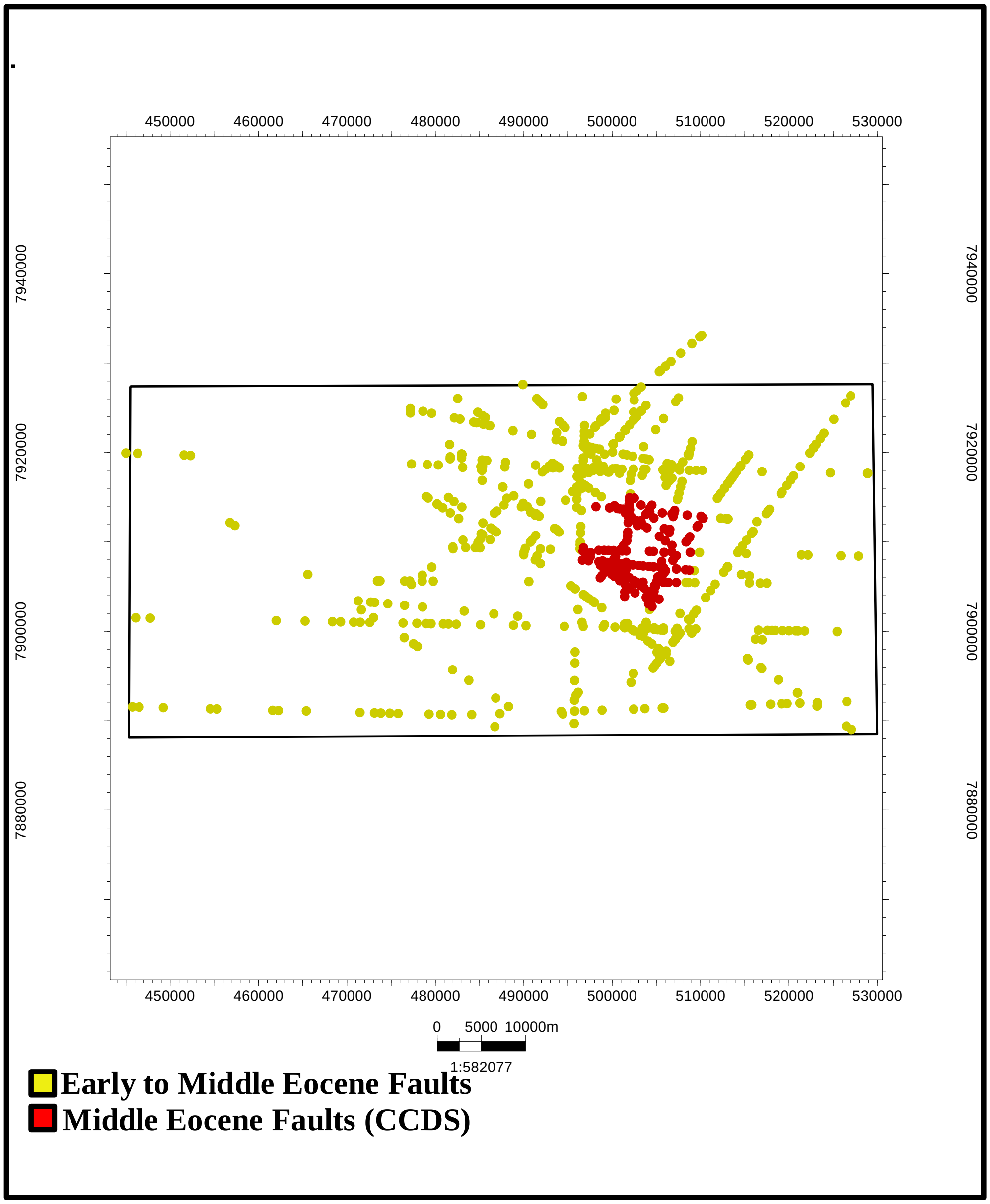

Figure 3.53.5.3 Early to Middle Eocene and Middle Eocene faults intersections at 500ms. Location shown in Figure 3.5.5.

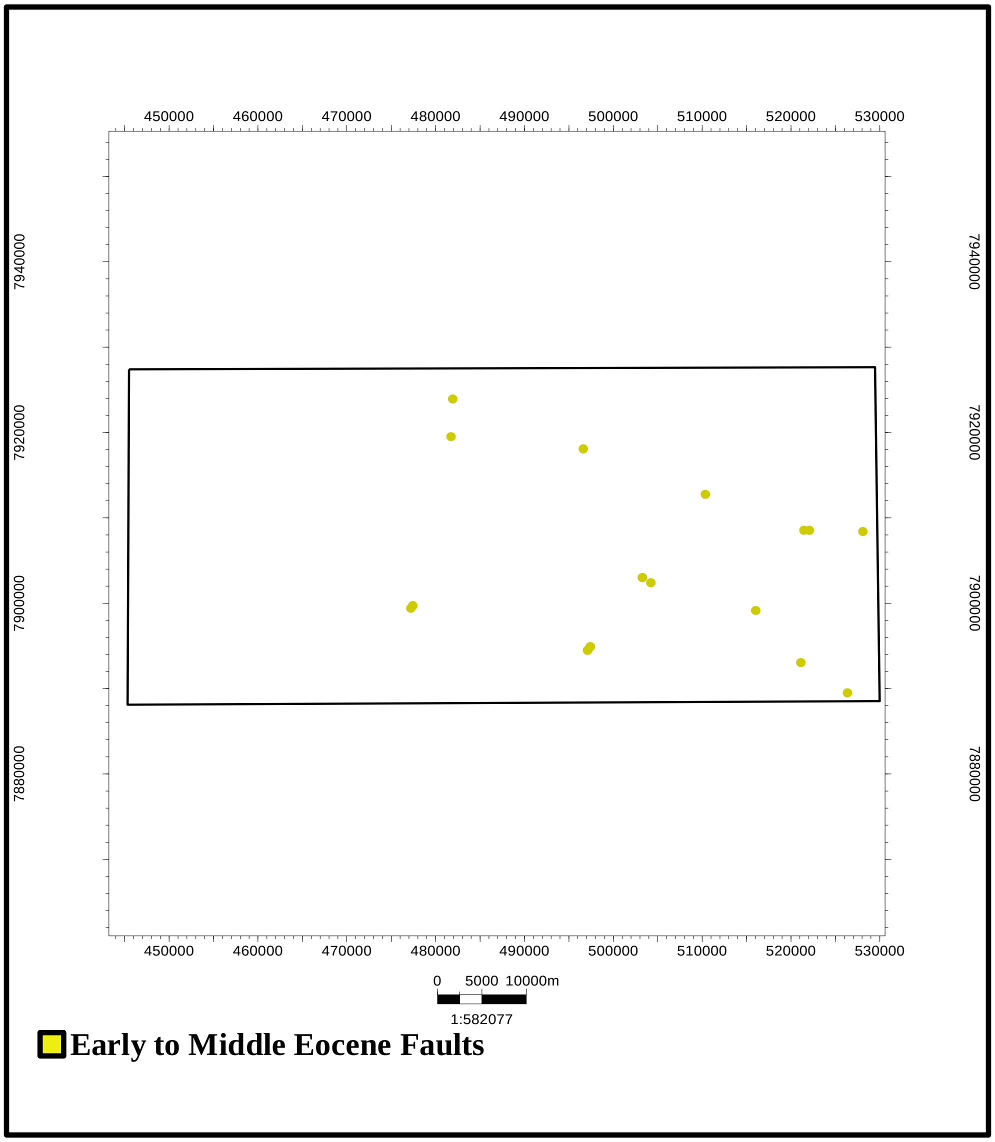

Figure 3.55.4 Early to Middle Eocene faults intersection at 250ms. Location shown in Figure 3.5.5.

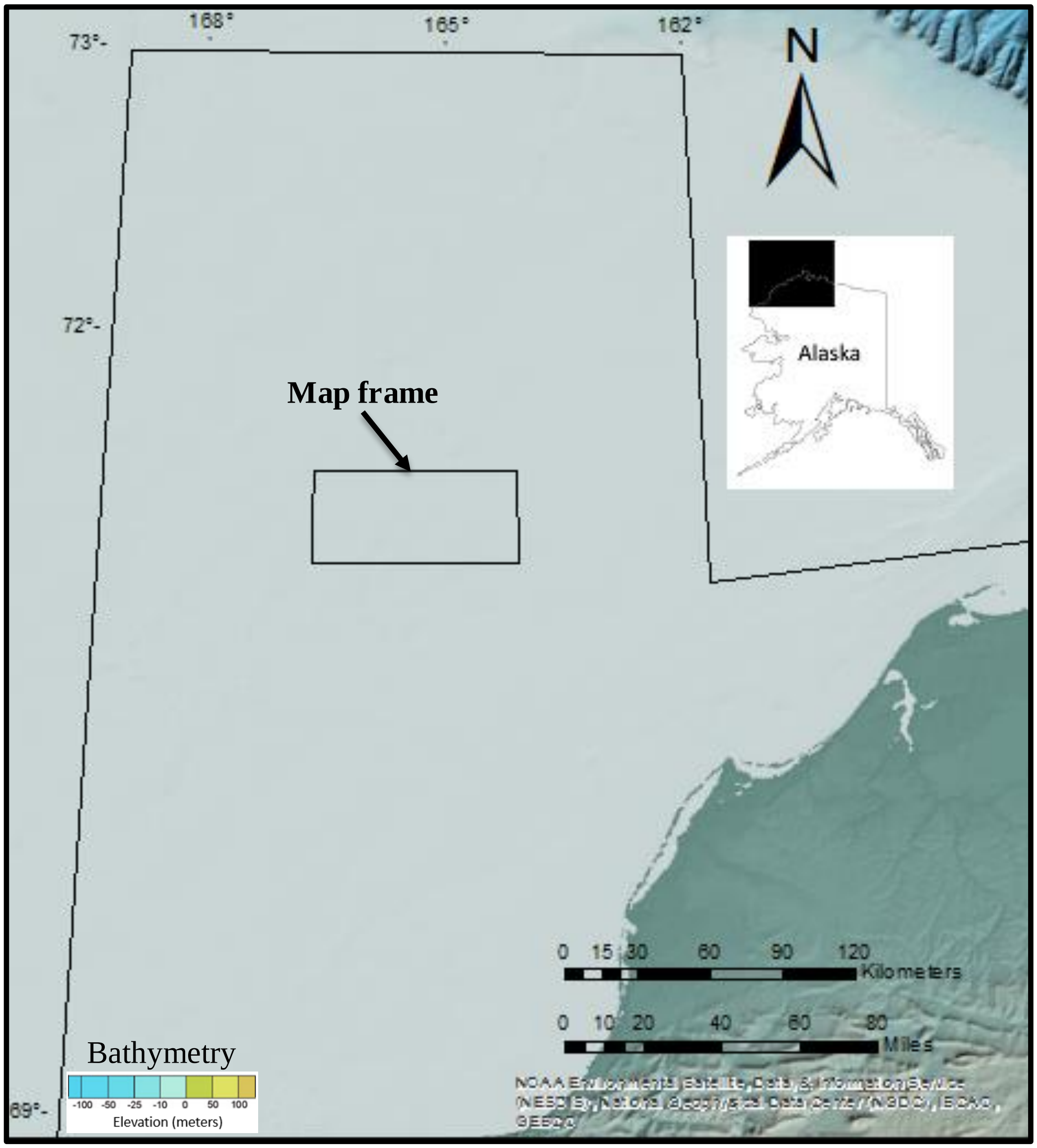

NOAA Environmental Satellite, Data, & Information Service (NESDIS), National Geophysical Data Center (NGDC), IBCAO, GEBCO

Figure 3.55.5 Location of the map frame in the Chukchi Sea planning area. Topographic and bathymetric basemap from Jakobsson et. al, 2012.

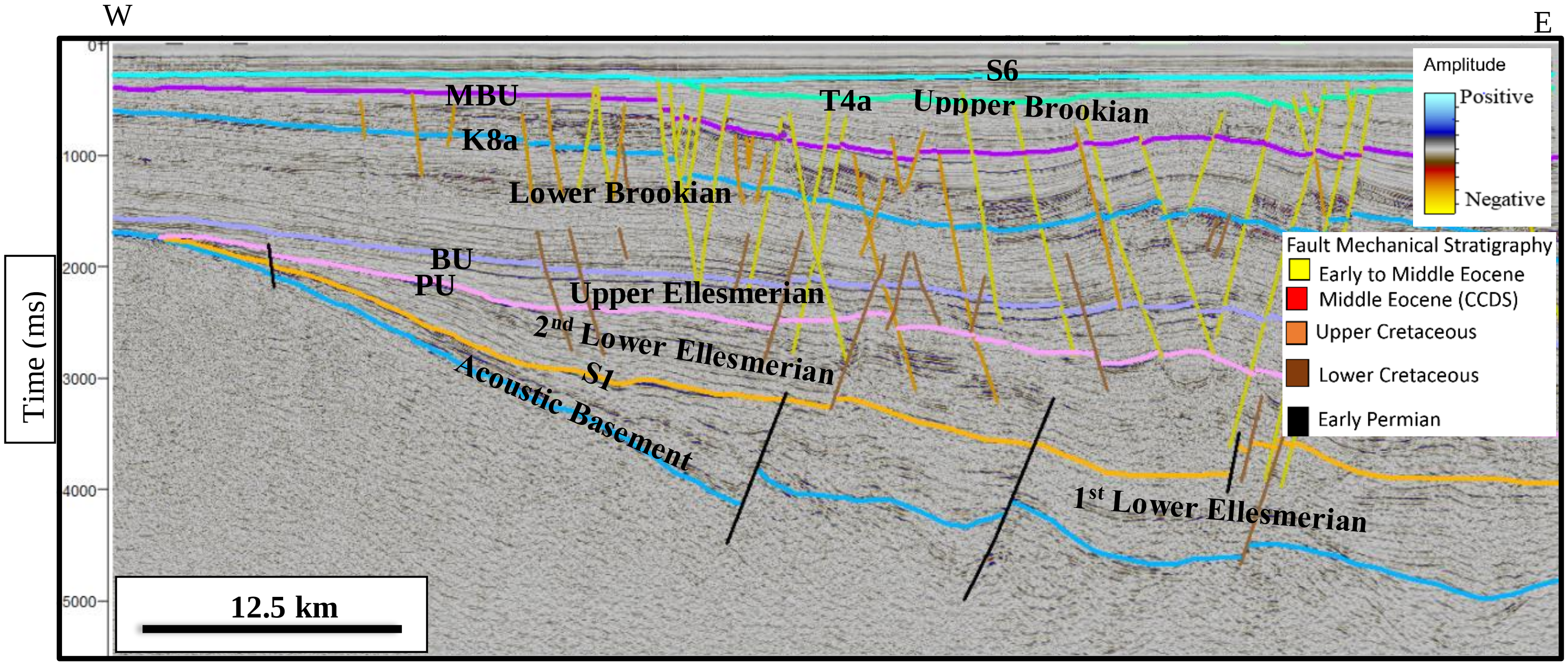

Figure 3.5.6 Example of fault mechanical stratigraphy on line d85_o_m2. Location shown in Figure 3.5.8.

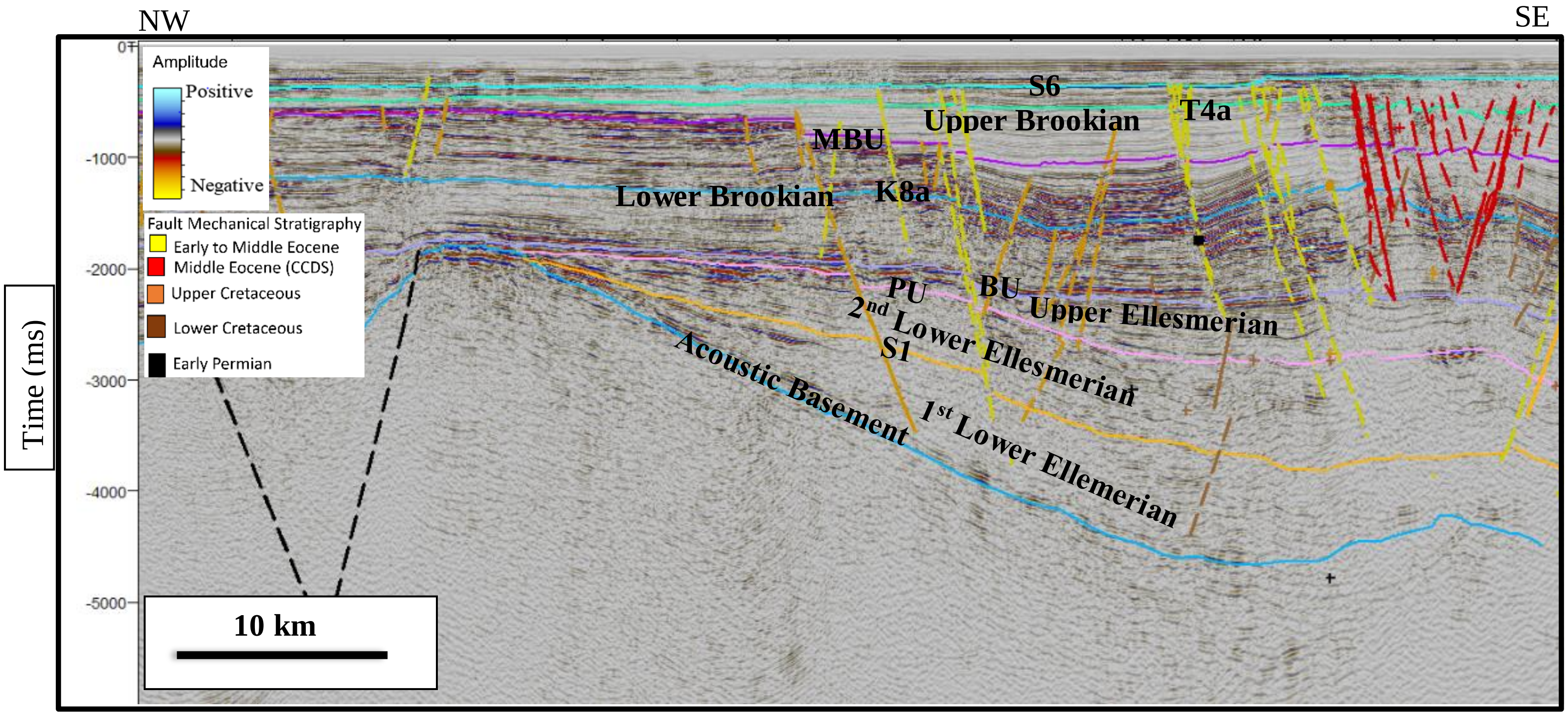

Figure 3.5.7 Example of fault mechanical stratigraphy on line d84-29b. Location shown in Figure 3.5.8.

Table 3.1 Fault mechanical stratigraphy color-coding.

Age	Color
Middle Eocene (diffuse fault traces)	Red
Early to Middle Eocene (distinct fault traces)	Yellow
Upper Cretaceous	Light Brown
Lower Cretaceous	Brown
Early Permian	Black

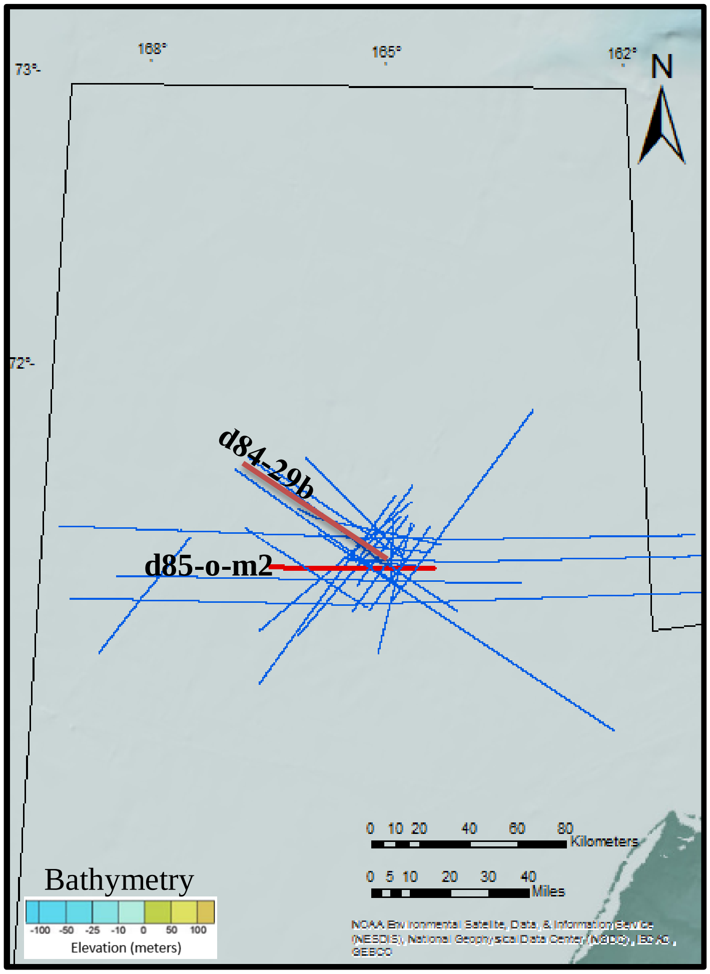

Figure 3.5.8 Location of line d85_o_m2, and d84-29b (red). Topographic and bathymetric basemap from Jakobsson et al. 2012

4. Geological Hypotheses

Qualitative interpretation was the approach to solve the geological problem studied in this thesis; the interpretation techniques utilized, well data, and geological knowledge of the area constrained and narrowed down the number of solutions to several geological models that could explain the aspect of the structure in seismic data.

These geological models along with their correspondences and discrepancies with the data are explained in this chapter. The models were chosen by its possible occurrence in the tectonic settings of the area, the typical seismic signature of the models, or a combination of both.

4.1.Reactive diapirism

Reactive diapirs occur in regional thin-skinned extension structural regimes where the extension rates are slow. A source layer of a fluid material (e.g. evaporites or mobile shale) fills the mass void created by the extension, and as the fault blocks become progressively smaller, the diapirs support them at higher structural levels, thus forming diapiric structures (Vendeville and Jackson, 1992).

Derived from the fault mechanical stratigraphy analysis, it can be said that an extensional structural regime with relatively low extension rates is present in the Chukchi Basin. Another mechanism that could favor the formation of a reactive diapir is basin forming transtensional regimes; from the literature (Thurston and Theiss, 1987), and from direct observations in the data (i.e. the negative flower structure in the Chukchi Platform) it is known that transtensional structural regimes are present in the area.

Thurston and Lothamer (1991), interpreted evaporitic diapirs in an isolated area on the Chukchi Platform, northwest of the structure, these structures can also be observed on the seismic lines provided by the BOEM (Figure 4.1.2). However, the diapirs interpreted on the Chukchi Platform are active diapirs, indicated particularly by the outward and upward rotation of the flaps flanking these diapirs (Figure 4.1.3) (Schultz et al., 1993). The structure is located in the Northcentral subbasin, where no author has reported evaporites through neither seismic interpretation nor well data, and the seismic facies of the homoclinal structure itself (i.e. contorted reflectors below MBU) do not indicate evaporitic lithologies.

The fault mechanical stratigraphy of the faults related to the structure constrains them to a limited range of geological time, middle Eocene indicated by the T4a seismic horizon, in contrast with the theory and examples of reactive diapirism where the faults get younger towards the center of the structure (Vendeville and Jackson 1992).

The model of an evaporite reactive diapir does not fit the observations coherently; evaporites are commonly reflection free or chaotic, with high amplitude reflectors on the top (Sheriff and Geldart, 1995), as for our structure the reflection free/chaotic facies are above the anticlinal feature of the structure that resembles a diapir. A reactive shale diapir model does not fit the observations either; even though the operational sequence below the MBU is defined by clastics; an approximation of the depth of the structure through the checkshot data indicates a depth range of the structure from 1500-2000m, lower than 3000m, depth at which shale can become mobilized.

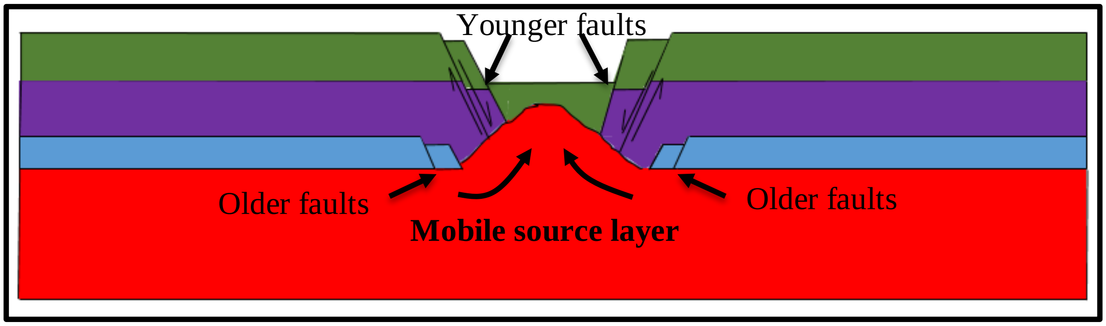

Figure 4.1.1 Model of a reactive diapir, modified after et al., 2016. Sigma 3 stresses are horizontal and perpendicular to fault planes.

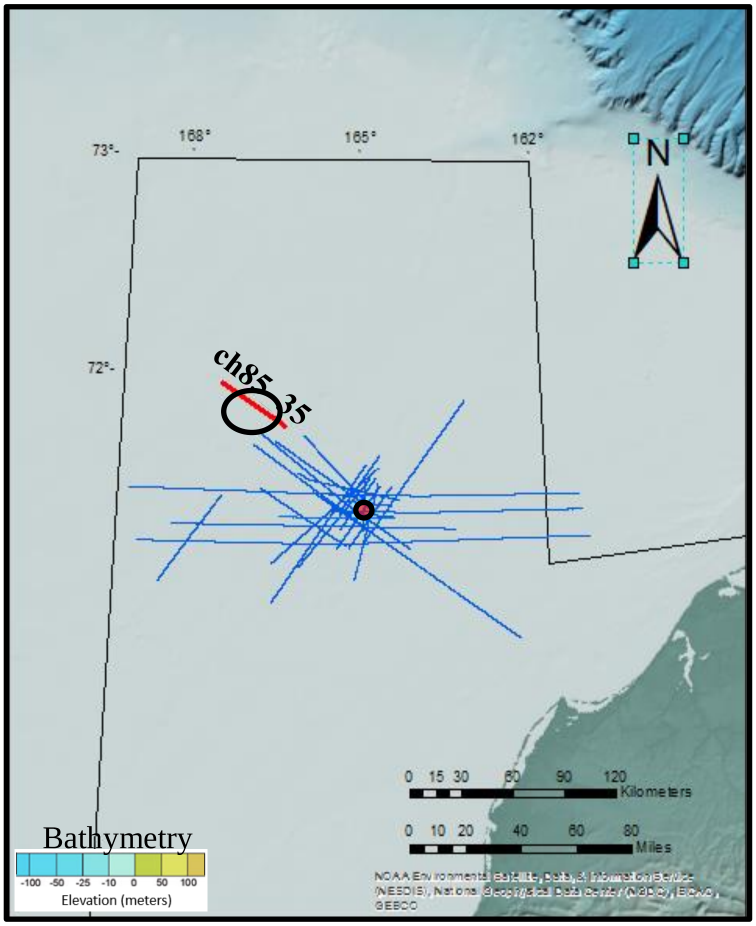

Figure 4.1.4.1.2 Position of line ch85_35 (red line) inside the isolated evaporitic area on the Chukchi Platform (black), and the area of the structure (red circle). Topographic and bathymetric basemap from Jakobsson et al., (2012).

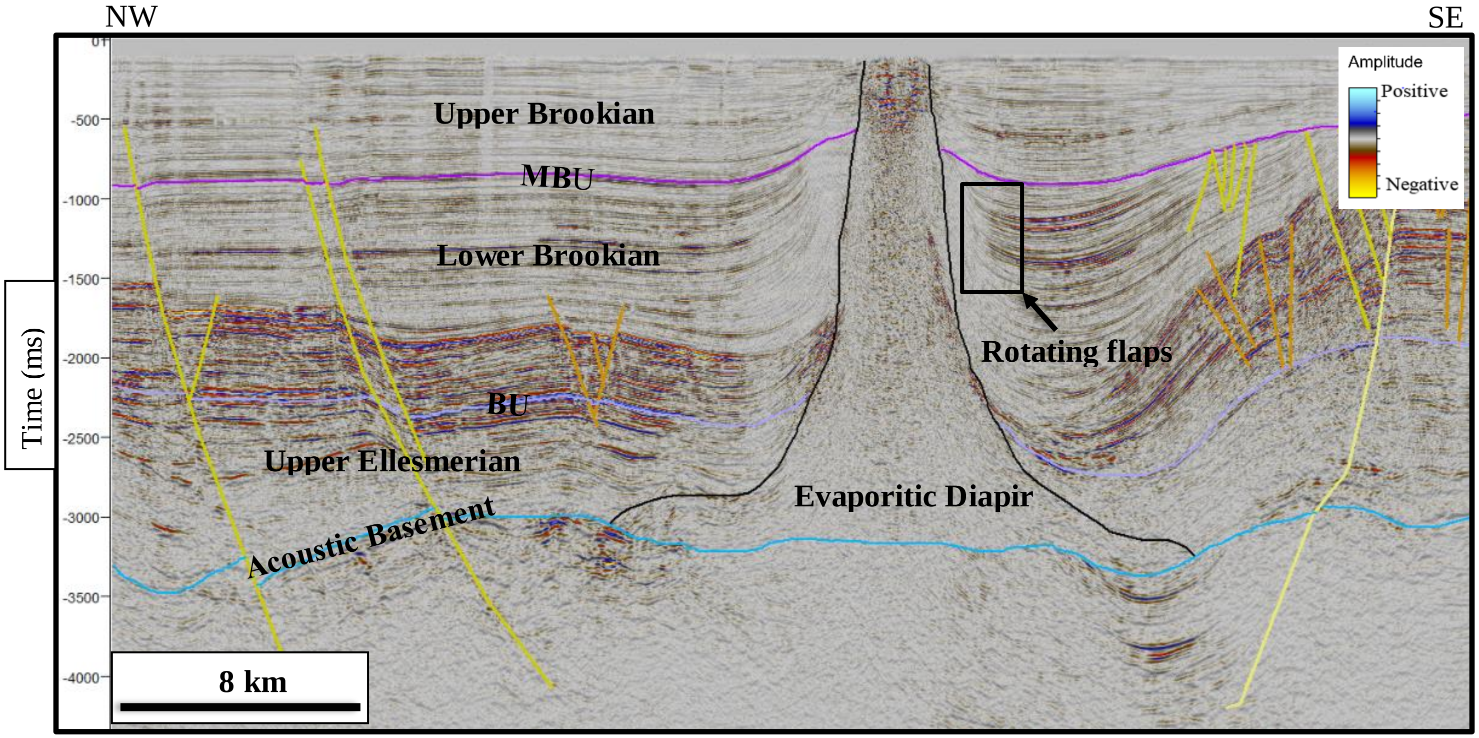

Figure 4.1.3 Evaporitic active diapir as observed on line ch85_35. Location shown in Figure 4.1.2.

4.2. Wrench Faulting

Thurston and Theiss (1987) reported positive and negative wrench faults (flower structures) in the area (Figure 4.2.1). This transpresional-transtensional ~100-mile wide zone of deformation is termed Hanna Wrench-Fault Zone (Thurston and Theiss, 1987). Wrench-fault structures have also been observed in the data; following the fault interpretation procedure, a clear example of a negative flower structure on the Chukchi platform was interpreted (Figure 4.2.2) (Figure 4.2.3).

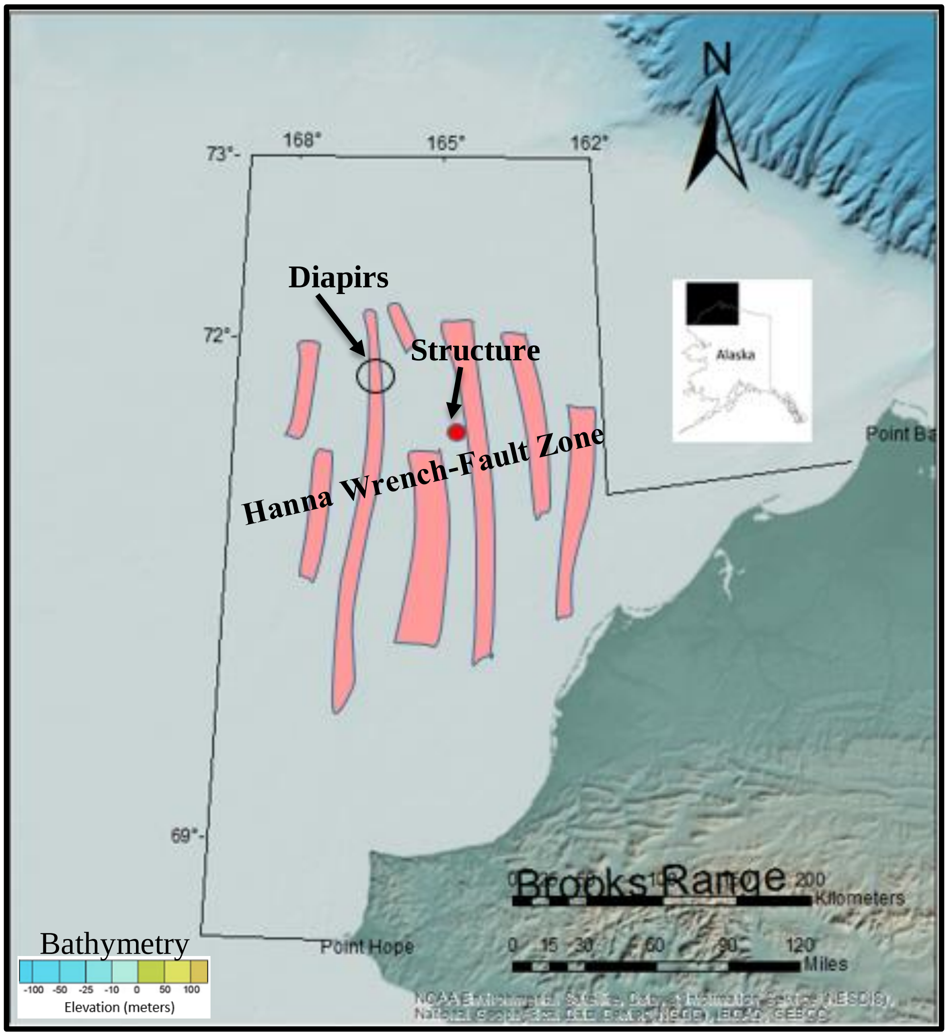

Figure 4.2.1 Closely spaced wrench faults of the Hanna Wrench Fault zone indicated by the pink polygons. Topographic and bathymetric basemap from Jakobsson et al., 2012.

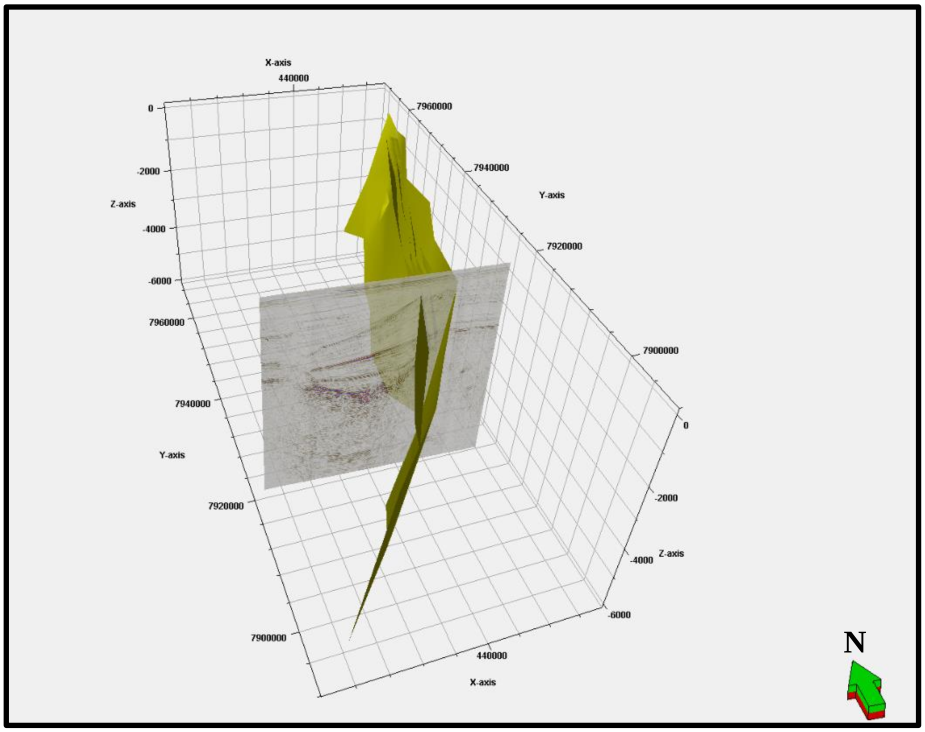

Figure 4.2.3 Pseudo 3-D geometry of an interpreted wrench fault on the Chukchi Platform.

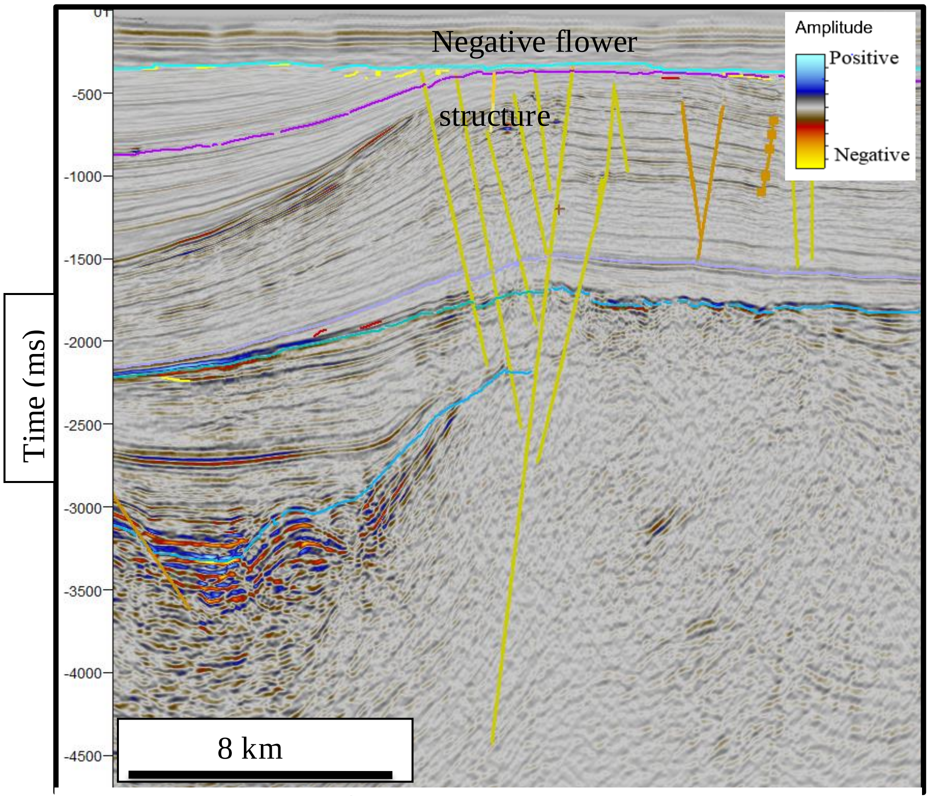

Figure 4.2.2 Wrench fault section on line wcs-6057. Location shown in Figure 3.2.28.

A negative wrench-fault model could explain the faults associated to the structure. In this scenario, the anticlinal feature at the base of the CCDS (Figure 1.1.3) could be a reactive shale diapir associated to the pull-apart basin generated by the transtensional stresses of the negative flower structure, similar to the geological scenario proposed by Smith (2004), to explain the Silverpit Crater structure in the North Sea.

Chaotic seismic facies cannot be easily explained with this model, in the other positive and negative wrench-fault structures observed in this data, the facies related to S6 and MBU are parallel. Additionally the fault mechanical stratigraphy of the other flower structures dates them within wider time ranges (Upper Cretaceous-Middle Eocene).

4.3. Gas chimney

Mound structures, similar to the anticlinal feature at the base of the structure, have been interpreted to being associated with vertical fluid expulsion at the Sea bottom (Figure 4.3.1) (Wang, et al., 2010). These mound structures are of similar geometry and dimensions with the mound observed at the base of the structure.

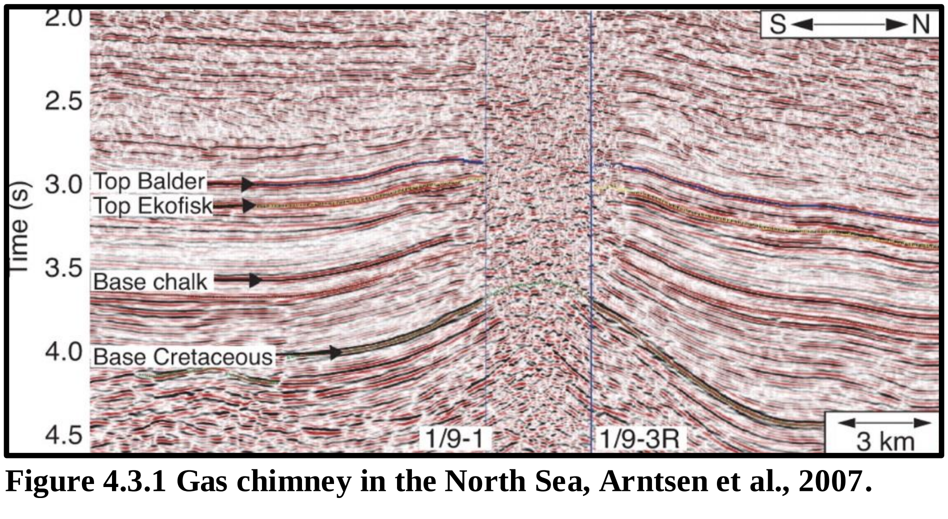

Figure 4.3.1 Gas chimney in the North Sea, Arntsen et al., 2007.

A bright spot with a reversal in apparent polarity can be observed adjacent to the well. This possible DHI is on an upthrown tilted fault block and in a reflector that ties with a low gamma ray measurement in the well on line ch90-001b (Figure 4.3.2), thus creating conditions for structural trapping and indicating a possible gas accumulation.

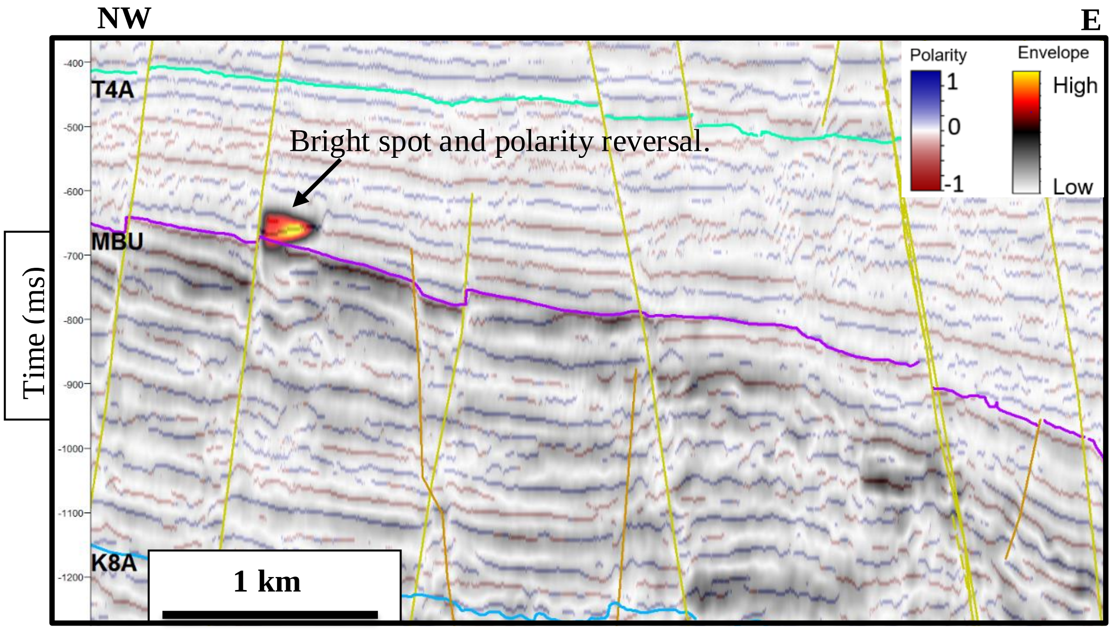

Figure 4.3.2 Apparent polarity co-rendered with envelope at 50% transparency on line ch90-001b. Location shown in Figure 3.3.1.

A bright spot can also be observed closer to the structure on line sc86_8459, in an upthrown block as well (Figure 4.3.3).

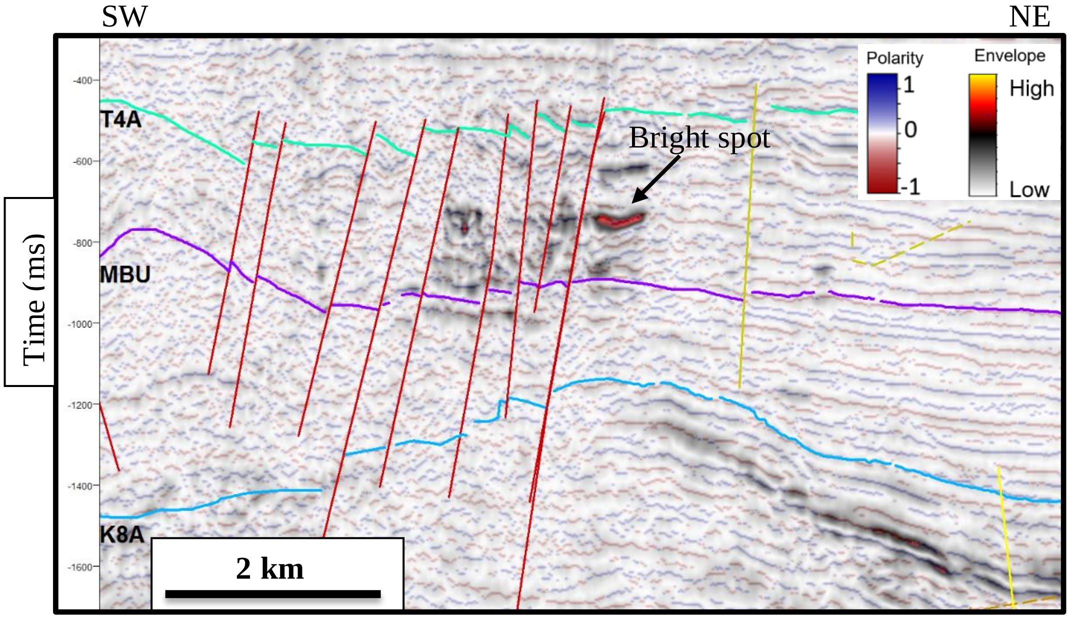

Figure 4.3.3 Bright spot on line sc86_8459, apparent polarity co-rendered with envelope at 50% transparency.

Since the apparent gas accumulation is at the same stratigraphic level as the reflectors associated with the mounded structure (MBU horizon), and the chaotic and dim reflectors above this mounded structure are typical of gas chimneys (Chopra and Marfurt, 2008), it is possible that the anticlinal feature and the chaotic dim reflectors in the structure are product of gas accumulation.

4.4. Complex Meteorite Impact Crater

The morphology of meteorite impact craters vary according to the projectile energy, target strength, and target gravity (Melosh, 1989). The first morphological type is the simple crater morphology, the characteristic features are a bowl shaped depression, an uplipfted rim, and an ejecta blanket, there is no minimum diameter size, these craters srange from a couple of meters to ~ 2 km of diameter in the Earth (Melosh, 1989). The second type are the complex craters, these are characterized by a central uplift and faulted concentric terrace faults, the minimum diameter of these craters is ~2 km in the Earth, and the range of transition between simple and complex structures (i.e. diameters at which complex features in a crater are recognizable) is between 2 km-4 km in diameter in the Earth. The third type are the multi-ringed basins, for these type of structures it is complicated to stablish a transition diameter relative to the gravity of the target. There are reported multi ring basins in extraterrestrial bodies with transition diameters ranging from hundreds to thousands of kilometers, e.g. the Mare Orientale on the Moon, with a diameter of roughly 900km (Melosh, 1989).

The preservation of impact structures on the Earth is not as good as in extraterrestrial bodies, because of the dynamic processes that affect the surface and subsurface of the earth (e.g. erosion, and tectonism) (Kenkmann et al., 2014; Melosh, 1989). Besides, the characteristics of both simple and complex structures can be misinterpreted as other types of circular endogenic geological features (e.g. volcanoes and structural analogs previously mentioned) (Kenkmann et al., 2014; Melosh, 1989).

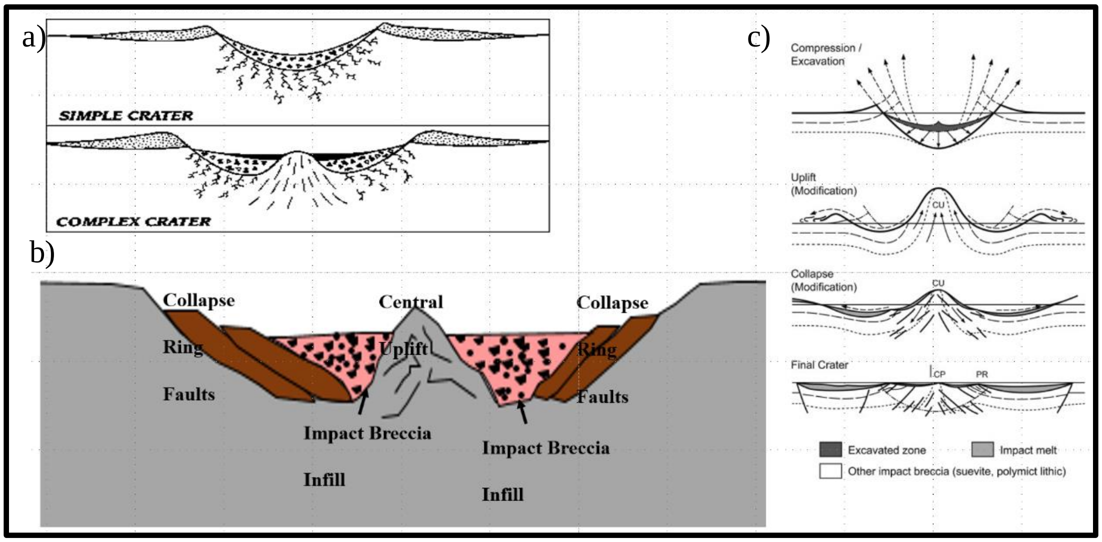

Figure 4.4.1 a) Morphology of an simple and complex impact craters (Hamilton, 2016), b) Morphological features of a complex crater, c) complex crater evolution (Reimold and Koeberl, 2014). Sigma 3 stresses are horizontal and radial.

The distance measured between the outermost faults related to the structure is ~10km, in the range of complex impact structures in the Earth) (Kenkmann et al., 2014; Melosh, 1989). The faults, the anticlinal dome beneath the structure, and the chaotic facies above the anticlinal dome, are observed in the strike line wcs-6059, oblique line ch83-104a, and in the dip line sc86_8459, this observations provide an argument for a circular geometry of the structure such as in complex impact craters.

The faults related to the structure share characteristics with collapse fault terraces in complex impact structures, the anticlinal dome at the base of the structure might be a central uplift feature, and the chaotic dim reflectors in the middle of the structure could indicate an impact-crater breccia infill. Thus, a complex meteorite impact crater model can consistently explain the characteristic features of the CCDS.

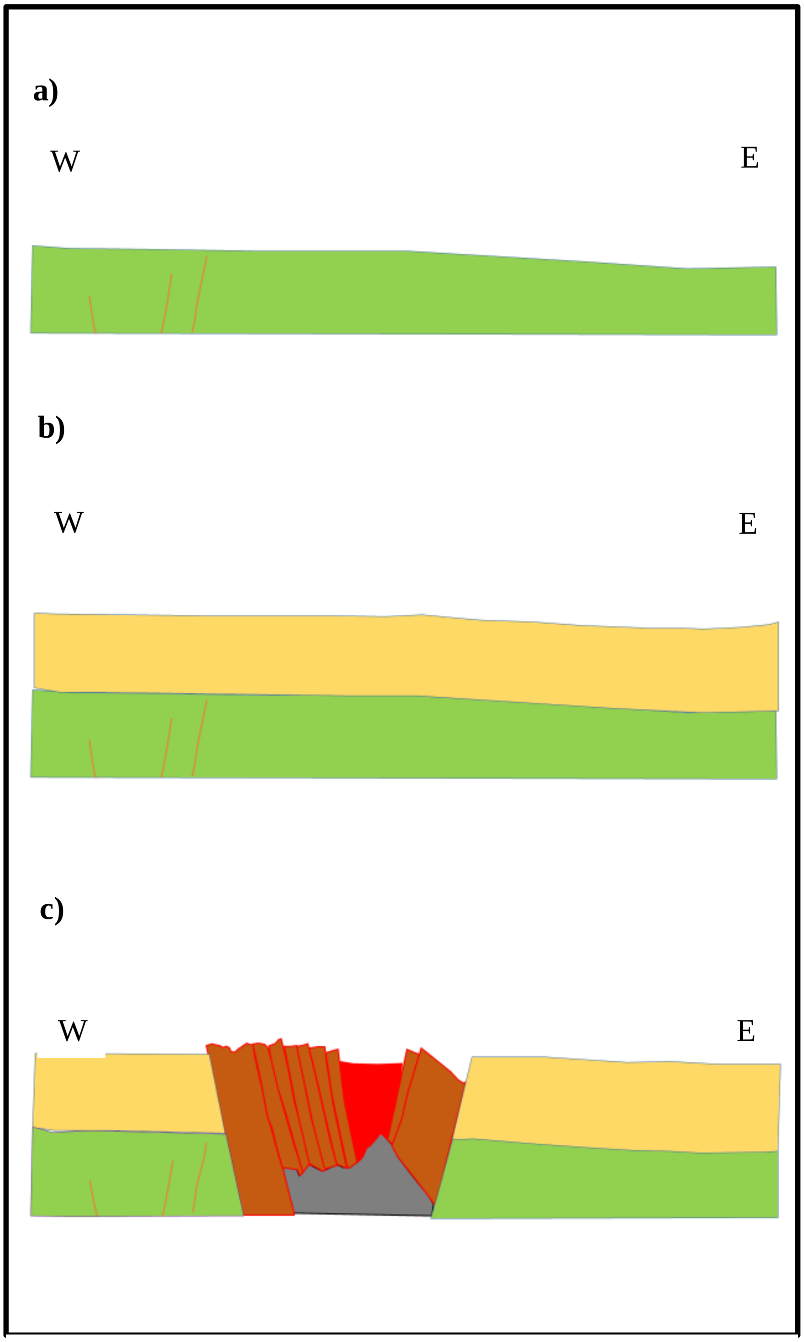

Figure 4.4.2 Geological evolution of the impact structure: a) Upper Cretaceous, b) Lower Eocene, c) Middle Eocene.

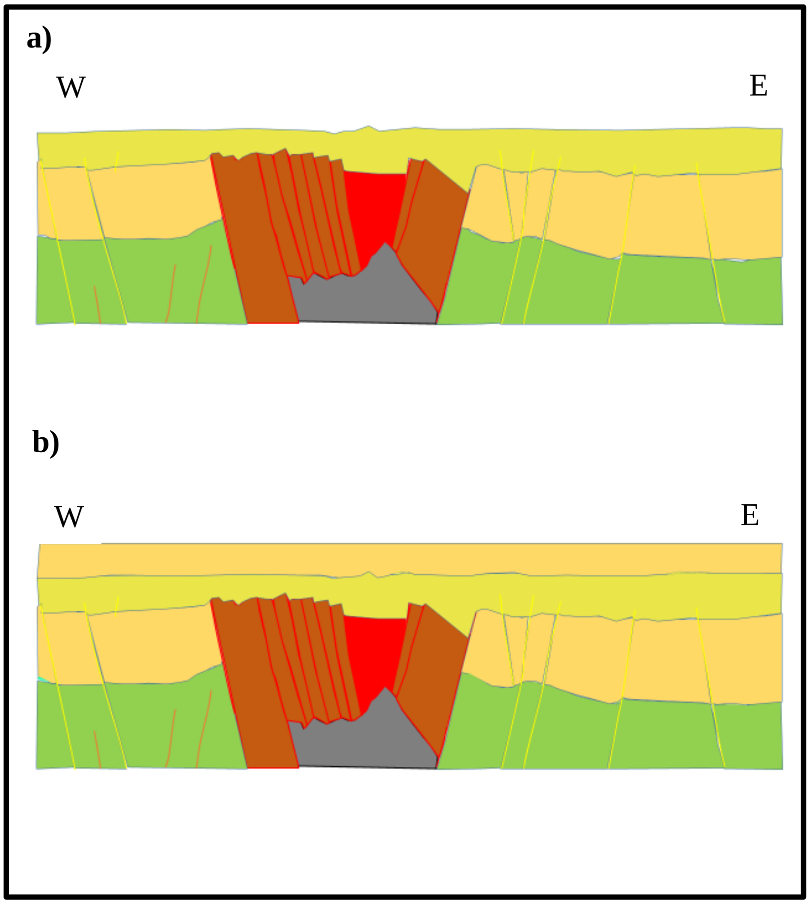

Figure 4.4.3 Geological evolution of the impact structure: a) Middle Eocene (top) and b) Pliocene.

Additionally, there are proven complex meteorite impact craters imaged in 3-D seismic that share similar characteristics with the CCDS. One example of that is the Silverpit crater in the North Sea. The central uplift and the tightly chronologically constrained faults in the Silverpit crater (Figure 4.4.4) are similar to the ones observed in the CCDS, another clear parallelism is the circular concentric geometry of the collapse faults (Figure 4.4.5).

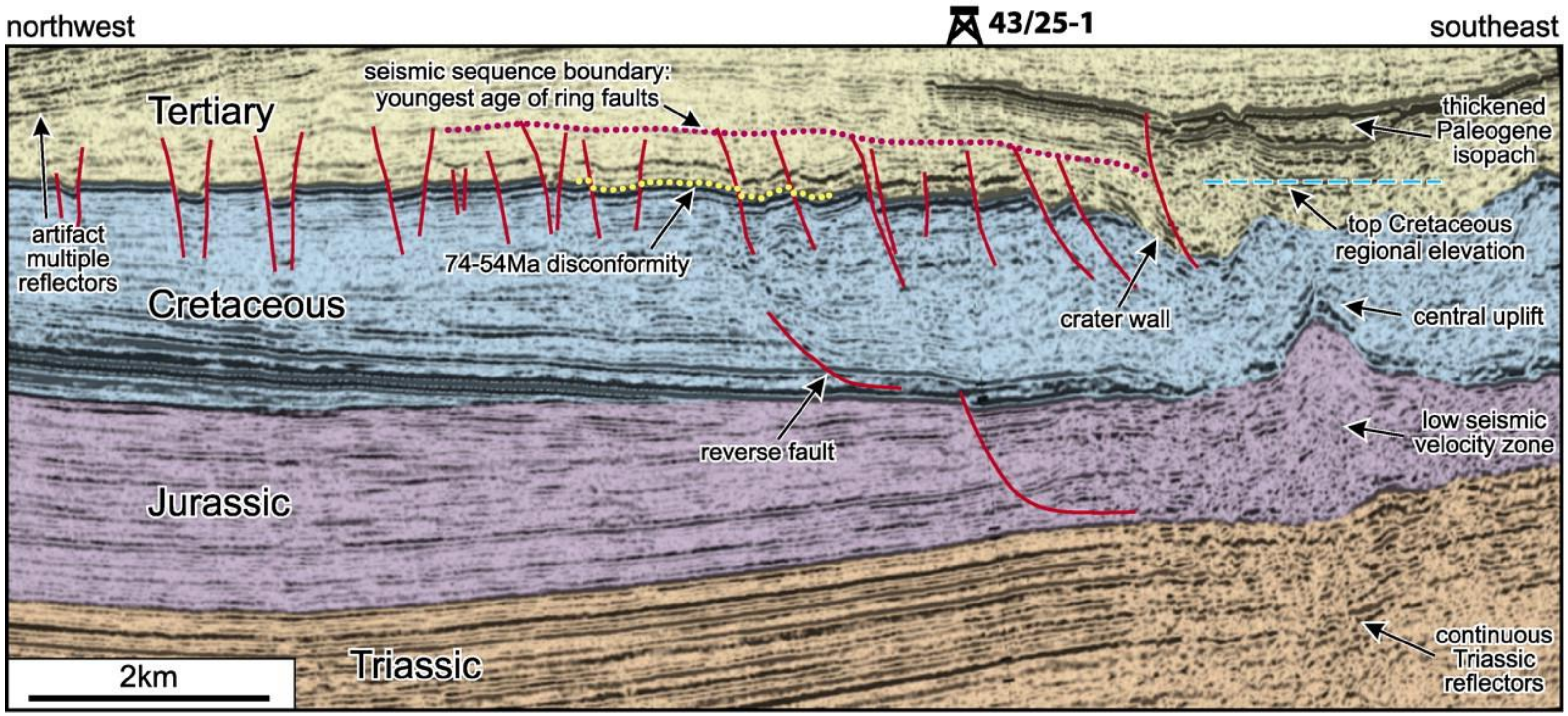

Figure 4.4.4 Elements of the Silverpit impact crater, from Stewart and Allen, 2012.

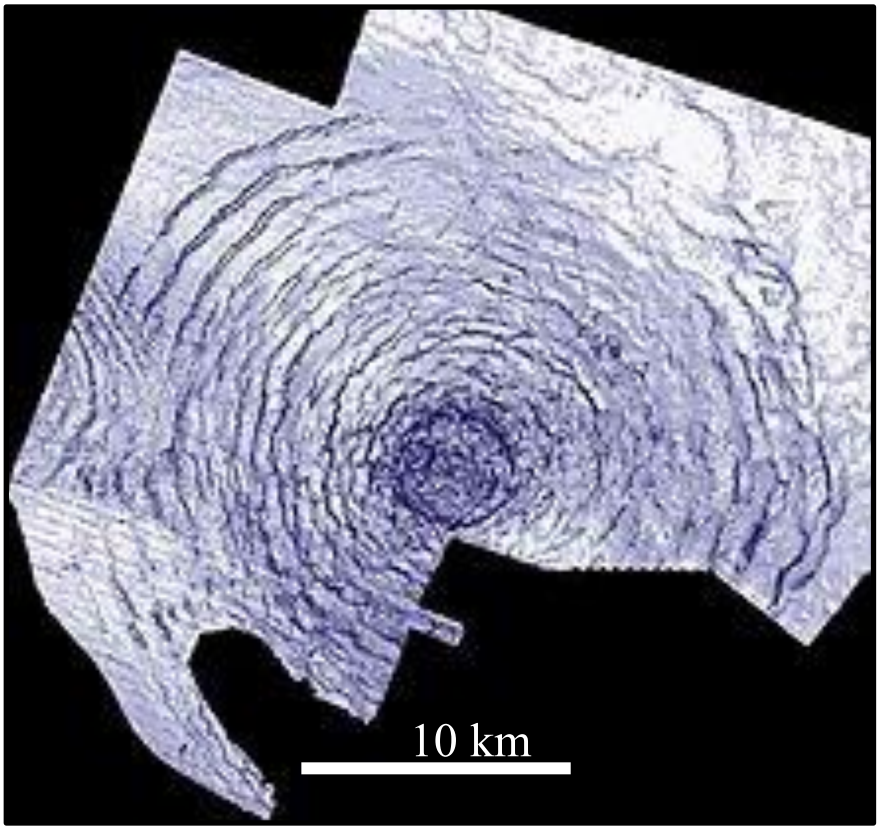

Figure 4.4.5 Concentric fault terraces observed on a structural time slice on the Silverpit crater, from Stewart and Allen, 2012.

5. Conclusions

By integrating seismic stratigraphy, fault mechanical stratigraphy, and attribute assisted interpretation the CCDS has been interpreted as a complex impact crater. The fault mechanical stratigraphy of the faults which constrains it to a limited geologic time in the Middle Eocene, the seismic expression of the structure (chaotic, contorted, and low frequency facies), and the structural styles of the structure, i.e. concentric ring faults, and the central uplift match those of a complex impact structure. Nonetheless, fluid expulsion and negative flower structures (wrench faulting) are possible as well due to the geological settings of the area, indicated both by the bright spots observed on the data and the interpreted wrench faults. A reactive diapir is unlikely because of the lack of evaporites or overpressured shales in the area of the structure, besides the diapirs that are observed on the Chukchi Platform are of the active type.

Exploration in frontier regions with limited data availability requires the application of proper interpretation techniques that are geological significant and a thorough understanding of the virtues and limitations of the data.

References

Arntsen, B., L. Wensaas, H. Løseth, and C. Hermanrud, 2007, Seismic modeling of gas chimneys: Geophysics, v. 72, p. sm251-sm259, doi: 10.1190/1.2749570

Bacon M., R. Simm, and T. Redshaw, 2003, 3-D seismic interpretation: Cambridge University press, 225 p., doi: 10.1017/CBO9780511802416.

Chopra, S., and K. J., Marfurt, 2008, Seismic Attributes for Prospect Identification and Reservoir Characterization: Tulsa, Society of Exploration Geophysicists, p.464

Craddok, W. H., and D. W. Houseknecht, 2016, Cretaceous-Cenozoic burial and exhumation history of the Chukchi shelf, offshore Arctic Alaska: AAPG bulletin, v. 100, no. 1, p. 63-100, doi: 10.1306/09291515010.

Grantz A., M. L. Holmes, and B. A. Kososki, 1975, Geologic framework of the Alaskan continental terrace in the Chukchi and Beaufort seas, in Yorath C. J., E. R. Parker, and D. J. Glass, ed., Canada's continental margins and offshore petroleum exploration Calgary, CSPG, memoir 4, p. 669 – 700.

Grantz, A, and S. D. May, 1984a, Summary geologic report for barrow arch outer continental shelf (OCS) planning area, Chukchi Sea, Alaska: Menlo Park, United States Geological Survey Open-File Report, 44 p.

Hamilton, C. J, 2011, Terrestrial impact craters, http://solarviews.com/eng/tercrate.htm, (accessed December 4, 2017).

Jakobsson, M. L. A. Mayer, B. Coakley, J. A. Dowdeswell, S. Forbes, B. Fridman, and H. Hodnesdal et al., 2012, The international bathymetric chart of the Arctic Ocean (IBCAO) Version 3.0: Geophysical Research Letters, v. 39, no. 12, p. L12609, doi: 10.1029/2012GL052219.

Johnson, P.P., 1992, The North Chukchi high-compressional structures in a rift setting: International Conference on Arctic Margins Abstracts with Programs, Anchorage, Alaska, p. 28.

Kenkmann, T., M. H. Poelchau, and G. Wulf, 2014, Structural geology of impact craters: Journal of Structural Geology, v. 62, p. 156-182, doi: 10.1016/j.jsg.2014.01.015.

Melosh, H. J., 1989, Impact cratering a geologic process: New York, Oxford University Press, 245 p.

Minerals Management Service, 2006, Chukchi Sea Province Summary, Assessment – Alaska Region. Available online at: https://www.boem.gov/uploadedFiles/BOEM/About_BOEM/BOEM_Regions/A laska_Region/Resource_Evaluation/2006AssessmentFiles/Chukchi%20Sea%20 Province%20Summary-2006%20Assessment.pdf

Mitchum, R. E., Jr., P. R. Vail, and J. B. Sangree, 1977, Stratigraphic Interpretation of Seismic Reflection Patterns in Depositional Sequences, in C. E. Payton, ed., Seismic Stratigraphy- applications to hydrocarbon exploration, Tulsa, American Association of Petroleum Geologists, Memoir, 26, p. 117-133.

Pigott, J. D., and M. O. Abouelresh, 201, Basin deconstruction-construction: Seeking thermal tectonic consistency through the integration of geochemical thermal indicators and seismic fault mechanical stratigraphy-Example from Faras Field, North Western Desert, Egypt: Journal of African Earth Sciences, v. 114, p. 110-124, doi 10.1016/j.jafrearsci.2015.11.006.

Pigott, J. D., M. H. Kang, and H. C. Han, 2013, First order seismic attributes for clastic seismic facies interpretation: Examples from the East China Sea: Journal of Asian Earth Sciences, v. 66, p. 34-54.

Pigott, J. D., and D. Radivojević, 2010, Seismic stratigraphy based chronostratigraphy (SSBC) of the Serbian Banat region of the Pannonian basin: Central European Journal of Geosciences, v. 2, p. 481-500, doi: 10.2478/v10085-010-0027-2.

Reimold, W. U., and C. Koeberl, 2014, Impact structures in Africa: A review: Journal of African Earth Sciences, v. 93, p. 57-175, doi: j.jafrearsci.2014.01.008.

Santos Betancor, I., and J. I. Soto, 2015, 3D geometry of a shale-cored anticline in the western South Caspian Basin (offshore Azerbaijan): Marine and Petroleum Geology, v. 67, p. 829-851, doi: 10.1016/j.marpetgeo.2015.06.012

Schultz-Ela D.D., M.P.A, Jackson, and B.C., Vendeville, 1993, Mechanics of active salt diapirism: Tectonophysics, v. 228, p. 275-312.

Sheriff R. E., and L. P. Geldart, 1995, Exploration Seismology: New York, Cambridge University Press, p. 575.

Sherwood, K. W., P. P. Johnson, J. D. Craig, S. A. Zerwick, R. T. Lothamer, D. K. Thurston, and S. B. Hurlbert, 2002, Structure and stratigraphy of the Hanna trough, U.S. Chukchi self, Alaska, in E. L. Miller, A. Grantz, and S. L. Klemperer, eds., Tectonics evolution of the Bering Shelf-Chukchi Sea-Arctic Margin and adjacent landmasses: Geological Society of America Special Paper 360, p. 39-66, doi:10.1130/0-8137-2360-4.39.

Smith, K., 2004, The North Sea Silverpit Crater: impact structure or pull-apart basin? : Journal of the Geological Society, v. 161, p. 593-602.

Taner, M.T, F. Koehler, and R. E. Sheriff, 1979, Complex seismic trace analysis: Geophysics, v. 44, p. 1041-1063.

Thurston, D. K., and R. T. Lothamer, 1991, Seismic evidence of evaporate diapirs in the Chukchi Sea, Alaska: Geology, v. 19, p 477-480.

Thurston, D. K., and L. A. Theiss, 1987, Geologic report for the Cukchi Sea planning area, Alaska, Regional Geology, Petroleum Geology, and Environmental Geology, in Sherwood, K. W., ed., OCS Report MMS 87-0046, 193 p.

Tolson, R. B., 1987, Structure and Stratigraphy of the Hope Basin, Southern Chukchi Sea, Alaska, in D. W. Scholl, A. Grantz, and J. G. Vedder, ed., Geology and Resource Potential of the Continental Margin of Western North America and Adjacent Ocean Basins- Beaufort Sea to Baja California: Menlo Park Circum-Pacific Council for Energy and Mineral Resources Earth Science Series, v. 6, p. 59-71.

Walden, A. T., and R. E. White, 1998, Seismic Wavelet Estimation: A frequency domain solution to a geophysical noisy input-output problem: IEEE transactions on Geoscience and Remote Sensing, v. 36, p. 287-297.

Appendix A: Attribute Assisted Interpretation

A seismic attribute can be seen as a mathematical operation performed on seismic data that is susceptible to certain characteristics of the seismic signal. These characteristics are quantitatively or qualitatively proportional to the underlying geological information in the seismic signal

A.1 Envelope

The envelope is considered as the calculation of the reflection strength of the trace, and it is calculated as the Euclidean norm of the real and imaginary trace (quadrature) in the complex plane (Taner et al., 1979).

$$R(t) = \sqrt{x(t)^2 + y(t)^2}$$

the quantities x(t) and y(t) represent the real and imaginary trace respectively.

This attribute was used to help in the identification of bright spots, a clear example of this is the bright spot observed in line ch90-001b (Figure 4.1.1).

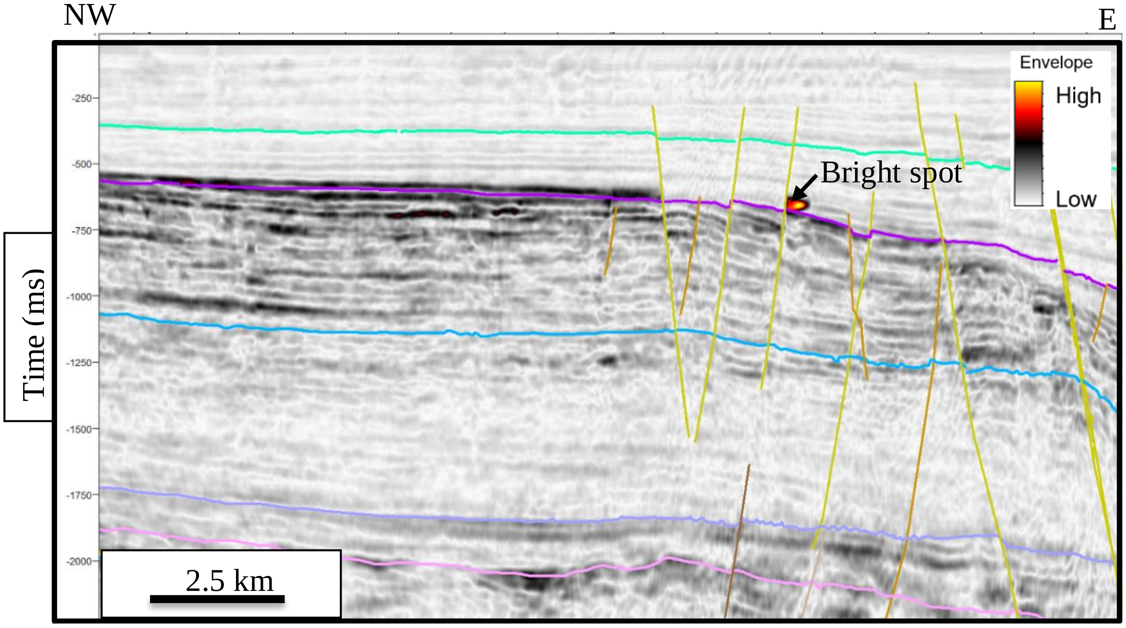

Figure A.1.1 Envelope on line ch90-001b, a bright spot is identified using this attribute.

A.2 Cosine of Instantaneous Phase

The cosine of instantaneous phase “normalizes” the amplitude of seismic traces, highlighting the continuity of the reflectors (Pigott et al, 2013) and is defined as:

$$\emptyset = \arctan \frac{y(t)}{x(t)}$$

where, y(t) is the cuadrature or imaginary trace obtained by taking the Hilbert transform of the real trace x(t). The cosine of phase trace c(t) is then:

$$c(t) = \cos \emptyset(t)$$

The cosine of instantaneous phase assisted the interpretation of reflector terminations, faults, and reflector geometry, as it can be observed in the extraction of cosine of phase in line wcs-6057 (Figure 4.2.1).

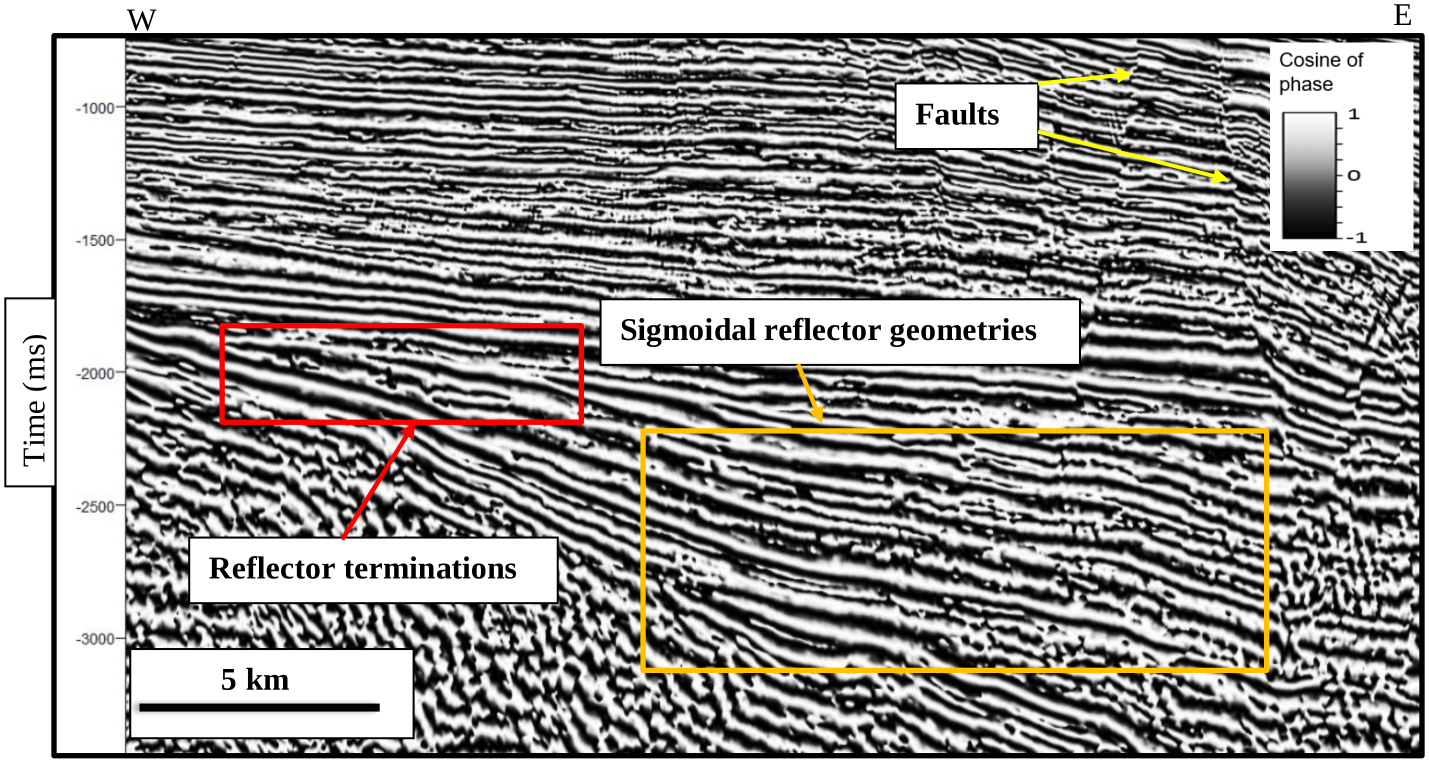

Figure A.3.1 Terminations, reflector geometries, and faults enhanced in the cosine of phase section of line wcs 6057. Location shown in Figure 3.2.28.

A.3 Variance

Variance is a statistical measurement of waveform similarity (Chopra and Marfurt, 2007) and it is calculated as follows:

$$var(t,p,q) = \frac{\frac{1}{J}\sum_{j=1}^{J}[u_j\left(t - px_j - qy_j\right) - < u(t,p,q) >]^2}{\frac{1}{J}\sum_{j=1}^{J}[uj(t - px_j - qy_j]^2}$$

where

$$< u(t,p,q) >$$

Indicates the mean seismic trace, and p and q the apparent dips. The variance measures the difference between each trace and the mean trace.

The variance estimate of waveform similarity was utilized in this work for fault interpretation and seismic facies description, particularly in the identification of chaotic seismic facies. An example of this application is the extraction of this attribute in line wcs-6057, where both the chaotic facies associated with the CCDS and normal faults can be observed (Figure 4.3.1).

The implementation of variance in this work was useful regardless of the influence of amplitude changes in its calculation and not only being affected by waveform changes, since it was utilized for fault interpretation and chaotic facies recognition where both waveform and amplitude changes are expected.

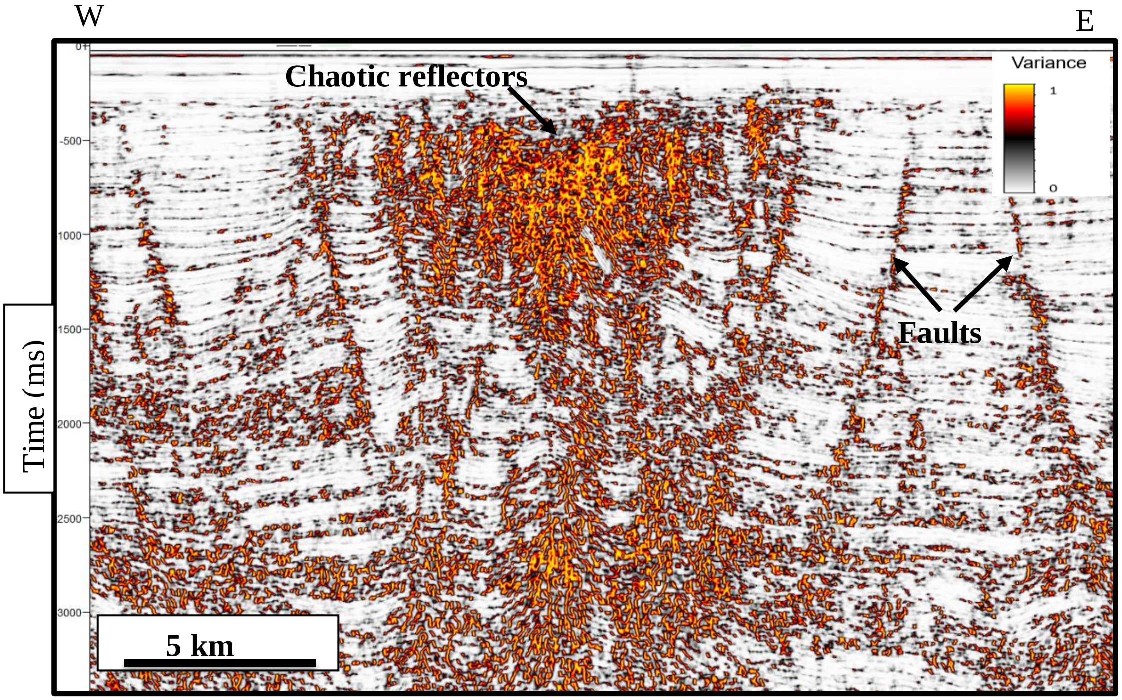

Figure A.3.1 Chaotic reflectors and faults enhanced in a variance section of line wcs-6059. Location shown in Figure 3.2.28.

A.4 Apparent polarity

Apparent polarity is defined by the sign of the real trace x(t) at its envelope maximum. Together with reflection strength (Taner et al, 1979), this attribute was used to identify possible fluid accumulations. The bright spot on line ch90-001b, also displays a change in apparent polarity, which is not as easy to observe in original amplitude but it is clear in the apparent polarity section (Figure 4.4.1).

$$polarity = e(t) signum[\varphi(t)]$$

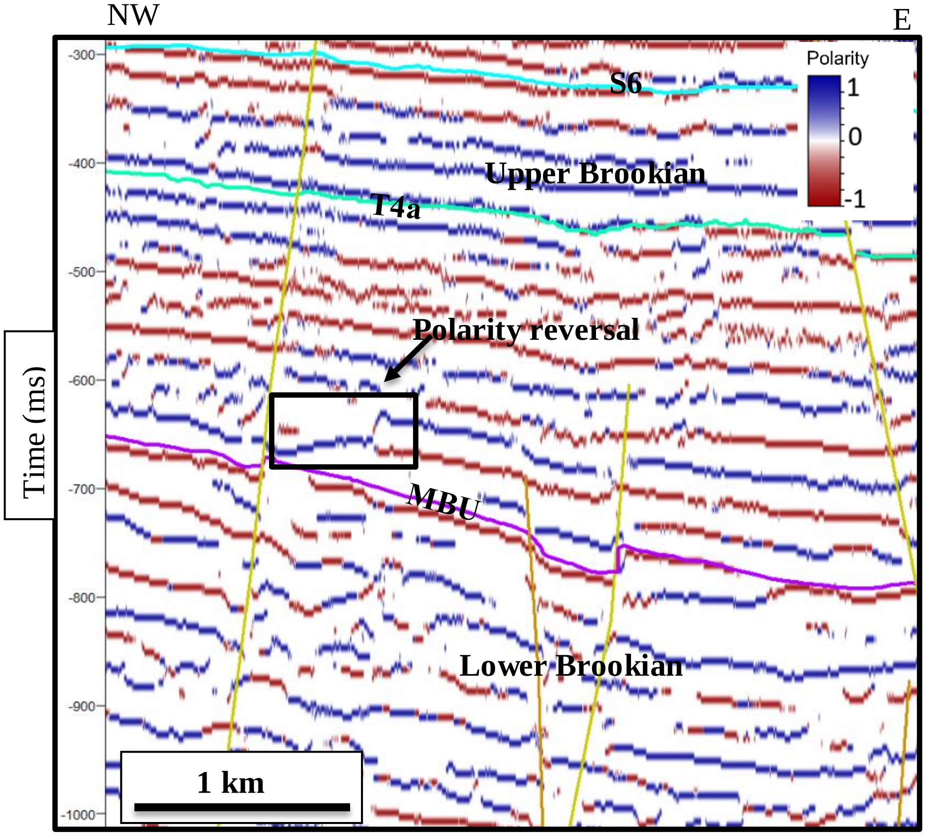

Figure A.4.1 Polarity reversal identified in an apparent polarity section on line ch90-001b. Location shown in Figure 3.3.1.